**Title**
Fabrication and Characterization of Organic/Inorganic Photovoltaic Devices



**Author**
Guvenc, Ali Bilge

**Publication Date**
2012

Peer reviewed|Thesis/dissertation

UNIVERSITY OF CALIFORNIA
RIVERSIDE

# Fabrication and Characterization of Organic/Inorganic Photovoltaic Devices

A Dissertation submitted in partial satisfaction
of the requirements for the degree of

Doctor of Philosophy

in

Electrical Engineering

by

Ali Bilge Guvenc

March 2012

Dissertation Committee:
Dr. Mihrimah Ozkan, Chairperson
Dr. Cengiz S. Ozkan
Dr. Kambiz Vafai

The Dissertation of Ali Bilge Guvenc is approved:

_____

_____

_____

Committee Chairperson

University of California, Riverside

To my beloved wife and daughters

ABSTRACT OF THE DISSERTATION

Fabrication and Characterization of Organic/Inorganic Photovoltaic Devices

by

Ali Bilge Guvenc

Doctor of Philosophy, Graduate Program in Electrical Engineering
University of California, Riverside, March 2012
Prof. Mihrimah Ozkan, Chairperson

Energy is central to achieving the goals of sustainable development and will continue to be a primary engine for economic development. In fact, access to and consumption of energy is highly effective on the quality of life. The consumption of all energy sources have been increasing and the projections show that this will continue in the future. Unfortunately, conventional energy sources are limited and they are about to run out. Solar energy is one of the major alternative energy sources to meet the increasing demand. Photovoltaic devices are one way to harvest energy from sun and as a branch of photovoltaic devices organic bulk heterojunction photovoltaic devices have recently drawn tremendous attention because of their technological advantages for actualization of large-area and cost effective fabrication. The research in this dissertation focuses on both the mathematical modelling for better and more efficient characterization and the improvement of device power conversion efficiency. In the first part, we studied the

effect of incident light power on the space charge regions of the Schottky barriers of the organic bulk heterojunction photovoltaic devices, the current-voltage characteristics and performance of the devices and built a current-voltage model for the devices that involves these effects. The incident light power showed an effect on the Schottky barriers of the devices by changing the width of the space charge regions. This change directly affects the reverse bias current-voltage curves by increasing the current values and the slope of the curves. But under excessive incident light power; the space charge regions merge, the devices break down and work as ohmic devices. In the second part, we combined the two improvement methods, improving the charge carrier transport and improving absorption of the organic bulk heterojunction photovoltaic devices. For charge carrier transport improvement, we presented deoxyribonucleic acid complexes as hole collecting and electron blocking layer on the anode side of the devices by using them as band energy diagram arranging layer, for absorption improvement with plasmonic effect of the particles, we present colloidal platinum nanoparticles as the surface plasmons. Deoxyribonucleic acid complex layer improved the device performance by improving the charge carrier hopping efficiency of the devices by arranging the band energy diagram in order to collect holes easily and block electrons diffusing to anode electrodes. Colloidal platinum nanoparticles layer improved the device performance by increasing the light-harvesting efficiency of the devices by increasing the rate of photon absorption. This proves that the colloidal platinum nanoparticles can be used as surface plasmons in organic bulk heterojunction photovoltaic devices. Because peak their extinction spectra matches with the peak of absorbance of poly(3-hexylthiophene) (P3HT): [6,6]-phenyl-

$C_{61}$-butyric acid methyl ester (PCBM). Combination of these two novel materials in the same device showed a significant improvement as a 26% increase in the power conversion efficiency of the devices. The research conducted in this dissertation offers promising potential of organic bulk heterojunction photovoltaic devices as one of the clean and affordable alternative energy sources for supplying increasing demand on energy.

**Table of Contents**

**List of Figures**

**List of Tables**

## Chapter 1:

## Introduction

Energy is defined as the capacity of to do work. It is food for the human activity in the broadest sense: it moves our bodies, cooks our food, heats and lights our houses, moves our vehicles and etc.[1] It is central to achieving the goals of sustainable development and will continue to be a primary engine for economic development. It is involved in everything that happens on earth. In fact, access to and consumption of energy is highly effective on the quality of life. In figure 1-1, United Nations (UN) Human development index (HDI), which is a composite index based on measures of health, longevity, education, and economic standards of living, in 2011, versus average per capita electricity usage per person in year 2010 for 162 countries is given. The per capita consumption of electricity correlates well with a country's social well-being as measured by the UN HDI. As it can be seen from the figure energy production and utilization directly affect living standards and prosperity and are at the hearth of prosperity everywhere in the world.

This chapter begins with an overview of the situation in global energy; consumption, according to world population, regions and fuel sources, and projections for future demand. Then, in order to understand the importance of the renewable energy for the future of the humanity, increasing gap between world oil supply and demand, and the effect of carbon dioxide ($CO_2$) emission on the global warming are demonstrated. From this perspective this chapter also gives an overview on renewable energy sources; types

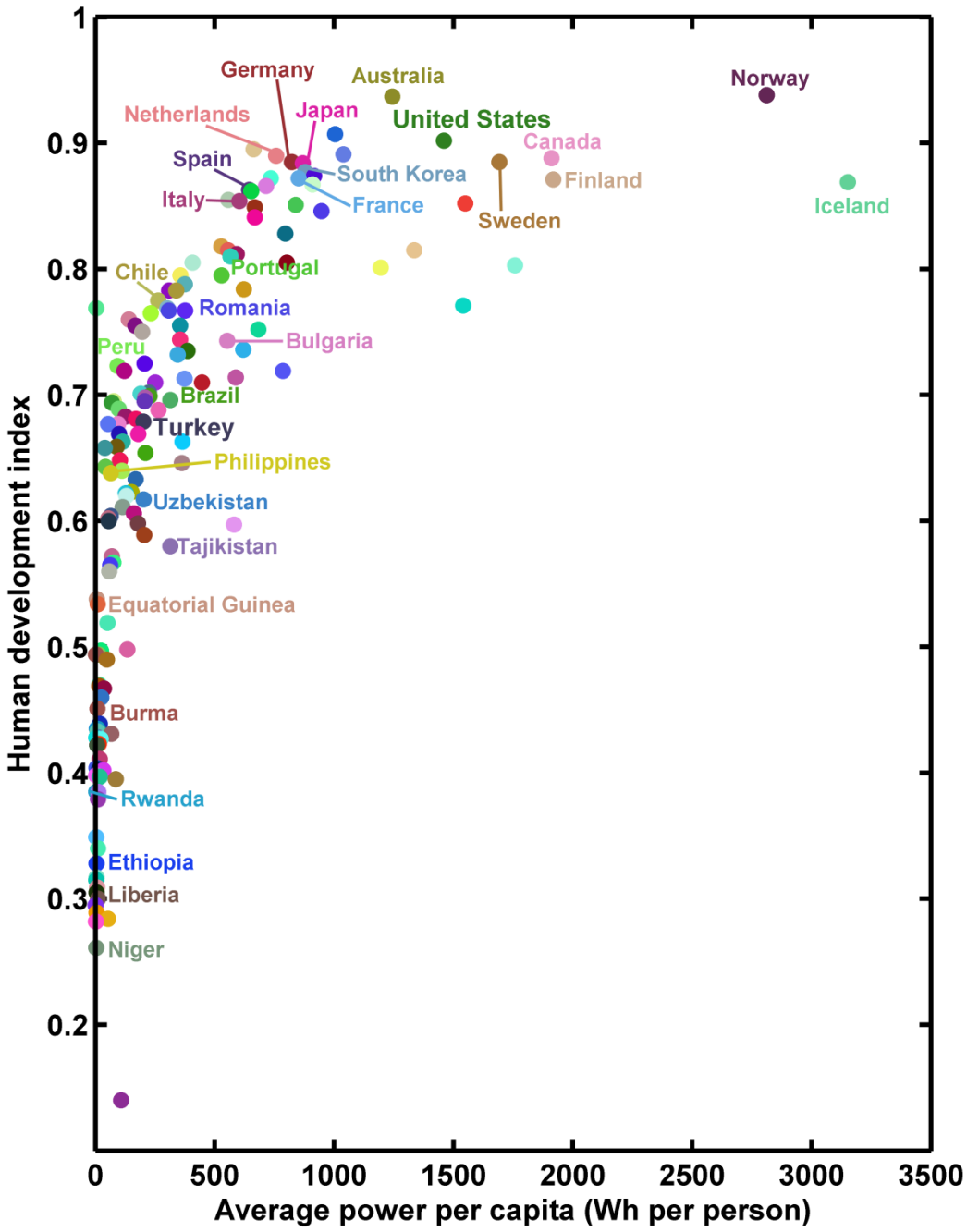


**Figure 1-1** Human development index in year 2011 versus annual average power per capita per person in year 2010[2, 3]

of renewable energy sources and consumption according to regions. Finally, the current situation in solar energy harvesting, capacity of electricity generation from solar harvesting according to regions, and future projections are given.

### 1.1 Big Picture in World Energy

The world population is currently about 6.96 billion[4] (Figure 1-2). The UN projects growth to approximately 8.5 billion by 2035[4] (Figure 1-2). As it can be seen from figure 1-1, the population increase from 2005 to 2011 have been occurred and projections of the population increase of 1.5 billion people between 2011 and 2035 will occur almost entirely in non-Organization for Economic Co-operation and Development (OECD) countries such as China and India. These countries continue to lead world economic growth and energy demand growth even during the global recession of 2008-2009. Since 1990, energy consumption in these countries as a share of total world energy use has increased significantly, and they accounted for about 50% of total world energy consumption in 2010. Whereas these countries have 85% of the world population in 2010 and it is projected that most of the increase in the world population will be in these countries.[4] If the world is to meet even a fraction of the economic hopes of the people already alive today, plus those still to be born in these countries, there will be a substantial increase in energy need. As it can be seen from figure 1-3, most of this increase in the energy need have been and will also be in these countries. Energy use in non-OECD countries was 7% greater than that in OECD countries in 2010 and it is projected that non-OECD economies will consume 38% more energy than OECD economies in 2020 and 67% more in 2035.[4]

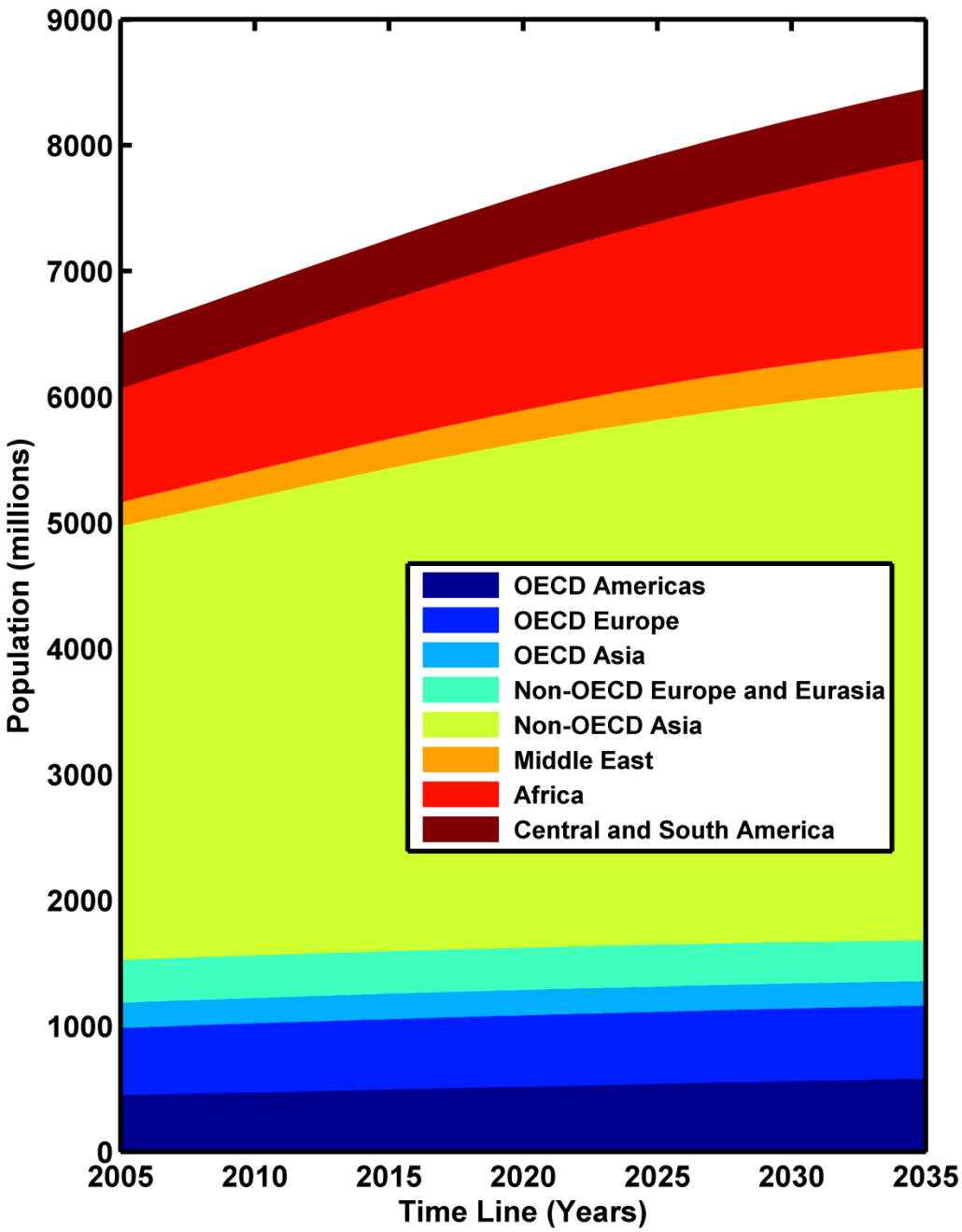


**Figure 1-2** World populations (in millions) according to regions from 2005 to 2011 and projected population between 2011 and 2035.[4]

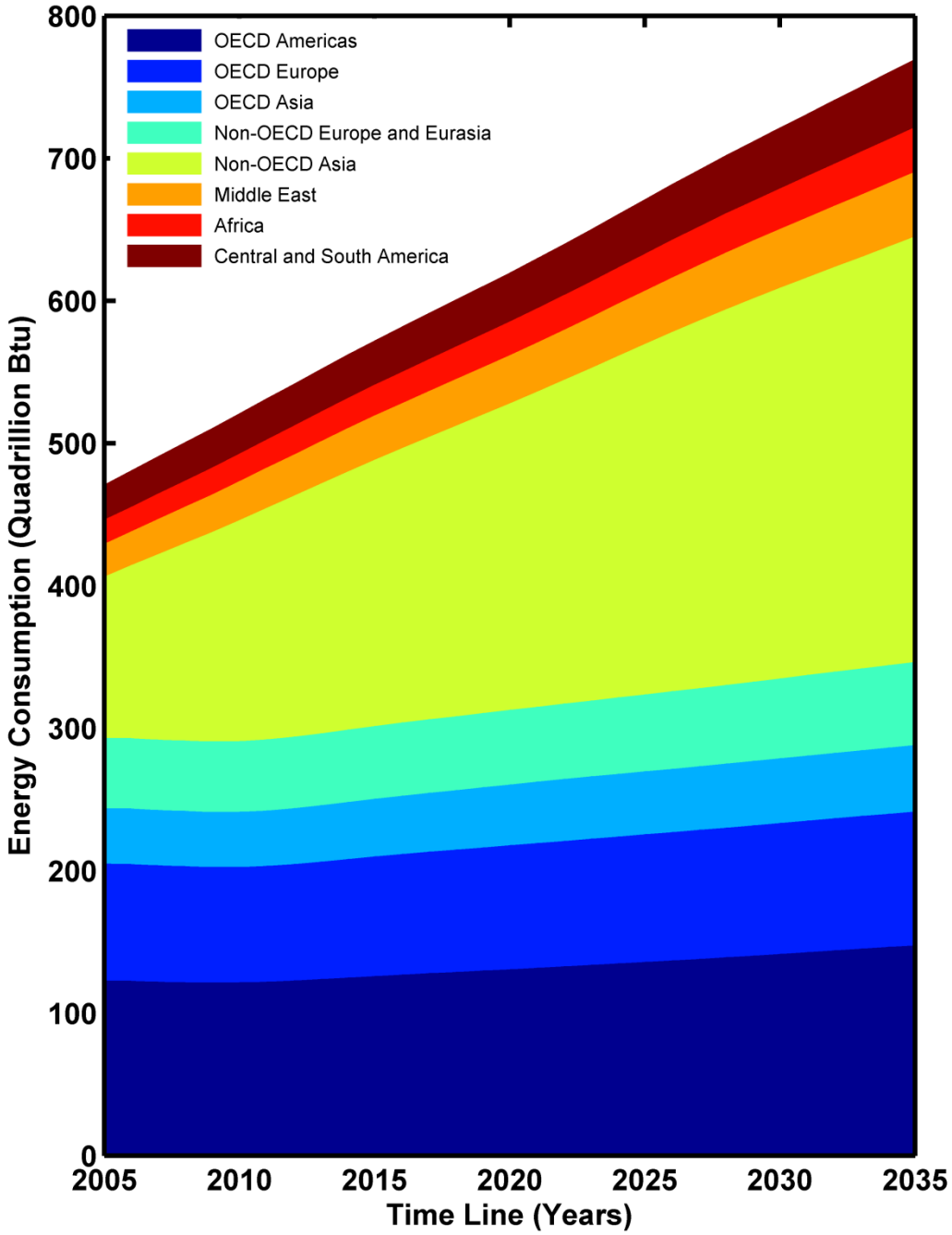


**Figure 1-3** World energy consumption (in British Thermal Units (Btu)) according to regions from 2005 to 2011 and projected consumption between 2011 and 2035.[4]

## 1.2 Major Energy Sources and Consumption Forms

The consumption of all energy sources have been increasing and the projections show that this will continue in the future as it can be seen in figure 1-4 which summarizes the broad international spectrum of energy. Expectations on the oil prices indicate that oil prices will always be relatively high so increase in consumption of oil as energy source is projected to remain at an average annual rate of 1% during 2005 and 2035 period as given in the figure.[4] Whereas consumption of renewable energy sources are projected to have the highest average annual rate of 2.8%.[4] In respect of the above projections, it is expected that the total share of the oil in world energy consumption will decrease 5%. Other fossil fuel sources such as coal and natural gas are projected to increase with rates of 1.6% and 1.5% respectively. Most of these increases will again be in non-OECD countries. These countries have been using and are projected to use coal as a cheaper replacement for more expensive energy sources; China alone accounts the 76% of the net increase in coal consumption and India and the rest of non-OECD Asia account for 19% of the world increase.

In figure 1-5a, world end-use energy consumption according to energy forms is given. As it can be seen from the figure, despite the projected relatively high prices oil is expected to remain as the mostly consumed energy form. On the other hand, electricity is projected to have the highest average annual increase rate, 2.3%. Most of this increase in the electricity consumption will be in non-OECD countries because of raising living-standards and expansion of infrastructures due to both their growing economies and populations (Figure 1-2). In order to supply this increasing demand, electricity power

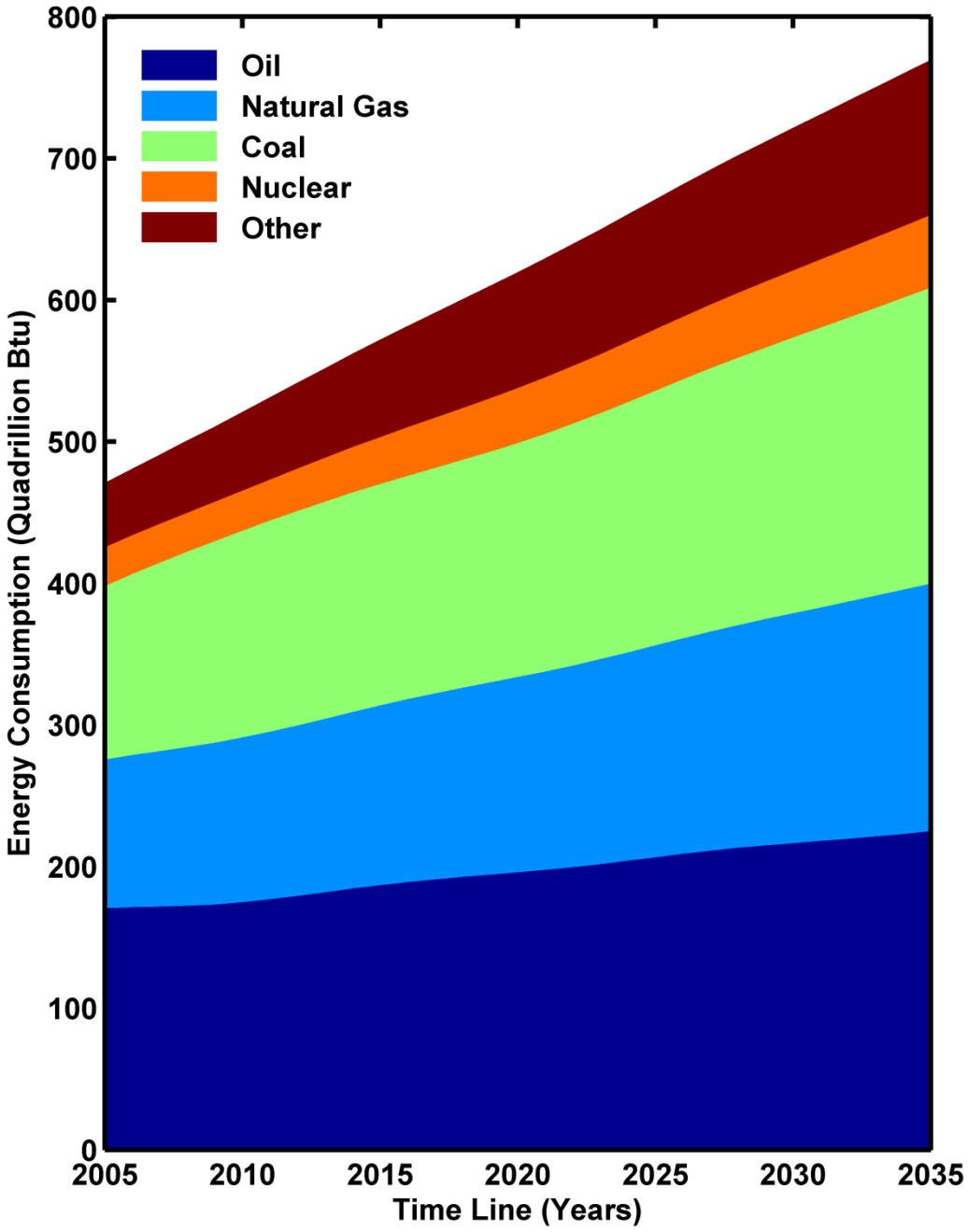


**Figure 1-4** World energy consumption (in Btu) according to major fuel sources from 2005 to 2011 and projected consumption between 2011 and 2035.[4]

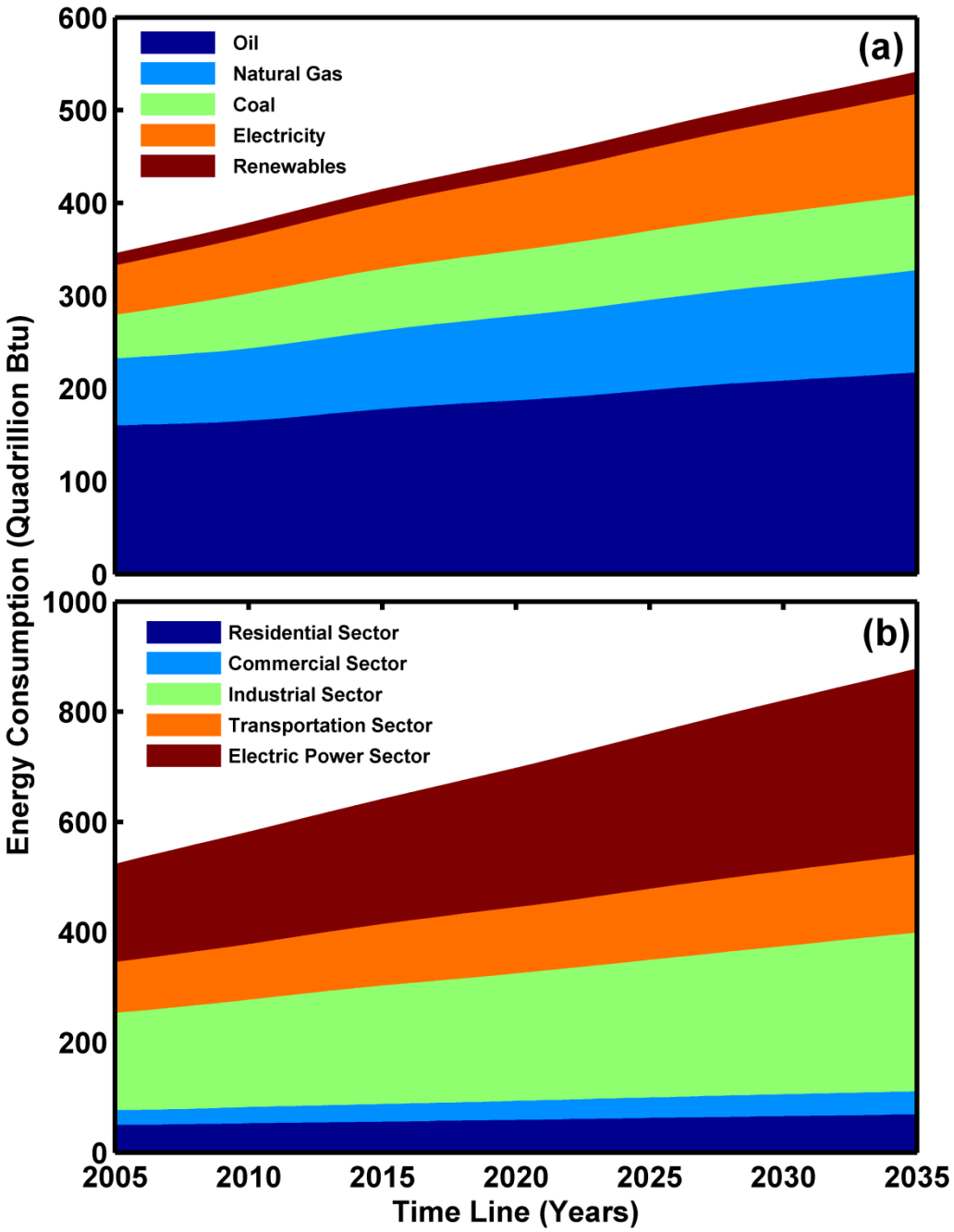


**Figure 1-5** (a) World end-use energy consumption (in Btu) according to major energy forms and (b) world energy consumption (in Btu) according to sectors during period 2005 to 2011 and projected consumption between 2011 and 2035[4]

sector is projected to have the highest energy consumption percentage compared to other major sectors at the end of this period in 2035 as given in figure 1-5b. Currently, fossil based fuels sources such as coal, natural gas and oil provide the largest share of world electricity generation (Figure 1-6a). The consumption of oil for electricity generation is expected to decline during this period due to projections on the oil prices indicates that the prices will remain relatively high. On the other hand, the consumption of coal and natural gas for electricity generation is projected to increase during the same period because of increasing consumption on non-OECD countries, low prices and broad range of availability. During the same period, electricity generation from nuclear power is also projected to have a slight increase which has lots of uncertainties because of the replacement of old power plants by their new counters, concerns about plant safety, and radioactive waste disposal. Although their increase in the net consumption amounts, their percentages in world total fuel consumption for electricity generation is projected to decline because world electricity generation from renewable energy is expected to increase almost 150% with an average annual increase rate of 3% during the same period.[4] World total electricity generation according to renewable energy sources in the same period is given in figure 1-6b. It can be seen from the figure that consumption in all renewable sources have been increasing and are projected to increase due to Government policies and incentives throughout the world support the rapid construction of renewable generation facilities. Worldwide, hydroelectricity and wind are the two largest contributors to the increase in global renewable electricity generation and solar power generation is projected to be the fastest-growing contributor among renewable sources.

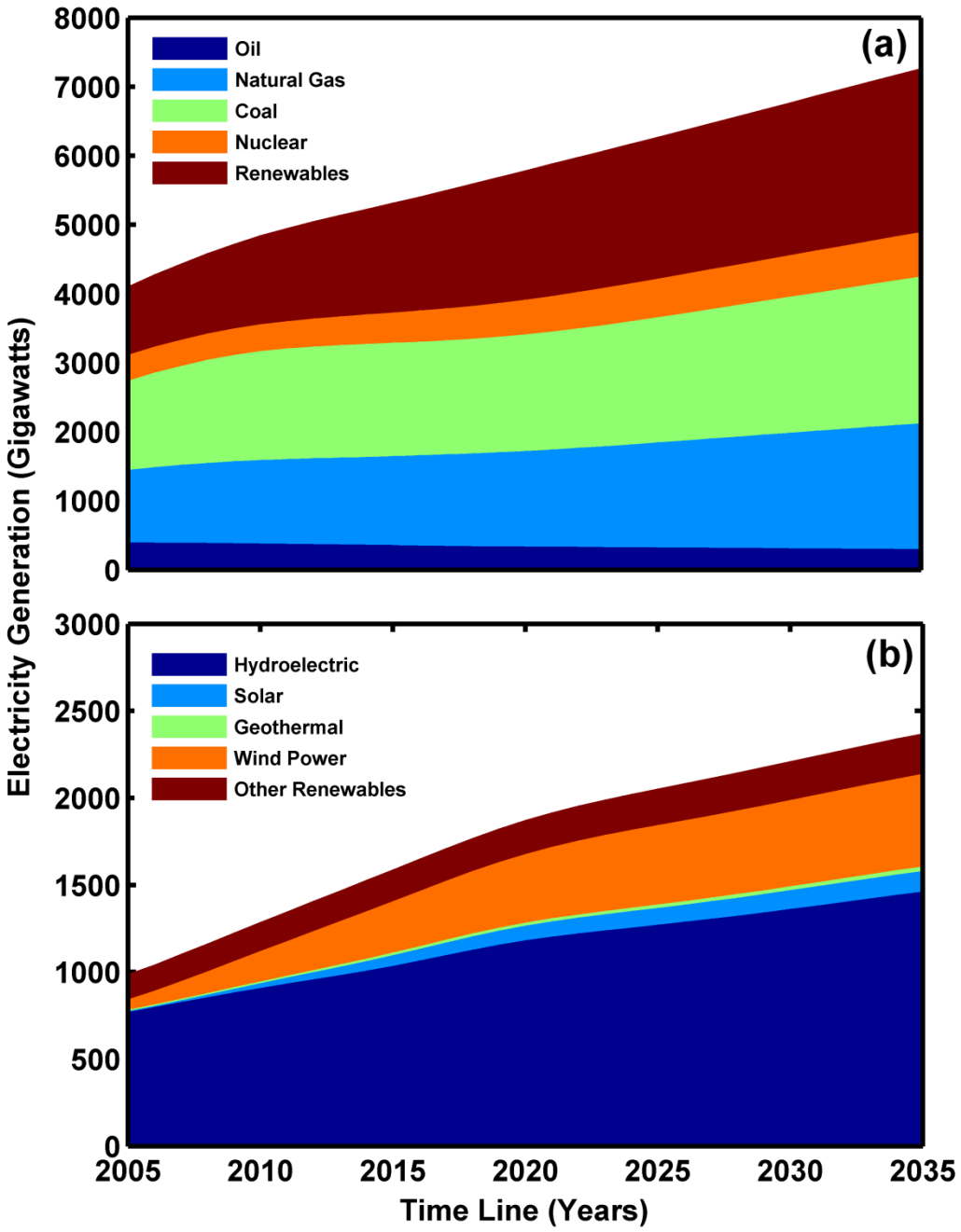


**Figure 1-6** (a) World electricity generation capacity (in Gigawatts) according to major energy sources and (b) world electricity generation capacity (in Gigawatts) according to renewable energy sources during period 2005 to 2011 and projected capacity between 2011 and 2035[4]

### 1.3 Future Concerns on Oil Supplies and Global Climate Change

Oil is the most important fossil fuel, and the world economies are dependent on it as it has the world wide highest consumption (Figure 1-4), and since all kinds of transport rely on oil. Such high dependency on oil as energy source brings the concerns on future availability of oil supplies. In figure 1-7 smoothed annual discoveries of oil as seen by Exxon is given[5]. The major result from the figure is that world oil discoveries has peaked in 1960s and it has been continuously declining since then and is projected to keep declining in the future and diminish by 2040s[5]. Also in figure 1-7, world oil production is given and as it can be seen from the figure, it has been increasing exponentially since 1960s following the peak oil discoveries except for the global oil crisis during period 1970 – 1980. If the production curve is crudely extrapolated according to the increase in the world oil consumption given in figure 1-4, a supply gap which can hardly be closed will be created. This situation is almost the same for all fossil fuel sources[5].

Besides on fossil fuel supplies, concerns on climate change will also force humankind to change energy consumption patterns by reducing significantly the consumption of fossil fuels. Because anthropogenic emissions of $CO_2$ result primarily from the combustion of fossil fuels, consumption of these fuels is at the center of the climate change debate. In figure 1-8, world energy-related $CO_2$ emissions according to regions during period 2005 to 2011 and projected emissions between 2011 and 2035 is given. As it can be seen from the figure, world energy-related $CO_2$ emissions increase from 30.2 billion metric tons in 2008 to 35.2 billion metric tons in 2020 and 43.2 billion

metric tons in 2035.[4] Much of the growth in emissions is attributed to non-OECD nations that continue to rely heavily on fossil fuels to meet fast-paced growth in energy demand.

$CO_2$ in the atmosphere causes greenhouse effect which keeps the solar radiated heat in so increases the global average temperatures. World had cycles of these temperature increases and following ice ages in the history. Besides the nature itself anthropogenic emission of $CO_2$ contributes to this natural increase in the global average temperature by causing increase in the $CO_2$ concentration. In figure 1-9, the global average $CO_2$ concentration and global average temperature anomaly according to years are given.[6, 7] As it can easily be seen from the figure, $CO_2$ builds-up in the atmosphere. Anomaly level in the global average temperature increases in the positive direction parallel to this build-up. This can be taken as a strong proof of dependency of global warming on $CO_2$ emissions due to combustion of fossil fuels.

Global warming is a very serious problem. An increase in global temperature will cause sea levels to rise and will cause more frequent occurrence of extreme weather events including heat-waves, droughts and heavy rainfall events, species extinctions due to shifting temperature regimes, and changes in agricultural yields. These catastrophic disasters will cause billions of dollars of economic damage to the governments, cause mass-human-migration to more habitable regions and etc. The threat of global warming caused by the burning of fossil fuels brings the necessity to change our energy economy by reducing the use of fossil fuels and by introducing renewable energy sources.

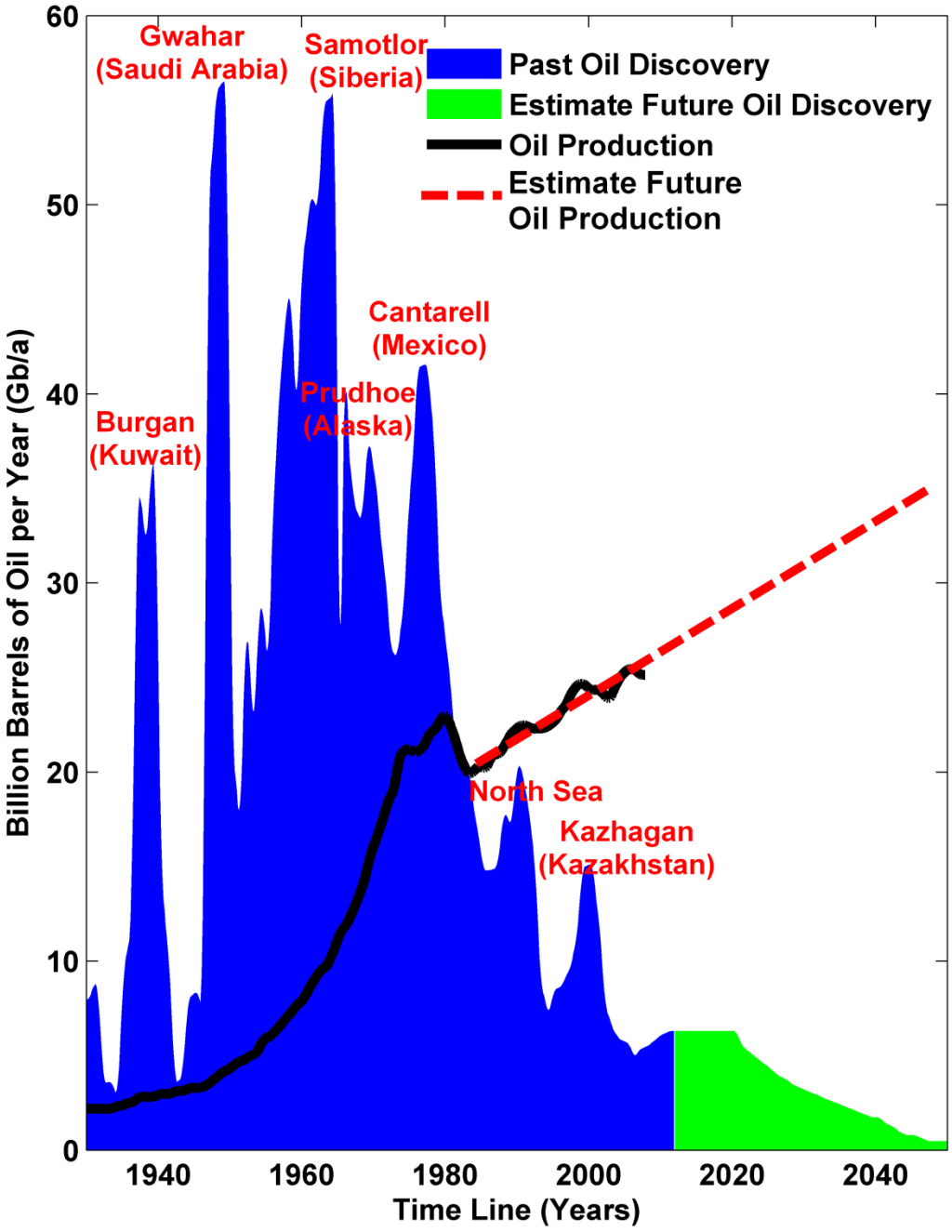


**Figure 1-7** Peak oil: smoothed annual discoveries of oil as seen by Exxon, past discoveries, and projected future discoveries versus past and projected future world oil production.[4, 5]

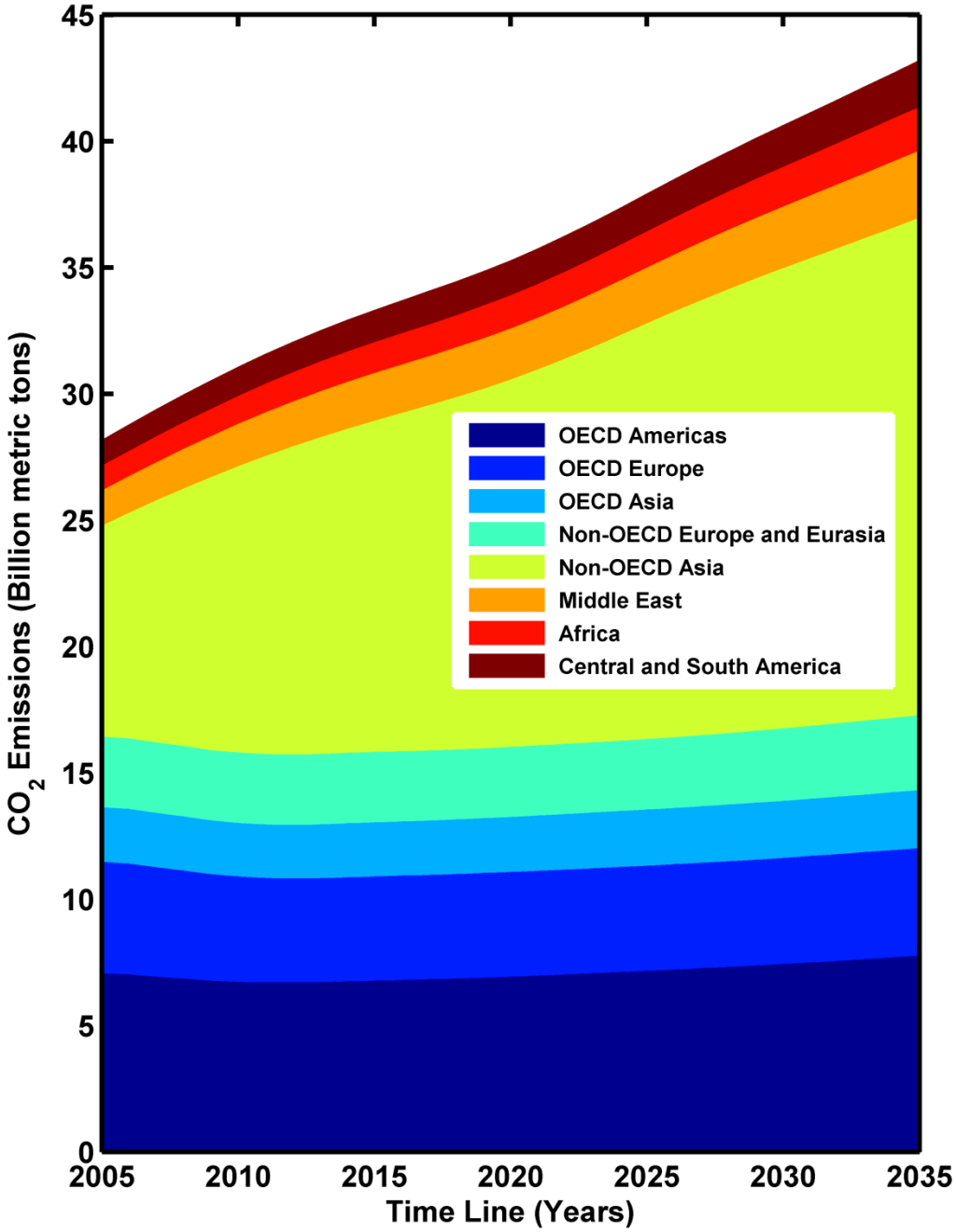


**Figure 1-8** World energy-related CO2 emissions (in Giga metric tons) according to regions during period 2005 to 2011 and projected emissions between 2011 and 2035.[4]

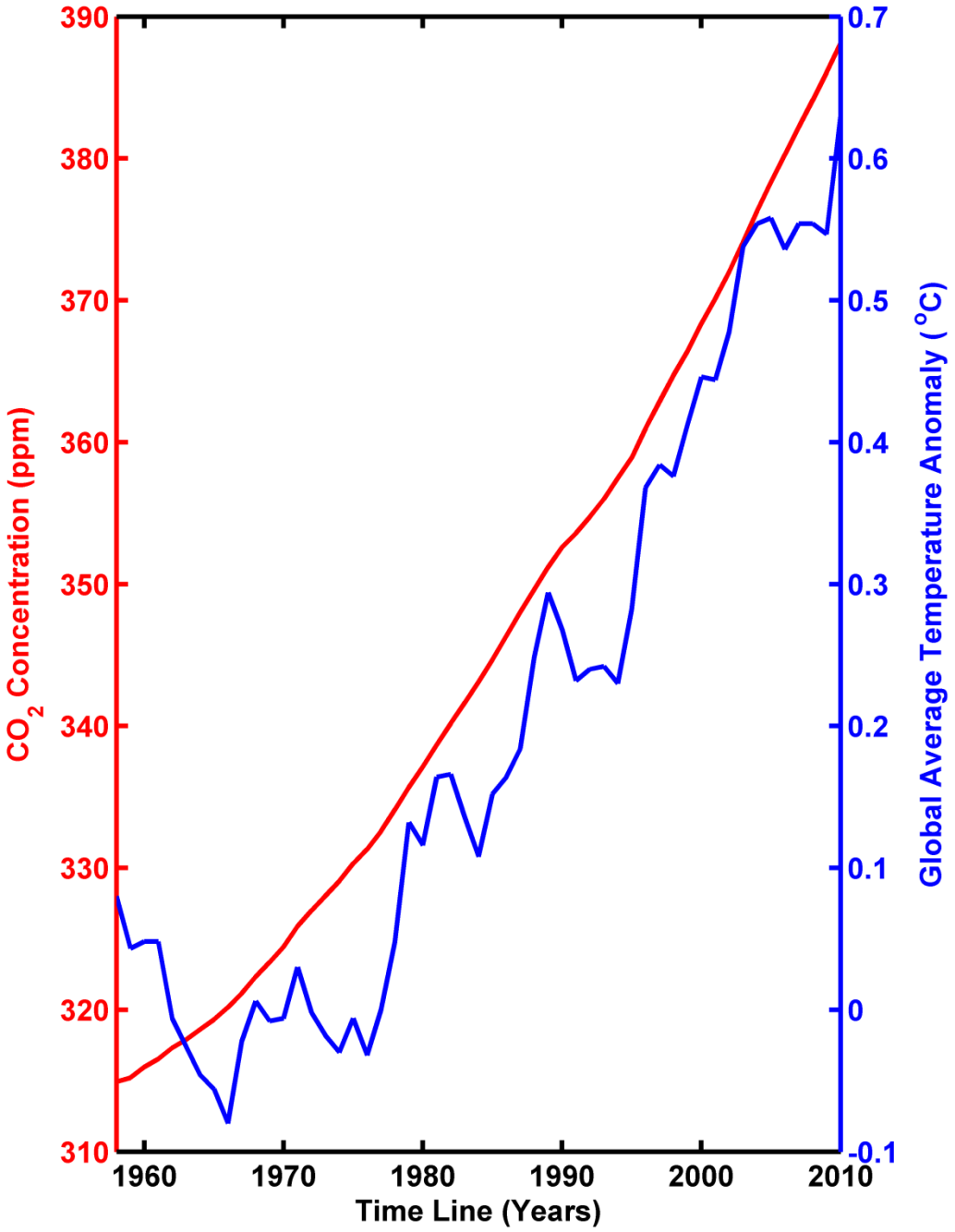


**Figure 1-9** Global average $CO_2$ concentration in the atmosphere[6] and global average temperature anomaly[7] according to years.

## 1.4 Renewable Energy

Renewable energy is basically the energy that comes from natural sources and can be derived from these natural sources such as hydropower, wind, sunlight and geothermal heat. Unlike fossil fuels, which are exhaustible, renewable energy sources regenerate constantly and can be sustained indefinitely.

Consumption of renewable energy sources is not new; human kind developed their civilization by burning wood which is one form of biomass until the discovery of the fossil fuels almost 150 years ago. As the consumption of the fossil fuels expanded, reliance on renewable energy sources declined. Now, a new era is on the doorstep for human kind: Fossil fuels, especially oil, are exhausting, prices increasing and earth is giving alarms for increasing $CO_2$ emissions with the increasing frequency of natural disasters all around the globe. Despite of all these negativity on the energy market, demand for energy is growing exponentially. Today, we are looking again at renewable energy sources to find new ways to use them to help meet growing energy needs and save the planet from a global climate change because the renewable energy is named so because it is environment friendly, can be sustained indefinitely and can replace non renewable energy sources like fossil fuels. With the increasing consciousness about the environmental care, consumption of renewable energy sources start growing by the end of $20^{th}$ century. The new millennium make people around the world to have more concerns on the insufficiency on the fossil fuels than the environment and as it can be seen in figure 1-6a, consumption of renewable sources for electricity generation started to increase and by 2035, this amount is projected to have the highest consumption

percentage among other energy sources. Unlike to the fossil fuel consumption projections which most of the increase in the consumption is projected to be in non-OECD countries due to high economical growth rates and increasing population, consumption of renewable energy sources is projected to increase globally (Figure 1-10). This shows that world is shifting to renewable energy sources because of the scarcity of exhausting fossil fuels, rising prices and environmental concerns.

Renewable energy sources come in several mainstream forms such as; hydropower, wind power, geothermal heat, solar energy and etc.

*Hydropower:* Hydropower is one of the oldest sources of energy. It was used thousands of years ago to turn a paddle wheel for purposes such as grinding grain. It is the renewable energy source that produces the most electricity in the world (Figure 1-6a, b). It has the highest consumption percentage, 60%, among other renewable energy sources. Hydropower is mainly the mechanical energy of moving water. The amount of available energy in moving water is determined by its flow or fall. The electric energy from water is mainly produced via the water flows through a pipe then pushes against and turns blades in a turbine to spin a generator. This can be achieved by converting the potential energy of water stored in the dams built across rivers, the kinetic energy of run-of-the-river or ocean waves and etc. The main drawback of hydroelectric generation is the power plants have to be built on appropriate water sources which is may be in great distances to big consumption areas.

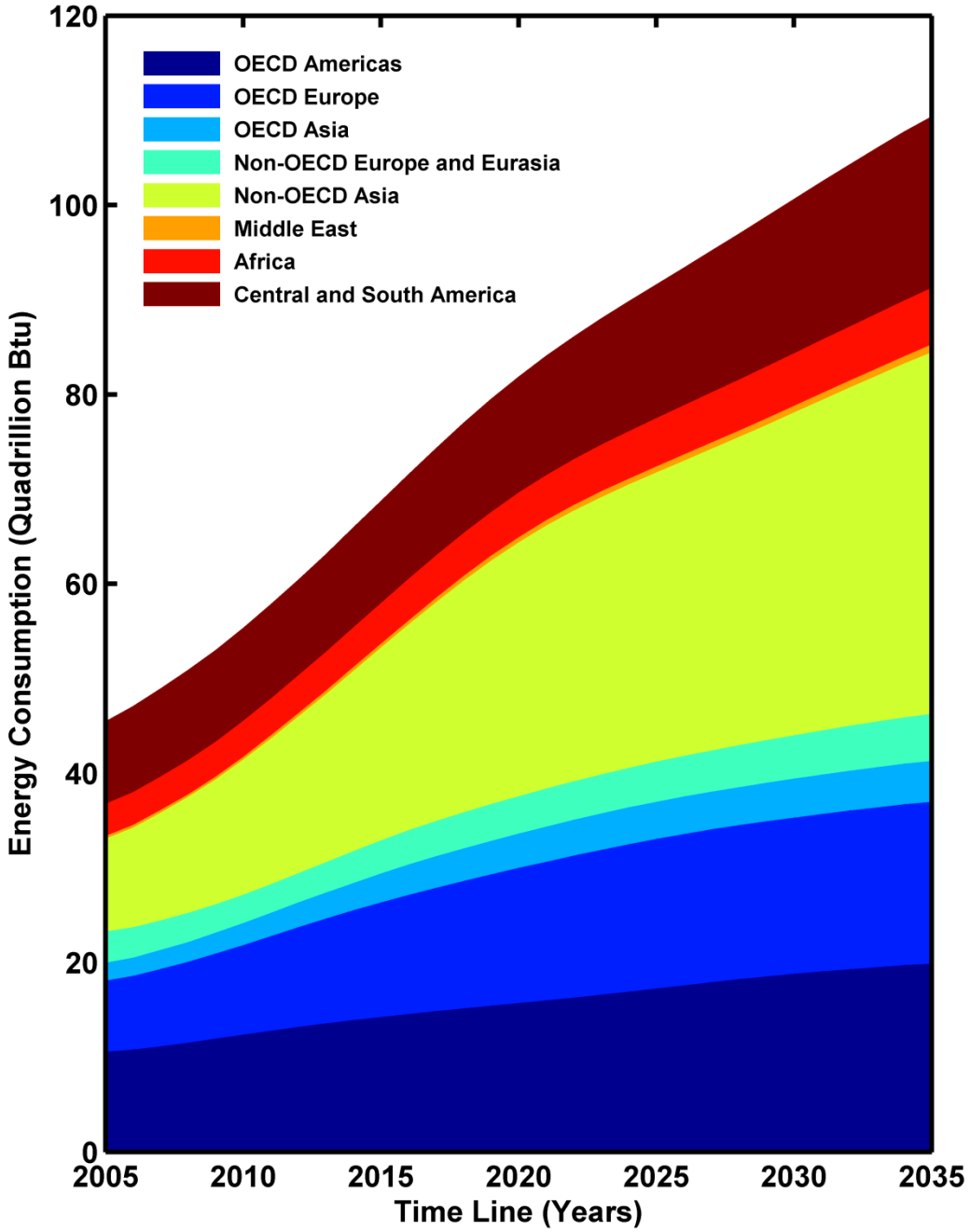


**Figure 1-10** World renewable energy consumption (in Btu) according to regions from 2005 to 2011 and projected consumption between 2011 and 2035.[4]

*Wind Power:* Wind is simply air in motion. It is caused by the uneven heating of the Earth's surface by the sun. The energy production mechanism is almost the same with the hydroelectricity power plants; instead of water wind turbines use air flow, converts the kinetic energy of air into electricity. The power output of a wind turbine is a function of the cube of the wind speed, so as wind speed increases, power output increases dramatically.[8] Areas where winds are stronger and more constant, such as offshore and high altitude sites, are preferred locations for wind farms. Wind power has the second largest consumption percentage among the renewable energy sources (Figure 1-6b). Even though wind is free, the wind cannot always be predicted. Another disadvantage is that these wind farms are usually near the coast, and this means higher land prices. Some other disadvantages of these wind farms are they can affect television reception for people in close proximity to the farm, can be noisy, can kill birds and etc.

*Geothermal Heat:* Geothermal energy is energy obtained by trapping the heat of the earth itself. It is expensive to build a power station but operating costs are low resulting in low energy costs for suitable sites. Three types of power plants are used to generate power from geothermal energy: dry steam, flash, and binary. Dry steam plants take steam out of fractures in the ground and use it to directly drive a turbine that spins a generator. Flash plants take hot water out of the ground, and allow it to boil as it rises to the surface. Then, they separate the steam phase in steam/water separators and then run the steam through a turbine. In binary plants, the hot water flows through heat exchangers, boiling an organic fluid that spins the turbine. The main drawback of this renewable energy source is the lack of available sites to build power plants, high costs on the construction of power

plants and the distance of these sites to the energy consumption areas. Because of these reasons, electricity generation from geothermal heat has the least percentage among other renewable energy sources (Figure 1-6b).

*Solar Energy:* Solar energy is the energy derived from the sun through the form of solar radiation. The sun has produced energy for billions of years. It has been harnessed by humans since ancient times using a range of ever-evolving technologies. However it is now that mankind has realized its importance as a safe and inexpensive energy source. The energy from the sun can be used to overcome the energy crisis. Solar energy is free and it is everywhere. The Earth receives 174 petawatts (PW) of incoming solar radiation at the upper atmosphere.[9] Approximately 30% is reflected back to space while the rest is absorbed by clouds, oceans and land masses. The energy capacity of the sun is examined that the earth receives more energy from sun in one hour than it is using in one year.[10] The solar irradiance map of the Earth is given in figure 1-11.[11] As it can be seen from the map, the solar irradiance is powerful enough to be used as an energy source at least 75% of the whole lands. This huge amount of energy can be converted into other forms of energy, such as heat and electricity by using heat engines which wither generate electricity by concentrating solar energy to heat a fluid and produce steam that is used to power a generator or use the hot fluid directly and photovoltaic devices which converts sunlight directly into electricity.

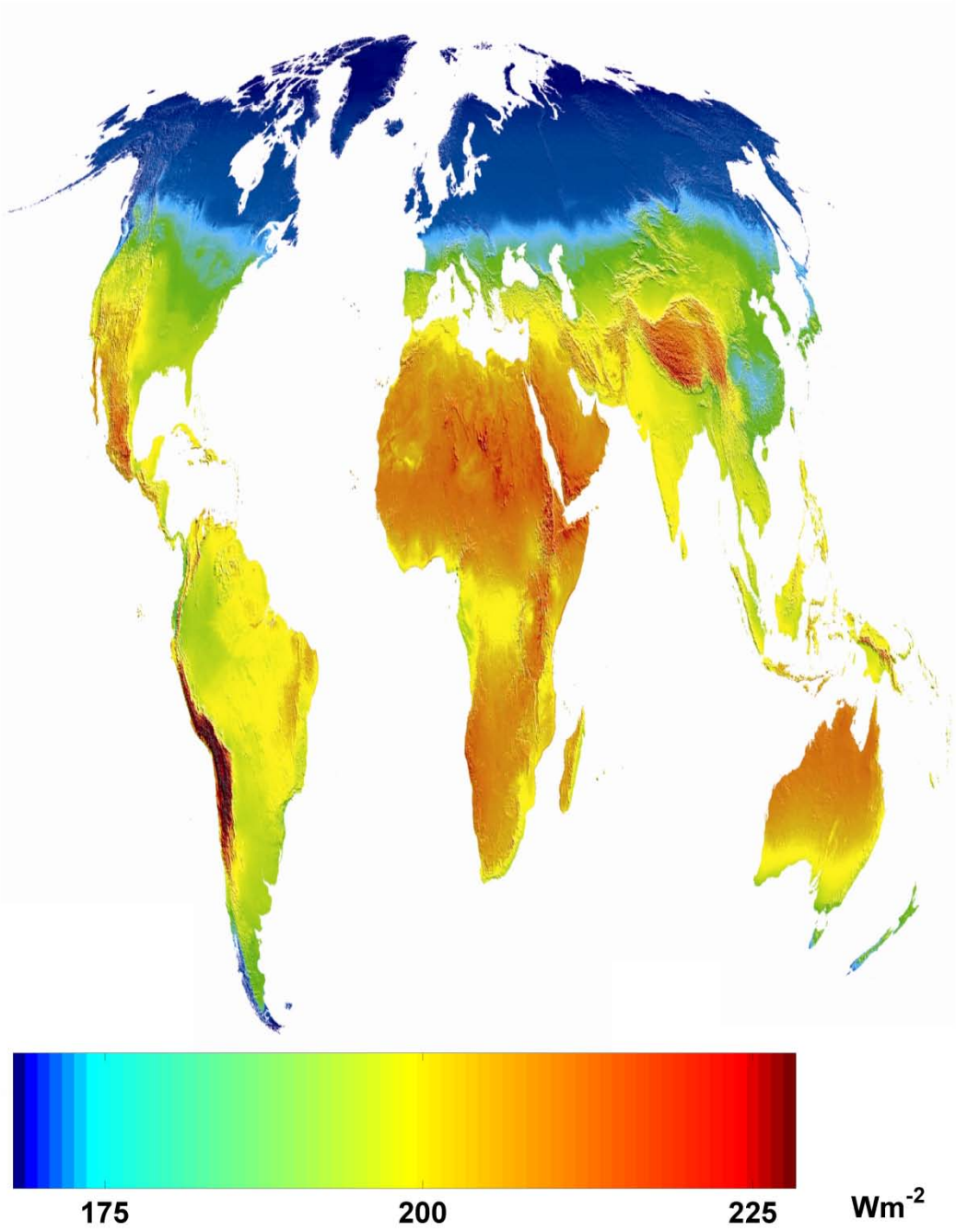


**Figure 1-11** Global mean solar irradiance map (map is modified from the original map developed by 3TIER, www.3tier.com)[11]

Generation of electricity from solar energy has the highest increase rate among other renewable energy sources since 2005 (Figure 1-6b). Throughout the world, almost all of the countries have application projects and research on solar electricity generation. In figure 1-12, world solar electricity generation capacity according to regions is given. In all regions of the world, the solar generation capacity increases exponentially since 2005. This is projected to saturate after 2015 however the increase is projected to continue. Most of this increase comes from OECD-Europe and non-OECD Asia countries. Ironically, the countries having the lowest solar irradiance are projected to increase their solar generation capacity higher than the rest of the world, whereas, the countries placed in the regions receiving the highest solar irradiance such as; middle-east, Africa and Central and South America has the lowest capacity and the increase rates. This correlates with the economic power of the countries and is a strong proof that the solar energy generation is still too expensive.

Cost is still the major drawback in all of the renewable energy sources. In order to overcome this, more research on photovoltaic devices is needed to increase the device efficiency, make the mass fabrication of the devices cheaper and develop new, cheaper and easy to implement materials. This thesis, discusses on the photovoltaic devices grouping them under inorganic and organic type of device, new mathematical model for organic photovoltaic device characterization, improving the device efficiency for organic materials by introducing inorganic materials in the device structure such as; metallic surface plasmons and reducing the cost for photovoltaic devices by introducing a new material, graphene, as the low-cost, transparent anode contact material.

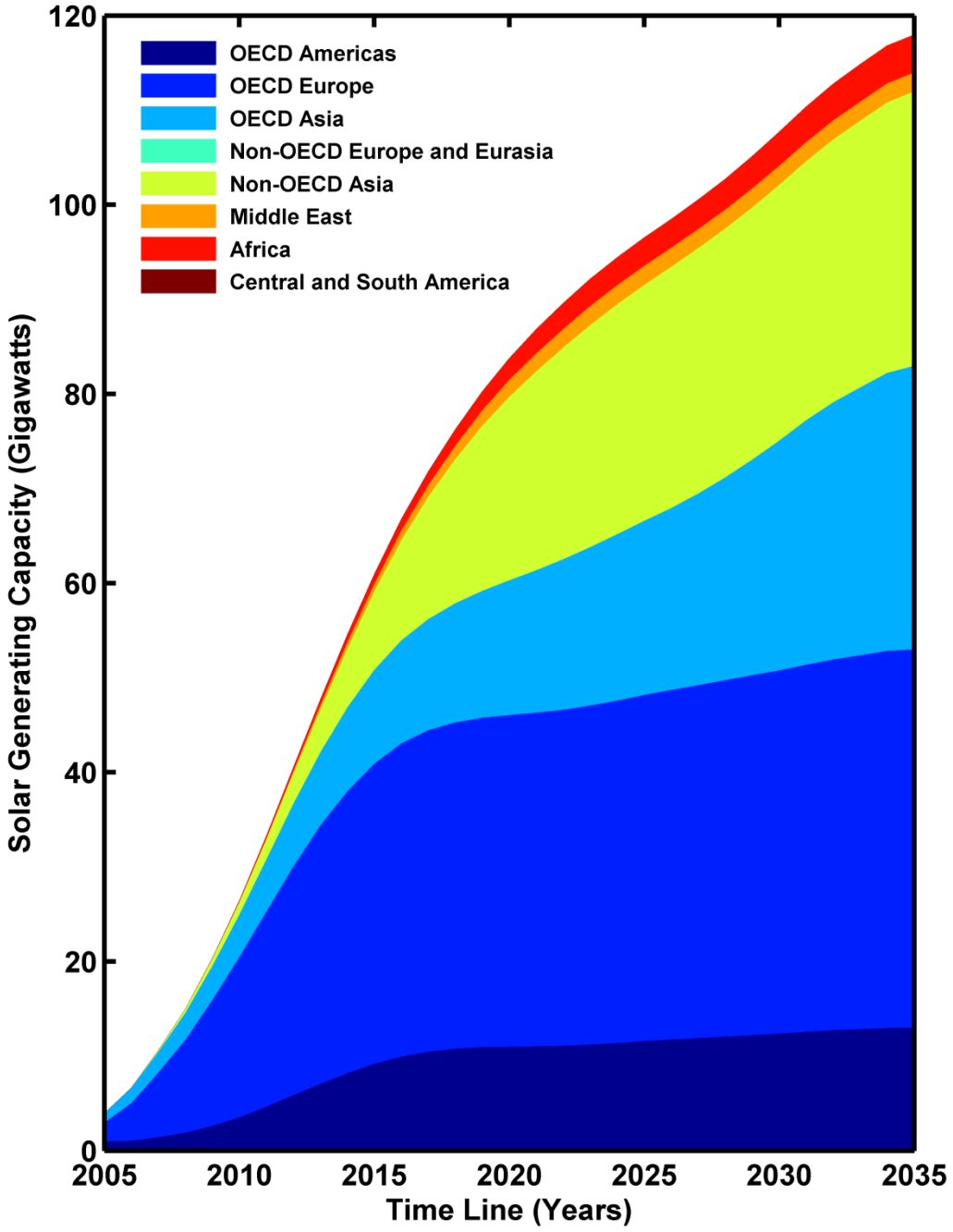


**Figure 1-12** World solar electricity generation capacity (in Gigawatts) according to regions during period 2005 to 2011 and projected capacity between 2011 and 2035[4]

## Chapter 2:

## Photovoltaic Devices

### 2.1 Introduction

Photovoltaic (PV) device [12-16], i.e. solar cell, is a solid state electrical device that converts the energy of light directly into electricity by the photovoltaic effect.[17, 18] Devices are described as PV devices when the light source is not necessarily sunlight. PV devices are used for detecting any kind of electromagnetic radiation having wavelengths from 10-to-100,000 nm, i.e. light spectrum from ultraviolet (UV)-to-far-infrared (IR)[19-21] or generating electricity out of light. In structural basis all PV devices are photodiodes which work on different operation modes.[22, 23] PV devices produce direct current electricity from light, which can be used to power equipment in solar cell mode, detect light or measure the intensity of the light source in photodiode/photo-detection mode. In photo-detection mode the diode is often reverse biased. This increases the width of the depletion layer[24], which decreases the junction's capacitance resulting in faster response times. The reverse bias induces only a small amount of current along its direction while the photocurrent remains virtually the same. For a given spectral distribution, responsivity[24] of the photodiode, the photocurrent is linearly proportional to the irradiance spectra.[24] In solar cell mode, the diode is used in unbiased operating mode in which current through the device is entirely due to the incident photon energy. The flow of photocurrent out of the device is restricted and a voltage builds up. This mode exploits the photovoltaic effect. A traditional solar cell is

just a large area photodiode which is used in the unbiased mode for making it to generate its own voltage and current.

This chapter discusses about how PV devices work, brief history of the development of PV devices and types of PV devices as an introduction for the photovoltaic technology. Then, for technical background, fabrication and characterization of PV devices according to operation mode are discussed in detail.

## 2.2 Photovoltaic Effect

The term "photovoltaic" comes from the Greek φῶς (phōs) meaning "light", and "voltaic", from the name of the Italian physicist Volta, after whom a unit of electro-motive force, the volt, is named. The term "photo-voltaic" has been in use in English since 1849.[25] Photovoltaic is a method of generating electrical power by converting solar radiation into direct current electricity using semiconductors that exhibit the photovoltaic effect.[26-28] It is the most direct way to convert energy of photons into electricity. In 1839, while experimenting with an electrolytic cell made up of two metal electrodes, a French experimental physicist named Alexandre-Edmond Becquerel, only nineteen years old at the time, discovered that when exposing certain materials to sunlight he could generate a weak electrical current. Becquerel named this phenomenon the "photovoltaic effect".[28-30] The photovoltaic effect is the basic process in which a device converts sunlight into electricity. It is quite generally defined as the emergence of an electric voltage between two electrodes attached to a solid or liquid system upon shining light onto this system. The explanation relies on ideas from quantum theory.

Light is made up of packets of energy, called photons, whose energy depends only upon the frequency, or color, of the light. The energy of visible photons is sufficient to excite electros, bound into solids, up to higher levels where they are freer to move. Normally, when light is absorbed by matter, photons are given up to excite electrons to higher energy states within the material, but the exited electrons quickly relax back to their ground state. In a photovoltaic device, however, there is some built-in asymmetry which pulls the excited electrons away before they can relax, and feeds them to an external circuit.

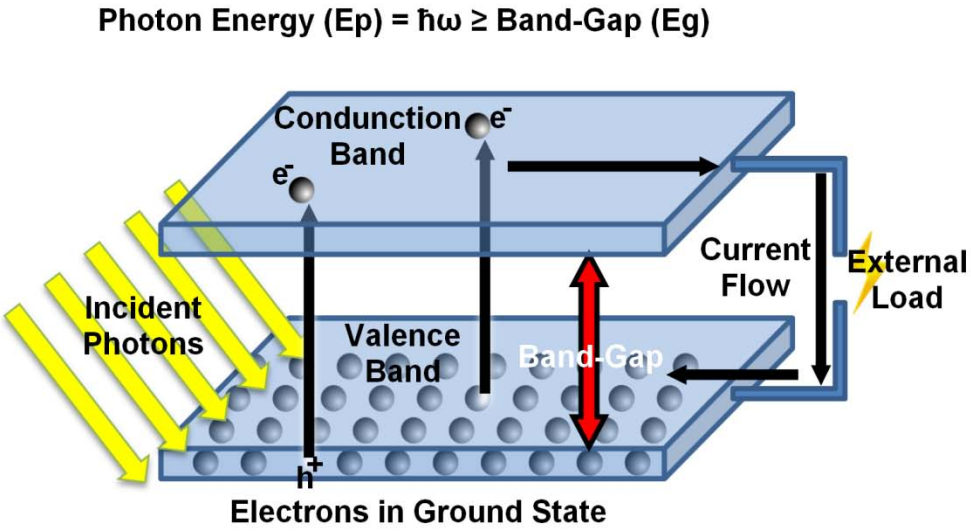


**Figure 2-1** Schematic of photovoltaic effect. Electrons are pumped by the photons from the valence band to the conduction band. There the electrons are extracted by a contact selective to the conduction band at a higher energy and delivered to the outside world via wires, where they do some useful work, then are returned to the valence band at a lower energy by a contact selective to the valence band.

The physics behind the basis of photovoltaic operation is that the materials which have weakly boned electrons occupying band energy called the valence band. When energy exceeding a certain threshold, called the band gap energy, is applied to a valence electron, the bonds are broken and the electron is somewhat “free” to move around in a new energy band called the conduction band where it can “conduct” electricity through the material. Thus, the free electrons in the conduction band are separated from the valence band by the band gap. This energy needed to free the electron can be supplied by photons. Figure 2-1 shows the idealized relation between energy and the spatial boundaries. When device is exposed to light, photons hit valence electrons, breaking the bond and pumping them to the conduction band. There, the contact that collects conduction-band electrons drives such electrons to external circuit. The electrons lose their energy by doing work in the external circuit. They are restored to the device by return loop circuit via second contact, which returns them the valence band with the same energy they started with. The movement of these electrons in the external circuit and contacts is called the electric current.

### 2.3 History of Photovoltaic Devices

It was not until 1883 which is almost fifty years after the first discovery of photovoltaic effect in 1839 by Becquerel that the first photovoltaic cell was built, by Charles Fritts, who coated the semiconductor selenium with an extremely thin layer of gold to form the junctions. The device was only around 1% efficient. In 1888, Russian physicist Aleksandr Stoletov built the first photoelectric cell based on the outer photoelectric effect discovered by Heinrich Hertz earlier in 1887. In 1905, Albert

Einstein described the nature of light and the photoelectric effect on which photovoltaic technology is based, for which he later won a Nobel prize in physics.[31] The modern photovoltaic cell was developed in 1954 at Bell Laboratories.[18] The highly efficient solar cell was first developed by Daryl Chapin, Calvin Souther Fuller and Gerald Pearson in 1954 using a diffused silicon p-n junction.[32]

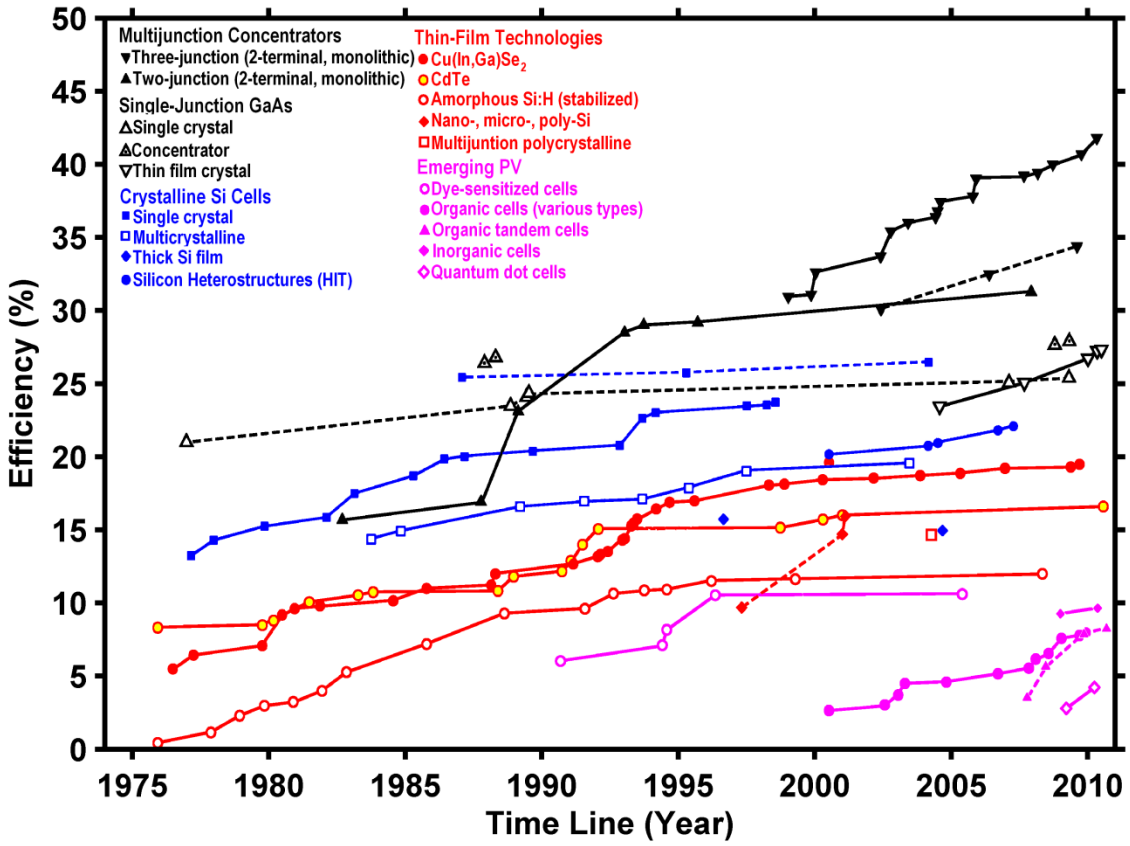


**Figure 2-2** Research Cell Efficiency Plot for Various Photovoltaic Technologies 1976-2011. Figure is modified from the original figure prepared by Lawrence Kazmerski, National Renewable Energy Laboratory (NREL)[33]

The first generation of solar cells, based upon silicon based p-n junction cells. These solar cells use a single junction of extremely pure silicon for extracting energy from photons, and have a theoretical efficiency maximum of 33%[34] (Figure 2-2).

In the early 1960s, silicon based solar cells have approximately 11% efficiency. They were relatively inexpensive, and suitable for the low power and limited lifetime application. The conversion efficiency of standard silicon solar cells ranges around 15% under standard test conditions. In the last 50 years, there have been many enhancements in the silicon cell technology to improve their efficiency. During this time, research is mainly focused on better light absorption, extremely thin cells with back-surface reflectors for internal light trapping, and passivated cell surfaces to reduce losses due to recombination effects. The highest measured efficiency for a large-area crystalline silicon solar cell stands at 25% (Figure 1-2). In spite of the complicated fabrication processes of these cells and high cost, they still dominate the solar cell market. In 2007, first generation solar cells accounted for 89.6% of commercial production. It is not thought that first generation cells will be able to provide energy more cost effective than fossil fuel sources.

The high cost of the first generation cells give rise to the development of the second generation solar cells. This so called ‘thin-film’ solar cell technology was first made by Wolf and Spitzer in mid 1980s.[35] This generation of solar cells has been developed based on materials of crystalline silicon, micro-amorphous (micromorphous) silicon,[36] copper indium gallium selenide, Cu,(In,Ga)$Se_2$, (CIGS) [37], and cadmium

telluride (CdTe).[38] They are significantly cheaper to produce than first generation cells but have lower efficiencies. In 2007, thin-film silicon production represented 5.2% of total market share. In 2010, CIGS based cells have the highest reported efficiency with is 20% (Figure 1-2).

Light concentrators increase efficiencies and reduce the cost/efficiency ratio. The two types of light concentrators are refractive lenses like Fresnel lenses and reflective dishes. With the improvement of these devices, light arriving on a large surface can be concentrated on a smaller cell. The intensity concentration ratio is the average intensity of the focused light divided by 0.1 W/m². The final output current of the multi-junction cell will be multiplied by this ratio under concentrated illumination.[39, 40]

Concentrator enhanced cells produce the highest efficiencies seen to date. Three-layer cells are fundamentally limited to 63%, but existing commercial prototypes have already demonstrated over 40%[41] (Figure 2-2). These cells capture about 2/3 of their theoretical maximum performance, so assuming the same is true for a non-concentrated version of the same design; one might expect a three-layer cell of 30% efficiency. This is not enough of an advantage over traditional silicon designs to make up for their extra production costs. For this reason, almost all multi-junction cell research for terrestrial use is dedicated to concentrator systems, normally using mirrors or fresnel lenses.

Using a concentrator also has the added benefit that the number of cells needed to cover a given amount of ground area is greatly reduced. A conventional system covering 1 m² would require 625 16 cm² cells, but for a concentrator system only a single cell is

needed, along with a concentrator. The argument for concentrated multi-junction cells has been that the high cost of the cells themselves would be more than offset by the reduction in total number of cells. However, the downside of the concentrator approach is that efficiency drops off very quickly under lower lighting conditions. In order to maximize its advantage over traditional cells and thus be cost competitive, the concentrator system has to track the sun as it moves to keep the light focused on the cell and maintain maximum efficiency as long as possible. This requires an expensive solar tracker system, and offsets the potential advantages offered by multi-junction cells.

After the discoveries of new organic photovoltaic materials, a third generation of photovoltaic devices based on organic solar cells became a very hot topic for scientists for the last decade. These so called ‘plastic cells’ became a very promising solution to the upcoming energy problem because of their flexible structures, low fabrication costs, ease of processing and adjustable electrical properties.

Still in research phase, third generation cells has moved beyond silicon-based cells by using the evaluation of materials innovation technology. Targeted conversion efficiency for this organic material based generation is 30-to-60%. Although many scientists came up with different materials and structures to this energy harvesting problem using organic solar cells, the efficiencies of these devices are still not good enough for commercialization. It is recently reported that efficiencies of these devices have increased over 5%.[42, 43] Increasing the performance of these plastic cells is dependent on understanding and suppressing the effects of the performance limitations.

## 2.3 Types of Photovoltaic Cell Materials

Different materials display different efficiencies and have different costs. Materials for efficient solar cells must have characteristics matched to the spectrum of available light. Some cells are designed to efficiently convert wavelengths of solar light that reach the Earth surface. However, some solar cells are optimized for light absorption beyond Earth's atmosphere as well. Light absorbing materials can often be used in multiple physical configurations to take advantage of different light absorption and charge separation mechanisms.

Materials presently used for photovoltaic solar cells include monocrystalline silicon (c-Si)[44-47], polycrystalline silicon[48-51], amorphous silicon (a-Si)[52-55], CdTe[56-59], copper indium selenide/sulfide (CIS)[60-64], and CIGS.[65-69]

Many currently available solar cells are made from bulk materials that are cut into wafers between 180-to-240 micrometers thick that are then processed like other semiconductors.

Other materials are made as thin-films layers, organic dyes[70], and organic polymers[71-75] that are deposited on supporting substrates. A third group are made from nano-crystals and used as quantum dots.[76-79] Silicon remains the only material that is well-researched in both bulk and thin-film forms.

### 2.3.1 Crystalline silicon

By far, the most prevalent bulk material for solar cells is crystalline silicon. Bulk silicon is separated into multiple categories according to crystal structure and crystal size in the resulting ingot, ribbon, or wafer.

*Monocrystalline Silicon (c-Si)[44]:* often made using the Czochralski process. Single-crystal wafer cells tend to be expensive, and because they are cut from cylindrical ingots, do not completely cover a square solar cell module without a substantial waste of refined silicon. Hence most c-Si panels have uncovered gaps at the four corners of the cells.

*Poly- or Multicrystalline Silicon (poly-Si or mc-Si)[47]:* made from cast square ingots — large blocks of molten silicon carefully cooled and solidified. Poly-Si cells are less expensive to produce than single crystal silicon cells, but are less efficient. US DOE data shows that there were a higher number of multicrystalline sales than mc-Si sales. Ribbon silicon[80-82] is a type of mc-Si; it is formed by drawing flat thin films from molten silicon and results in a multicrystalline structure. These cells have lower efficiencies than poly-Si, but save on production costs due to a great reduction in silicon waste, as this approach does not require sawing from ingots.

Analysts have predicted that prices of polycrystalline silicon will drop as companies build additional polysilicon capacity quicker than the industry's projected demand. On the other hand, the cost of producing upgraded metallurgical-grade silicon, also known as UMG Si, can potentially be one-sixth that of making polysilicon. Manufacturers of wafer-based cells have responded to high silicon prices in 2004-2008

prices with rapid reductions in silicon consumption. According to Jef Poortmans, director of IMEC's organic and solar department, current cells use between eight and nine grams of silicon per watt of power generation, with wafer thicknesses in the neighborhood of 0.200 mm. At 2008 spring's IEEE Photovoltaic Specialists' Conference (PVS'08), John Wohlgemuth, staff scientist at BP Solar, reported that his company has qualified modules based on 0.180 mm thick wafers and is testing processes for 0.16 mm wafers cut with 0.1 mm wire. IMEC's roadmap, presented at the organization's recent annual research review meeting, envisions use of 0.08 mm wafers by 2015.

### 2.3.2 Thin-Films

Thin-film technologies reduce the amount of material required in creating the active material of solar cell. Most thin film solar cells are sandwiched between two panes of glass to make a module. Since silicon solar panels only use one pane of glass, thin film panels are approximately twice as heavy as crystalline silicon panels. The majority of film panels have significantly lower conversion efficiencies, lagging silicon by two to three percentage points. Thin-film solar technologies have enjoyed large investment due to the success of First Solar and the, largely unfulfilled, promise of lower cost and flexibility compared to wafer silicon cells, but they have not become mainstream solar products due to their lower efficiency and corresponding larger area consumption per watt production. CdTe, CIGS and a-Si are three thin-film techologies often used as outdoor photovoltaic solar power production. CdTe technology is most cost competitive among them. CdTe technology costs about 30% less than CIGS technology and 40% less than a-Si technology in 2011.

*Cadmium Telluride (CdTe)[69]:* A CdTe solar cell uses a cadmium telluride thin film, a semiconductor layer to absorb and convert sunlight into electricity. The cadmium (Cd) present in the cells would be toxic if released. However, release is impossible during normal operation of the cells and is unlikely during fires in residential roofs. A square meter of CdTe contains approximately the same amount of Cd as a single cell Nickel-cadmium battery, in a more stable and less soluble form.

*Copper Indium Gallium Selenide (CIGS)[67]:* CIGS is a direct-bandgap material. It has the highest efficiency (~20%) among thin film materials. Traditional methods of fabrication involve vacuum processes including co-evaporation and sputtering.

*Gallium Arsenide (GaAs) Multijunction[83, 84]:* High-efficiency multijunction cells were originally developed for special applications such as satellites and space exploration, but at present, their use in terrestrial concentrators might be the lowest cost alternative in terms of $/kWh and $/W. These multijunction cells consist of multiple thin films produced using metalorganic vapour phase epitaxy. A triple-junction cell, for example, may consist of the semiconductors: GaAs, germanium (Ge), and Gallium indium phosphate (GaInP). Each type of semiconductor will have a characteristic band gap energy which, loosely speaking, causes it to absorb light most efficiently at a certain color, or more precisely, to absorb electromagnetic radiation over a portion of the spectrum. The semiconductors are carefully chosen to absorb nearly the entire solar spectrum, thus generating electricity from as much of the solar energy as possible. GaAs

based multijunction devices are the most efficient solar cells to date. In October 2010, triple junction metamorphic cell reached a record high of 42.3% (Figure 2-2).

*Light-Absorbing Dyes[70]:* Dye-sensitized solar cells (DSSCs) are made of low-cost materials and do not need elaborate equipment to manufacture, so they can be made in a DIY fashion, possibly allowing players to produce more of this type of solar cell than others. In bulk it should be significantly less expensive than older solid-state cell designs. DSSC's can be engineered into flexible sheets, and although its conversion efficiency is less than the best thin film cells, its price/performance ratio should be high enough to allow them to compete with fossil fuel electrical generation. The DSSC has been developed by Prof. Michael Grätzel in 1991 at the Swiss Federal Institute of Technology (EPFL) in Lausanne (CH).

Typically a ruthenium metalorganic dye (Ru-centered) is used as a monolayer of light-absorbing material. The dye-sensitized solar cell depends on a mesoporous layer of nanoparticulate titanium dioxide ($TiO_2$) to greatly amplify the surface area (200-to-300 $m^2/g$ $TiO_2$, as compared to approximately 10 $m^2/g$ of flat single crystal). The photogenerated electrons from the light absorbing dye are passed on to the n-type $TiO_2$, and the holes are absorbed by an electrolyte on the other side of the dye. The circuit is completed by a redox couple in the electrolyte, which can be liquid or solid. This type of cell allows a more flexible use of materials, and is typically manufactured by screen printing and/or use of Ultrasonic Nozzles, with the potential for lower processing costs than those used for bulk solar cells. However, the dyes in these cells also suffer from

degradation under heat and ultraviolet (UV) light, and the cell casing is difficult to seal due to the solvents used in assembly. In spite of the above, this is a popular emerging technology with some commercial impact forecast within this decade.

*Organic/Polymer Solar Cells[73]:* Organic solar cells are a relatively novel technology, yet hold the promise of a substantial price reduction and a faster return on investment. These cells can be processed from solution, hence the possibility of a simple roll-to-roll printing process, leading to inexpensive, large scale production.

Organic solar cells and polymer solar cells are built from thin film of organic semiconductors including polymers, such as polyphenylene vinylene and small-molecule compounds like copper phthalocyanin and carbon fullerenes and fullerene derivatives. Energy conversion efficiencies achieved to date using conductive polymers are low compared to inorganic materials. In addition, these cells could be beneficial for some applications where mechanical flexibility and disposability are important.

These devices differ from inorganic semiconductor solar cells in that they do not rely on the large built-in electric field of a pn junction to separate the electrons and holes created when photons are absorbed. The active region of an organic device consists of two materials, one which acts as an electron donor and the other as an acceptor. When a photon is converted into an electron hole pair, typically in the donor material, the charges tend to remain bound in the form of an exciton, and are separated when the exciton diffuses to the donor-acceptor interface. The short exciton diffusion lengths of most

polymer systems tend to limit the efficiency of such devices. Nanostructured interfaces, sometimes in the form of bulk heterojunctions[73], can improve performance.

*Silicon Thin Films[85-90]:* Silicon thin-film cells are mainly deposited by chemical vapor from silane gas and hydrogen gas. It has been found that poly-silicon with a low volume fraction of nanocrystalline silicon (nc-Si) is optimal for high open circuit voltage.[91] These types of silicon present dangling and twisted bonds, which results in deep defects as well as deformation of the valence and conduction bands. The solar cells made from these materials tend to have lower energy conversion efficiency than bulk silicon, but are also less expensive to produce. The quantum efficiency of thin film solar cells is also lower due to reduced number of collected charge carriers per incident photon.

An a-Si solar cell is made of amorphous or microcrystalline silicon (μ-Si) and its basic electronic structure is the p-i-n junction. a-Si is attractive as a solar cell material because it is abundant and non-toxic and requires a low processing temperature, enabling production of devices to occur on flexible and low-cost substrates. As the amorphous structure has a higher absorption rate of light than crystalline cells, the complete light spectrum can be absorbed with a very thin layer of photo-electrically active material. A film only 1 micron thick can absorb 90% of the usable solar energy. This reduced material requirement along with current technologies being capable of large-area deposition of a-Si, the scalability of this type of cell is high. However, because it is amorphous, it has high inherent disorder and dangling bonds, making it a bad conductor for charge carriers. These dangling bonds act as recombination centers that severely

reduce the carrier lifetime and pin the Fermi energy level so that doping the material to n- or p- type is not possible. Amorphous Silicon also suffers from the Staebler-Wronski effect, which results in the efficiency of devices utilizing amorphous silicon dropping as the cell is exposed to light. The production of a-Si thin film solar cells uses glass as a substrate and deposits a very thin layer of silicon by PECVD. A-Si manufacturers are working towards lower costs per watt and higher conversion efficiency with continuous research and development on multijunction solar cells for solar panels. a-Si has a higher bandgap (1.7 eV)[92] than crystalline silicon (c-Si) (1.1 eV), which means it absorbs the visible part of the solar spectrum more strongly than the infrared portion of the spectrum. As nc-Si has about the same bandgap as c-Si, the nc-Si and a-Si can advantageously be combined in thin layers, creating a layered cell called a tandem cell. The top cell in a-Si absorbs the visible light and leaves the infrared part of the spectrum for the bottom cell in nc-Si.

Recently, solutions to overcome the limitations of thin-film crystalline silicon have been developed. Light trapping schemes where the weakly absorbed long wavelength light is obliquely coupled into the silicon and traverses the film several times can significantly enhance the absorption of sunlight in the thin silicon films. Minimizing the top contact coverage of the cell surface is another method for reducing optical losses; this approach simply aims at reducing the area that is covered over the cell to allow for maximum light input into the cell. Anti-reflective coatings can also be applied to create destructive interference within the cell. This can be done by modulating the refractive index of the surface coating; if destructive interference is achieved, there will be no

reflective wave and thus all light will be transmitted into the semiconductor cell. Surface texturing is another option, but may be less viable because it also increases the manufacturing price. By applying a texture to the surface of the solar cell, the reflected light can be refracted into striking the surface again, thus reducing the overall light reflected out. Light trapping as another method allows for a decrease in overall thickness of the device; the path length that the light will travel is several times the actual device thickness. This can be achieved by adding a textured back-reflector to the device as well as texturing the surface. If both front and rear surfaces of the device meet this criteria, the light will be 'trapped' by not having an immediate pathway out of the device due to internal reflections. Thermal processing techniques can significantly enhance the crystal quality of the silicon and thereby lead to higher efficiencies of the final solar cells. Further advancement into geometric considerations of building devices can exploit the dimensionality of nanomaterials. Creating large, parallel nanowire arrays enables long absoprtion lengths along the length of the wire while still maintaining short minority carrier diffusion lengths along the radial direction. Adding nanoparticles between the nanowires will allow for conduction through the device. Because of the natural geometry of these arrays, a textured surface will naturally form which allows for even more light to be trapped. A further advantage of this geometry is that these types of devices require about 100 times less material than conventional wafer-based devices.

## 2.4 Organic Photovoltaic Devices

The organic solar cell field started with the small organic molecules (pigments), but real breakthrough was achieved after the development of semiconducting polymers. Incorporating these conjugated polymers into organic solar cells resulted in remarkable improvements within the past years.

The milestone in the polymer solar cell was in 1977. In that year, Shirakawa, MacDiarmid, and Heeger demonstrated the conductivity of conjugated polymers can be controlled by doping who were honored for their discovery with the Nobel prize in chemistry in 2000.[93] Since then, these conjugated polymers have been used successfully in LEDs [94-96] and solar cells.[96, 97]

### 2.4.1 Organic Semiconductor Materials (Conjugated Polymers)

What makes these conjugated polymers attractive for solar cells is the bond structure between the carbon atoms. Different from most of the industrial plastics where the insulating properties of them come from the formation of $\sigma$ bonds between the constituent carbon atoms, in conjugated polymers these bonds that make up the backbone are alternatingly single or double given in figure 2-3a. In other words, each carbon atom in the backbone of the polymer binds to only three adjacent atoms, leaving one electron per carbon atom in a $p_z$ orbital. The mutual overlap between these $p_z$ orbitals results in the formation of $\pi$ bonds along the conjugated backbone, thereby delocalizing the $\pi$ electrons along the entire conjugation path. As the delocalized $\pi$ electrons fill up to whole band, conjugated polymers becomes intrinsic semiconductors [98].

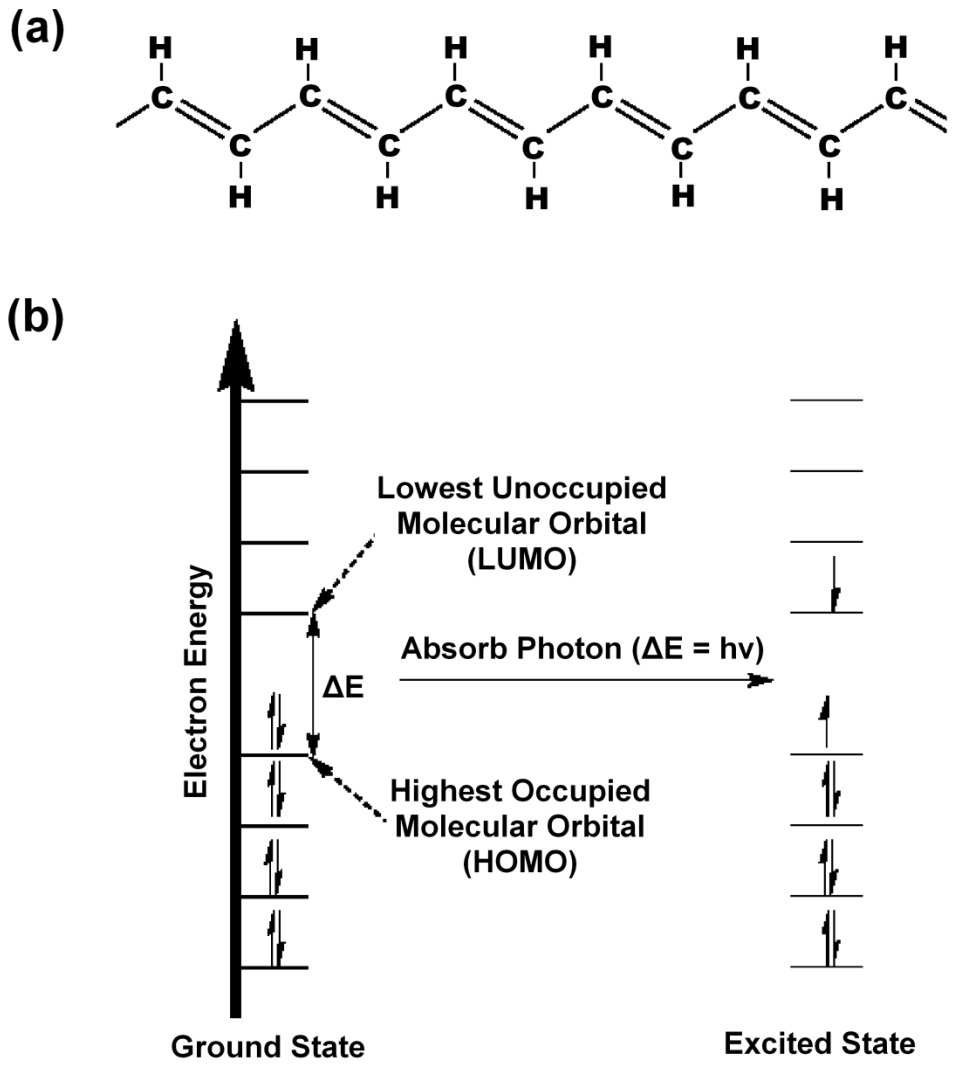


**Figure 2-3** (a) In polyacetylene, the bonds between adjacent carbon atoms are alternatingly single or double (b) Changes in the electron energy levels of a conjugated polymer before and after the photon absorption.

The filled $\pi$ band is called the highest occupied molecular orbital (HOMO) and the empty $\pi^*$ band is called the lowest unoccupied molecular orbital (LUMO). This $\pi$ system can be excited without breaking the chain and therefore chain stays together by the $\sigma$ bonds without falling apart.

In conjugated systems, pi bonds (π bonds) are covalent chemical bonds, where two lobes of one involved electron orbital overlap two lobes of the other involved electron orbital. Only one of the orbital's nodal planes passes through both of the involved nuclei. Also, as the band gap of a conjugated system depends on its size,[98] any disturbance of the conjugation along the polymer's backbone will change the local HOMO and LUMO positions. Therefore, real conjugated polymers are subject to energetic disorder. Hence, it is possible to promote an electron from the HOMO to the LUMO level upon, for example, light absorption. For absorption to occur, the energy of the photon must exactly equal the energy of the orbital gap (band gap). Upon absorption of a photon with sufficient energy by the organic semiconductor, an electron jumps into the LUMO, leaving a hole behind in the HOMO given in figure 2-3b. However, due to electrostatic interactions, this electron-hole pair forms a tightly bound state which is called exciton. The exciton binding energy for organic semiconductors (in a range of 200-to-500 meV) is one order of magnitude larger than inorganic semiconductors like silicon, where photo excitations lead direct free carriers at room temperature.

### 2.4.2 Exciton Dissociation and Charge Transfer Mechanism

After the neutral-charge excitons generated via light absorption, they start to transport through diffusion. The diffusion length of an exciton is a characteristic property of the conjugated polymers and varies from 5 nm to 20 nm. However, the increase in the diffusion length decreases the exciton lifetime meaning that they either decay or dissociate through the internal mechanism. Therefore, the thickness of the conjugated polymer systems is restricted by the exciton diffusion length.

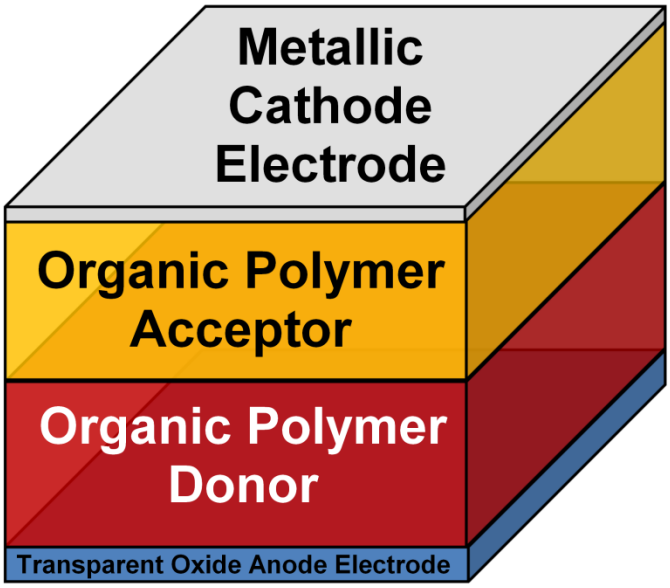


**Figure 2-4** Common conjugated organic polymer photovoltaic device structure

The diffusion mechanism is followed by dissociation for the excitons that are close enough to the layer interface. Conjugated organic polymer photovoltaic devices usually have the device structure given in figure 2-4. As it can be seen from the figure the device has two polymer layers, one is the donor and the other one is the acceptor for the generated charges. After the generation of the excitons, electrons transfer into the acceptor at the donor-acceptor interface while the hole stays. The rest of the excitons decays through recombination. Thus, the energy efficiencies of single-layer polymer devices remain typically below 0.1%. Then, dissociation of the electron-hole pair is transferred into the related electrodes. Efficiency of this process is related to different parameters. Some of which are the exciton diffusion length, carrier drift length and exciton lifetime.

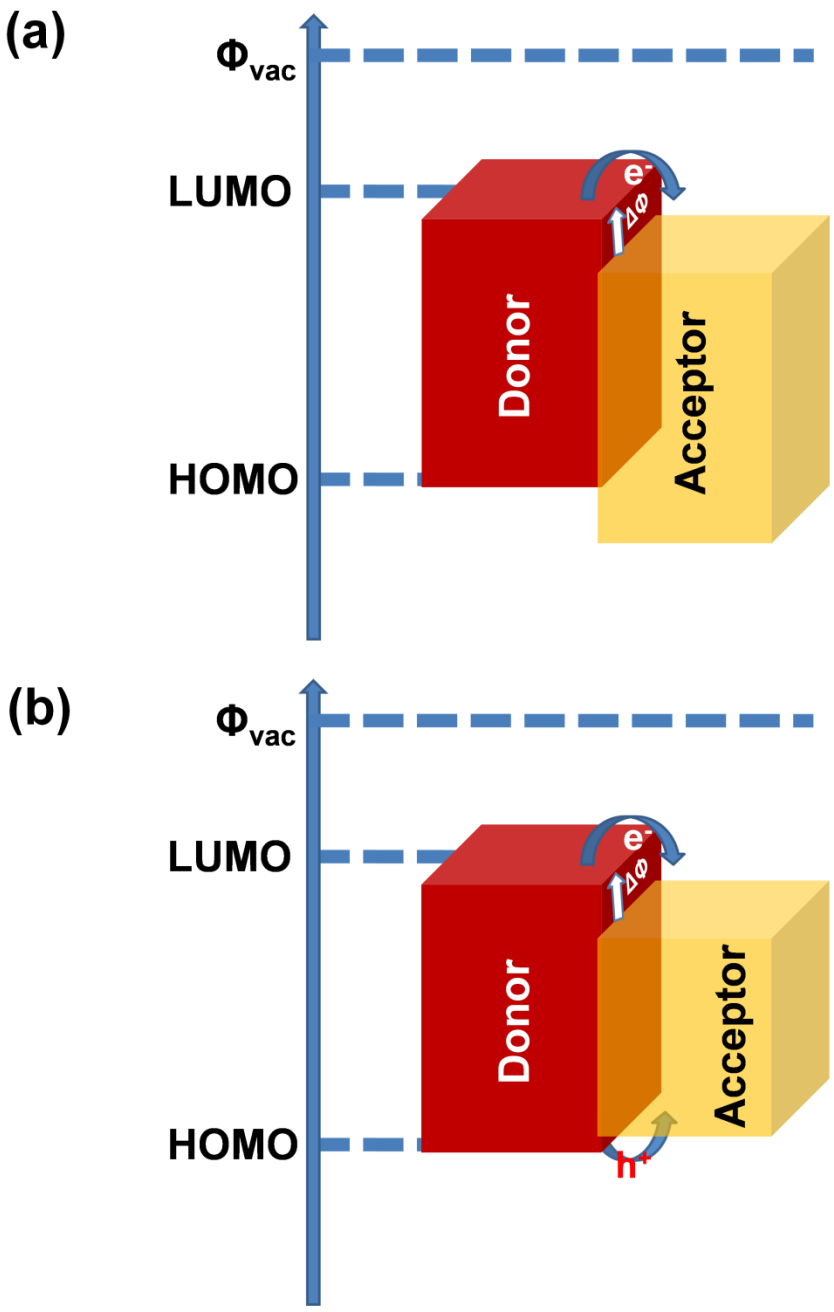


**Figure 2-5** (a) The Interface between two different polymers having lower HOMO and LUMO level but the same band gap. Electrons can be transferred to a lower energy state but holes stay. (b) The interface between two different semiconducting polymers can facilitate either charge transfer by splitting the exciton or energy transfer, where the whole exciton is transferred from the donor to the acceptor.

In addition, the absorption bands of the materials used have a high impact on the overall efficiency. The absorption band of most conjugated polymer lies in a relatively narrow range of solar spectrum, as they are commonly known as intrinsic wide band gap semiconductors (band gap above 1.4eV).

The thermal energy at room temperature (~25 meV) is not sufficient to efficiently generate free charge carriers in organic materials by exciton dissociation, even at typical internal electric fields ($\sim 10^6$–$10^7$ V/m) [95], it is not an easy process. In many conjugated polymers most of the excitons cannot dissociate into free carriers in a pure layer [96].

The charge separation occurs at the interface between donor and acceptor molecules, due to a large potential drop. The excited electron can jump from the LUMO of the donor (the material with the higher LUMO) to the LUMO of the acceptor if the potential difference $\Delta\Phi$ between the ionization potential of the donor and the electron affinity of the acceptor is larger than the exciton binding energy (Figure 2-5a). The efficiency of this exciton dissociation process, also called as photo induced charge transfer, depends on some conditions. First of all, during the process, free charges can be generated only if the hole remains on the donor side of the interface which is due to the higher HOMO level of the donor. If the HOMO of the acceptor is higher, both electron and hole can be transferred to the acceptor side which leads to an energy loss (Figure 2-5b). The thickness of this layer is also an important parameter for efficient exciton generation. This thickness should be higher that the exciton diffusion length to collect all the excitons that are able to diffuse to the interface.

### 2.4.3 Organic Heterojunction Photovoltaic Devices

While high recombination rates and low efficiencies in one layer organic solar cells made them inappropriate candidates for the future applications, the discovery of heterojunction organic solar cells opened a new era for this type of cells. According to this approach, polymer layer is made by hole and electron accepting organic materials and photo generated excitons in this layer dissociated into free carriers at the interface. Comparing with the single component solar cells, recombination rate of heterojunction solar cells is low.

In the literature, different types of heterojunction cells are considered by using different polymer blends and molecules. The list of some breakthrough materials and devices are shown in Table 2-1.

**Table 2-1** Summary of device characteristics for various solar cell devices fabricated with different organic heterojunction polymer blends

| Polymer Blend | Year | Fill Factor [%] | Power Conversion Efficiency [%] | Reference |
|---|---|---|---|---|
| **PPV/ $C_{60}$** | 1995 | - | - | [97] |
| **POPT/CN-PPV** | 1998 | 35 | 1.9 | [99] |
| **MDMO-PPV/ [60]PCBM** | 2001 | 51 | 3.0 | [100, 101] |
| **P3HT/ PCBM** | 2002 | 55 | 4.9 | [101, 102] |
| **PTB7/$PC_{71}$BM** | 2010 | 69 | 7.4 | [103] |

Among the conjugated polymers given above, two of them, (3-hexylthiophene) (P3HT) as the donor polymer and phenyl-$C_{60}$-butyric acid methyl ester (PCBM) as the acceptor polymer (Figure 2-6), drew a lot of attention because of their ability to absorb photons at longer wavelengths and strong electron accepting properties respectively.

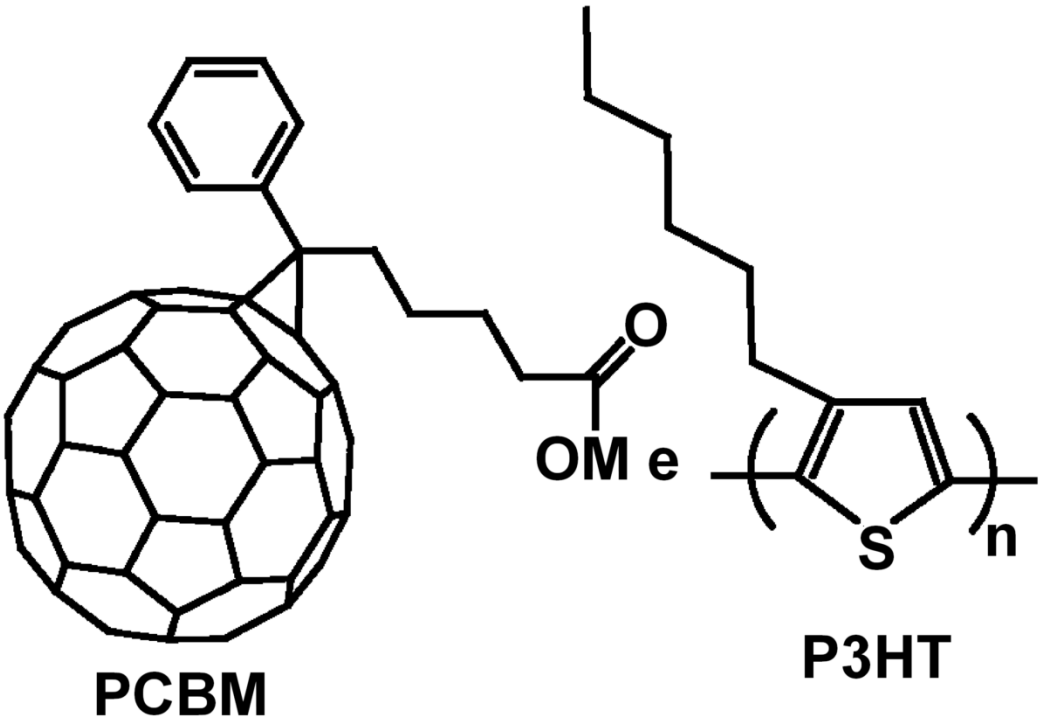


**Figure 2-6** Commonly used acceptor and donor polymers (left) electron acceptor polymer PCBM (right) hole conducting and electron donor polymer P3HT

The buckminster fullerene $C_{60}$ is based on experiments in bulk heterojunction cells that when $C_{60}$ is mixed with hole conducting materials, photoconductivity increases under illumination [104]. But, $C_{60}$ shows a tendency to crystallize in the polymer mixture. This leads to the development of PCBM, a derivative of $C_{60}$ (Figure 2-6left). The increased solubility of PCBM resulted in the formation of smaller crystallites in the blend. For the electron donor material, P3HT (Figure 2-6right) is one of the most widely

used polymer. The most important finding was that slow drying of the P3HT:PCBM layer leads to increase mobility values, thus prevents the buildup of space charge regions inside the device. There are two main types of organic heterojunction solar cells, bi-layer organic heterojunction and organic bulk heterojunction.

#### 2.4.3.1 Bi-Layer Organic Heterojunction Photovoltaic Devices

Bi-layer organic heterojunction, can be prepared by depositing two different layers of organic polymers one top of the other (Figure 2-7a). The geometry of this type guarantees directional photo-induced charge transfer across the interface. After the exciton dissociation, both types of charge carriers travel in different layers. So, the chance for recombination is significantly reduced. The limiting factors on this type of heterojunction cells is the interfacial area is limited to the total device area and thickness of the P3HT layer has to be thin enough to enable excitons to diffuse to the P3HT/PCBM interface for dissociation. Thinner P3HT layer reduces the photon absorption percentage so the device efficiency.

#### 2.4.3.2 Organic Bulk Heterojunction Photovoltaic Devices

A new structure based on the mixture of the electron donor and acceptor material is prepared to increase the interface area and thus to improve exciton dissociation efficiency. This mixture of materials deposited on the surface to form a heterojunction layer which is also called as bulk heterojunction (Figure 2-7b).

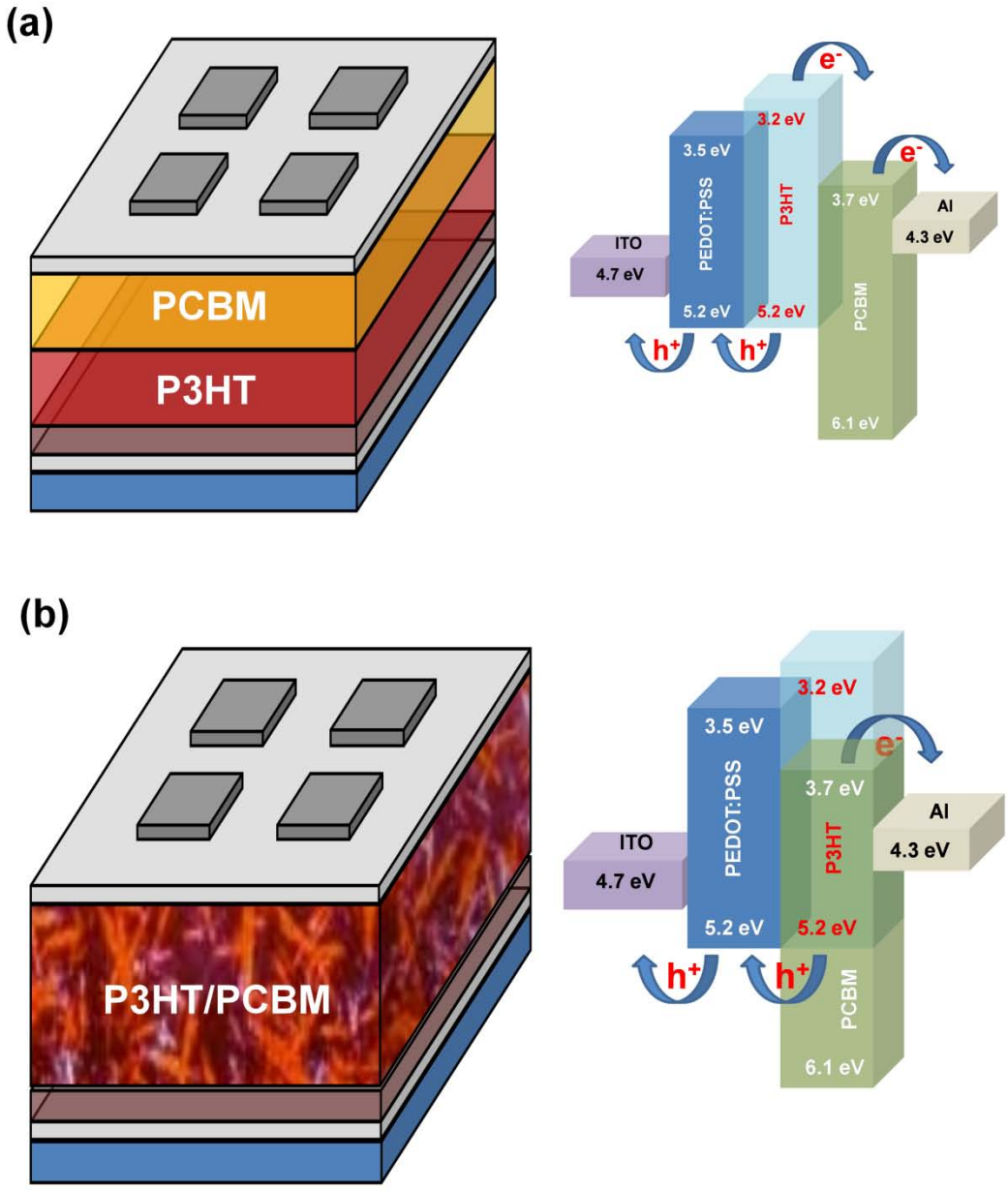


**Figure 2-7** Different organic heterojunction devices structures, corresponding band (a) Bilayer organic heterojunction device structure, (b) Organic bulk heterojunction device structure

One of the early problems in organic bulk heterojunction photovoltaic is the possible short circuits between electrodes based on the fabrication of the thin polymer layer. These short circuits can cause from the gaps in the layers or from the morphology.

This problem is solved by depositing another polymer layer between the anode contact and the active polymer layer. Most common buffer polymer is poly-(3,4-ethylenedioxythiophene):poly-(styrenesulphonic acid) (PEDOT:PSS) given in figure 2-8. Along with acting as an electron blocking layer, a thin semiconductor PEDOT:PSS layer works to prevent electron leakage from the bulk heterojunction acceptor to the anode, to help extracting the photo-generated holes and to planarize the contact surface.

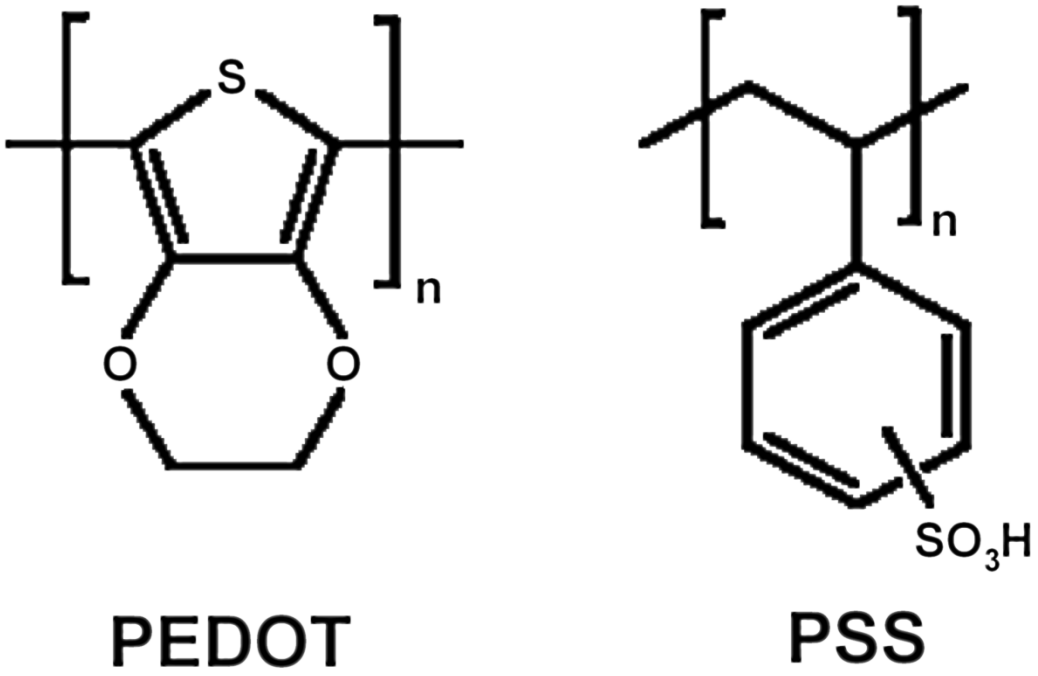


**Figure 2-8** Most commonly used buffer polymers as PEDOT:PSS blend in organic photovoltaic devices (left) PEDOT (right) PSS

Electrode materials have also important effect over the performance of organic solar cells. The work function of the electrode materials determines whether the electrode forms an ohmic or a blocking contact for the respective charge carrier. Moreover the

difference in work function of the electrode materials has a considerable effect over the open circuit voltage. The most commonly used electrode materials for the electron collecting contact is aluminum (Al) (4.28eV). Although some metals are used for the hole collecting side, it is not possible to form an transparent metal electrode with low sheet resistance.

The most commonly used electrode material on the anode side is Indium Tin Oxide (ITO) which is a degenerated semiconductor comprising a mixture of $In_2O_3$ (90%) and $SnO_2$ (10%) with a bandgap of 3.7eV. The large bandgap allows no absorption of wavelengths longer than about 350 nm. The material can be highly conducting leading to very low sheet resistances for 100 nm thick layers of ITO. When there is lack of oxygen, it acts as n- type dopant which is suitable for the anode contact applications. As the thickness of the ITO layer increases, the sheet resistance decreases. Commercial available ITO coated glasses have a sheet resistance between 5-to-15 $\Omega sq^{-1}$ with a thickness of 100-to-150 nm. The transmission properties of the thicker ITO substrates do not change much since the material does not absorb in the visible. Nominal transmission is greater than 85% for the 150 nm thick substrates.

By this property, conjugated polymers with absorption in the whole visible range can be used with ITO if the bandgap of the polymer and the work function of the ITO can allow for the charges to move in the right direction. In this sense, ITO and PEDOT:PSS are suitable for the hole collection side of the organic photovoltaic devices. The energy diagram of an these device is given in figure 2-7a,b for both bi-layer organic photovoltaic device and organic bulk heterojunction photovoltaic devices respectively.

### 2.4.4 Fabrication of Organic Bulk Heterojunction Photovoltaic Devices

Fabrication of organic bulk heterojunction photovoltaic devices starts with the deposition of the transparent conductive oxide layer on top of substrates. Substrates can be glass or flexible plastic (Figure 2-9a). The most commonly used oxide materials for the transparent anode contact are ITO and zinc oxide (ZnO). The optical transmittance and electrical performance of ITO is much better than those of ZnO with a drawback of high cost. The deposition of the oxide layer can be done by sputtering (Figure 2-9b). ITO can have a 15 Ω/sq sheet resistance when the optical transmittance is close to 99% so ITO is the most popular material for transparent oxide contacts not only in the photovoltaics area but also in liquid crystal displays (LCD) and etc. ITO deposited on top of glass substrates shows hydrophobic property which makes it harder for the liquid based organic polymers to attach on surface. In order to overcome this problem, ITO coated glass substrates are usually treated by oxygen ($O_2$) plasma etching for 5 min at most. This process changes the surface properties of the substrates from hydrophobic to hydrophilic.[105] Following the plasma etching a thin layer of buffer layer which is mostly PEDOT:PSS for organic bulk heterojunction photovoltaic devices is deposited on top of ITO layer (Figure 2-9c). The deposition of PEDOT:PSS starts with first solving the PEDOT:PSS in organic solvents such as methylpyrrolidone, dimethyl sulfoxide or sorbitol which increase the electrical conductivity of PEDOT:PSS layer many orders of magnitude. Then, PEDOT:PSS solution is spin coated on to the surface with 4000 rounds per minute (rpm) for less than 1 min to make the layer both conductive and thin enough for high optical transmittance.

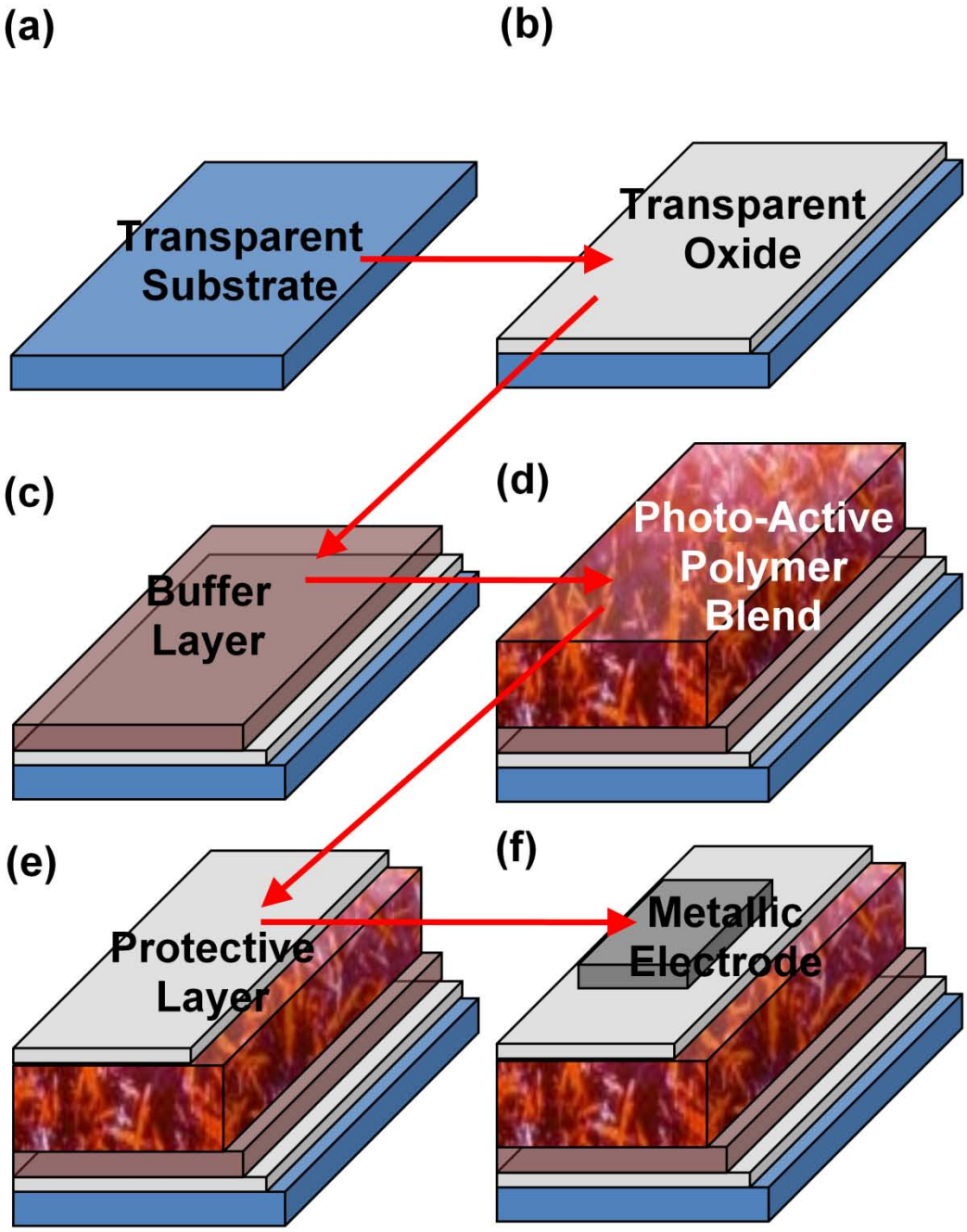


**Figure 2-9** Fabrication steps for organic bulk heterojunction photovoltaic devices. (a) substrate, (b) deposition of transparent and electrically conductive oxide layer, (c) deposition of buffer layer, (d) deposition of donor and acceptor polymer blend, (e) deposition of protective layer, (f) deposition of metal cathode electrode.

The aqueous PEDOT:PSS is then annealed at 120-to-150 °C for 15 minutes in usually inert gas environment such as nitrogen ($N_2$) to make the layer hard enough to for deposition of the active donor and acceptor polymer blend. The benefits of this annealing on the surface properties have been previously shown.[106]. The donor, P3HT, and acceptor, PCBM, are prepared as a mixture of 1:1 P3HT and PCBM blend which had been dissolved in 1 ml 1,2-dichlorobenzene (ODCB) to make a 60 mg/ml solution, and stirred for 12 hours at 80 °C was filtered through a 0.22 μm filter and then deposited on top of the PEDOT:PSS layer at different speeds for 50-to-100 seconds depending on the layer thickness by spin coating (Figure 2-9d). High temperature annealing treatment was carried in $N_2$ environment for 1 hour at 80-to-120 °C. The sample was then cooled back to room temperature within a 30 minute ramp. Slow annealing and cooling makes the crystal structure of the organic polymer blend more ordered which helps to increase the efficiency of the charge transfer, exciton dissociation and reduce the number of dead ends in the for the charges. For the cathode contact, first 1 nm of protective layer which is usually lithium fluoride (LiF) is deposited on top of active polymer blend via vacuum thermal evaporation to protect the organic polymer from the energetic metal atoms during thermal evaporation.[107] This protection layer also improves the overall performance by lowering the work function of the metal electrode. Then, 60-to-100 nm thick metal layer is deposited on top of LiF layer as the cathode contact again via vacuum thermal evaporation. Most commonly used metallic contact material for organic bulk heterojunction photovoltaic devices is Al because of its high electrical conductivity and low price.

### 2.4.5 Characterization of Organic Bulk Heterojunction Photovoltaic Devices

#### 2.4.5.1 Optical (Spectral) Characterization

*Absorbance / Transmittance:* Since the photovoltaic means converting the energy of light to electricity, the first step for this conversion is absorbing the energy of light. Light is electromagnetic radiation of any wavelength. Generally, this electromagnetic radiation is classified by wavelength. Light exhibits properties of both waves and particles and these particles are called photons. A photon has energy proportional to its frequency, i.e. reciprocal of wavelength. Light is emitted and absorbed in photons so in order to absorb the energy of light photons have to be absorbed in a process that their energy can be converted in to electricity. This process is known as photoelectric effect and explained in part 2.2.

Absorbance is the logarithmic measure of light that shows the amount of absorbed photons out of all incident photons for a given wavelength. This parameter can be defined over a range of wavelengths known also as spectra. When the definition of absorbance is done over a spectra this gives the absorbance spectra of a semiconductor material. Absorbance is defined as;

$$A_\lambda = \log_{10}\left(\frac{I_0}{I}\right) \tag{2.1}$$

where I is the intensity of light for a given wavelength, $\lambda$, passed through the material and $I_0$ is the intensity of incident light.

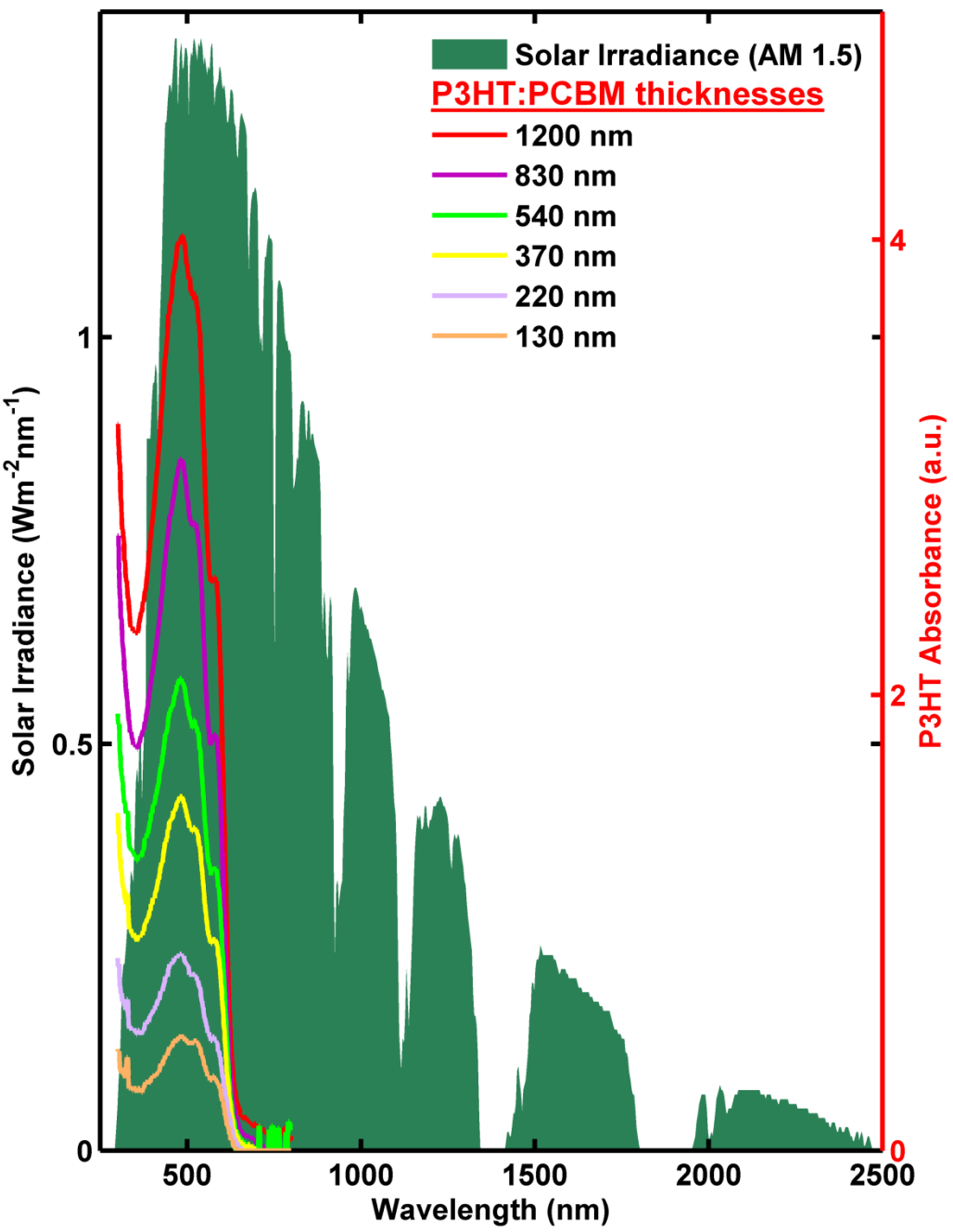


**Figure 2-10** Absorbance spectra of P3HT:PCBM photo-active bulk heterojunction layers having different thicknesses versus the solar irradiance spectra.

In order to use the light source more efficiently the peak absorbance should be in the range of high power irradiance spectra. Most of the organic photovoltaic devices are solar cells so the absorbance peaks of organic polymer blends used in bulk heterojunction structure should follow the solar irradiance spectra. In figure 2-10, absorbance spectra for P3HT:PCBM bulk heterojunction photo-active organic polymer layers and solar irradiance spectra are given. As it can be seen from the figure, the peak absorbance of P3HT:PCBM is in the range of the highest solar irradiance.

Additionally, in the device structure, magnitude of absorbance depends on the thickness of the active layer. Because the thickness of the active layer is of the same order of magnitude as the wavelength of the incident light, small changes in this layer thickness can have a significant effect on the absorbance of the devices. As it can be seen in figure 2-10, as the thickness of the P3HT:PCBM layer increases, magnitude of absorbance increases. This means more photons are absorbed and turned into exitons. However, there is a trade-off between the device thickness, absorbed number of photons and the recombination rate of excitons. Because organic polymers have very short exciton diffusion lengths and low charge carrier mobility values.

Transmittance is the fraction of incident light at a specific wavelength that passes through the material. It is also known as the reciprocal of the absorbance and can be defined as;

$$T_{\lambda} = 10^{-A_{\lambda}} \tag{2.2}$$

*Spectral Responsivity:* Spectral responsivity measurements of organic bulk heterojunction photovoltaic devices are used to calculate the spectral mismatch correction factor and understand physical mechanisms of devices. This correction factor between the reference and test cells is used to set the light intensity of the solar simulator for solar performance measurements. The spectral responsivity, $S_\lambda$, is calculated by

$$S_\lambda = \frac{q\lambda}{hc} QE_\lambda \tag{2.3}$$

where the constant term q/hc equals 8.0655 × 105 for w in units of meters, $S_\lambda$ in units of A/W and the quantum efficiency, $QE_\lambda$ in units of %.

The quantum efficiency is the ratio of the number of carriers collected by the solar cell to the number of photons of a given energy incident on the solar cell. The quantum efficiency may be given either as a function of wavelength or as energy. If all photons of a certain wavelength are absorbed and the resulting minority carriers are collected, then the quantum efficiency at that particular wavelength is unity. The quantum efficiency for photons with energy below the band gap is zero. A quantum efficiency curve for an ideal solar cell is shown in figure 2-11. While quantum efficiency ideally has the rectangular shape shown above, the quantum efficiency for most solar cells is reduced due to recombination effects. The same mechanisms which affect the collection probability also affect the quantum efficiency. The quantum efficiency can be viewed as the collection probability due the generation profile of a single wavelength, integrated over the device thickness and normalized to the incident number of photons.

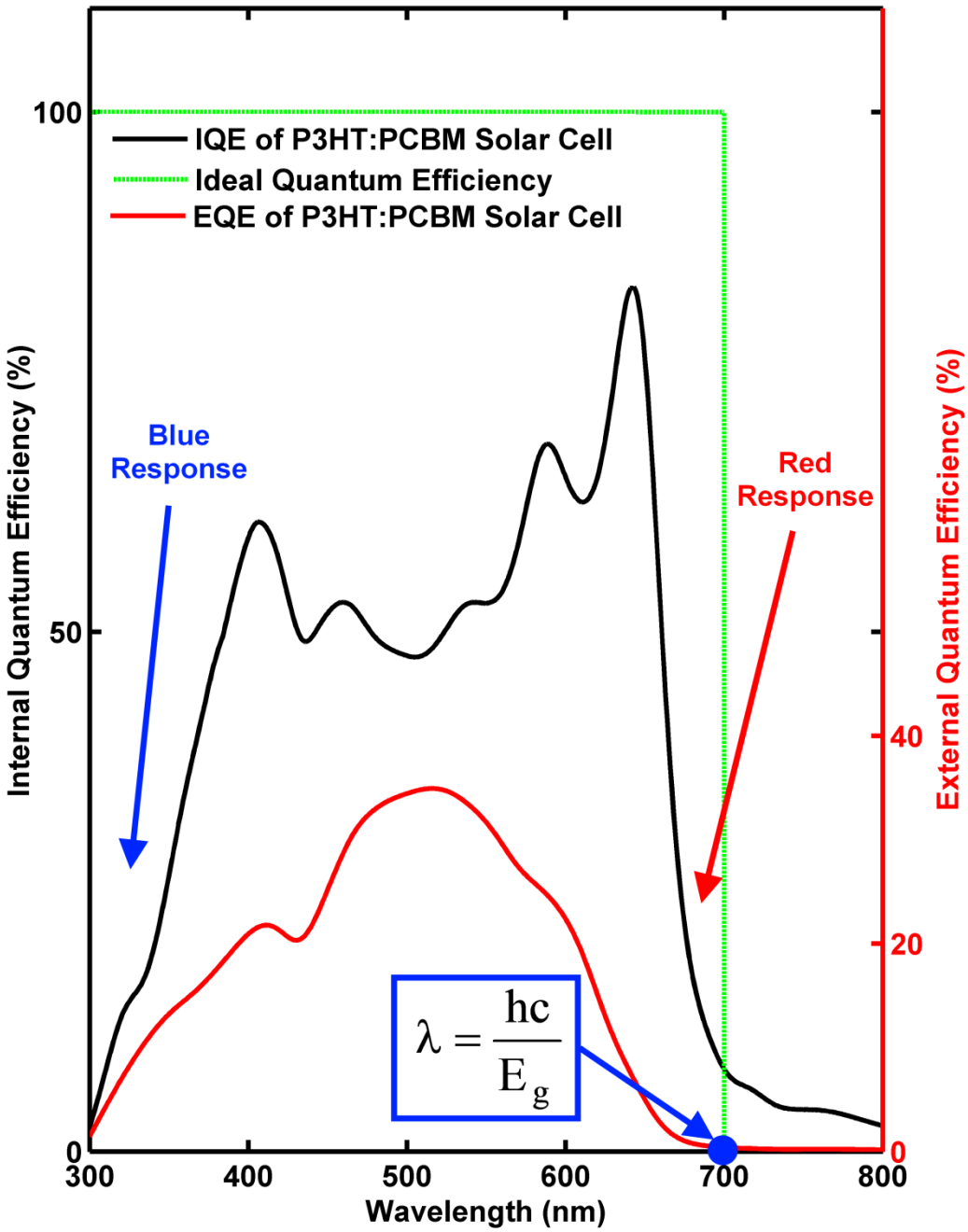


**Figure 2-11** External and internal quantum efficiency spectra for a P3HT:PCBM organic bulk heterojunction photovoltaic device given in comparison with the ideal quantum efficiency.

There are two types of quantum efficiency definitions. The first one is the external quantum efficiency (EQE) which describes the overall efficiency of the working mechanism of the organic bulk heterojunction photovoltaic devices. EQE can be determined by the ratio of the photons that generate electrons in the external circuit to incident photons of monochromatic light per time and area and given as;

$$EQE = \frac{\text{Number extracted electrons}\,(N_e)}{\text{Number of incident photons}\,(N_p)} \tag{2.4}$$

The EQE therefore depends on both the absorption of light and the collection of charges. EQE of a P3HT:PCBM organic bulk heterojunction photovoltaic device is given in figure 2-11. One important parameter during the measurements of the spectral response of the organic bulk heterojunction photovoltaic devices is the response time of the cell to the chopped light. For polymer solar cells, the response of the device to the incident light is very fast. For a P3HT:PCBM device, the response time is less than a millisecond [108].

Second type of quantum efficiency is the internal quantum efficiency (IQE). The IQE is the ratio of the number of charge carriers collected by the solar cell to the number of photons of a given energy that shine on the solar cell from outside and are not reflected back by the cell, nor penetrate through, i.e. absorbed photons. By measuring the reflection and transmission of a device, the EQE curve can be corrected to obtain the IQE. If the optical losses in a solar cell are known, the IQE can be calculated as;

$$IQE = \frac{\text{Number extracted electrons}\,(N_e)}{\text{Number of absorbed photons}\,(N_p)} \tag{2.5}$$

The IQE only considers photons, which are absorbed in the active layer. It is therefore the ratio of electrons in the external circuit to the number of photons absorbed in the active layer. IQE of a P3HT:PCBM organic bulk heterojunction photovoltaic device is given in figure 2-11. IQE and EQE give insight into both the charge carrier generation and transport processes in a photovoltaic device.

### 2.4.5.2 Electrical Characterization

*Equivalent Circuit Model:* Before we start the discussion of the electrical properties of organic solar cells, it is important to understand the electrical model of a solar cell. In the ideal case, a solar cell can be modeled by a diode parallel with a current source. But in practice, a series and a shunt resistance should be added to the model such that; the shunt resistor $R_{SH}$ is due to recombination of charge carriers near the dissociation site and the series resistor $R_S$ considers mobility of the specific charge carrier in the respective transport medium (Figure 2-12). In the ideal case, $R_S = 0$ (short circuit) and $R_{SH} = \infty$ (open circuit). The illuminated current density equation is given by,

$$J = J_0\left[\exp\left[\frac{q(V - JAR_S)}{nK_BT}\right] - 1\right] + \frac{V - JAR_S}{AR_{SH}} - J_L \qquad (2.6)$$

where $J_0$ is the reverse saturation density, q is the elementary charge, A is the active area of the device, n is the ideality factor, $K_B$ is the Boltzmann constant, T the temperature of the device and V the externally applied bias voltage. Here, $J_L$ is the photogenerated current density.

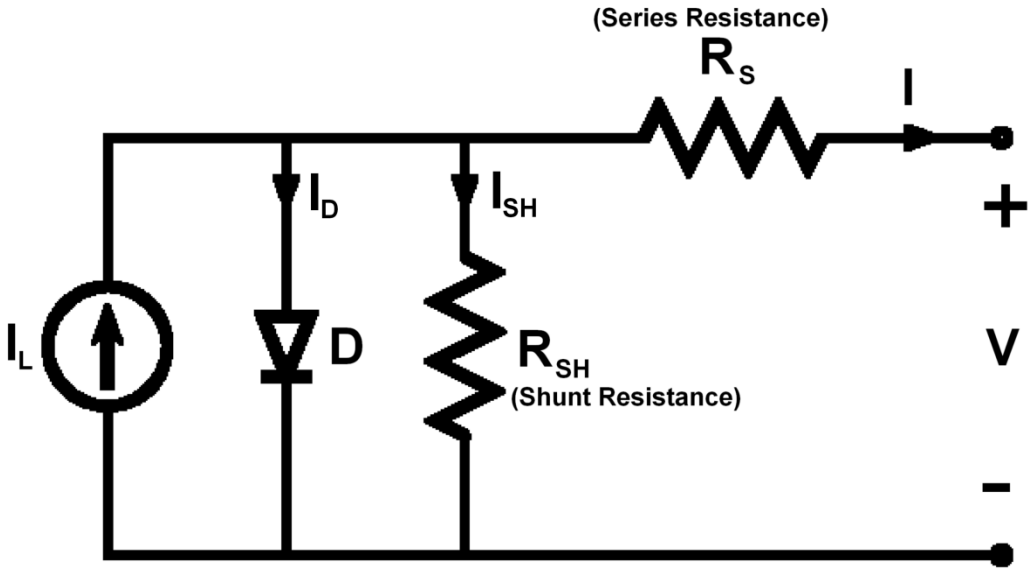


**Figure 2-12** Equivalent circuit model of a organic bulk heterojunction photovoltaic device, where $I_L$ is the photogenerated current.

*J-V curve and Photovoltaic Device Performance Parameters:* The main performance evaluation of a solar cell is described from its power conversion efficiency (PCE). PCE of a photovoltaic device is determined from the current density (J, current per unit device area) – voltage (V) characteristics of the cell. The J-V characteristics of an organic bulk heterojunction photovoltaic device in the dark and under illumination are shown in figure 2-13.

While, the J-V curve shows a diode like behavior in the dark; under illumination, extra charge carriers are generated in the device and the dark J-V curve is shifted in the negative J. Under illumination, three key figures are determined from the J-V curve; open circuit voltage ($V_{OC}$), short circuit current density ($J_{SC}$) and maximum power point ($P_{max}$).

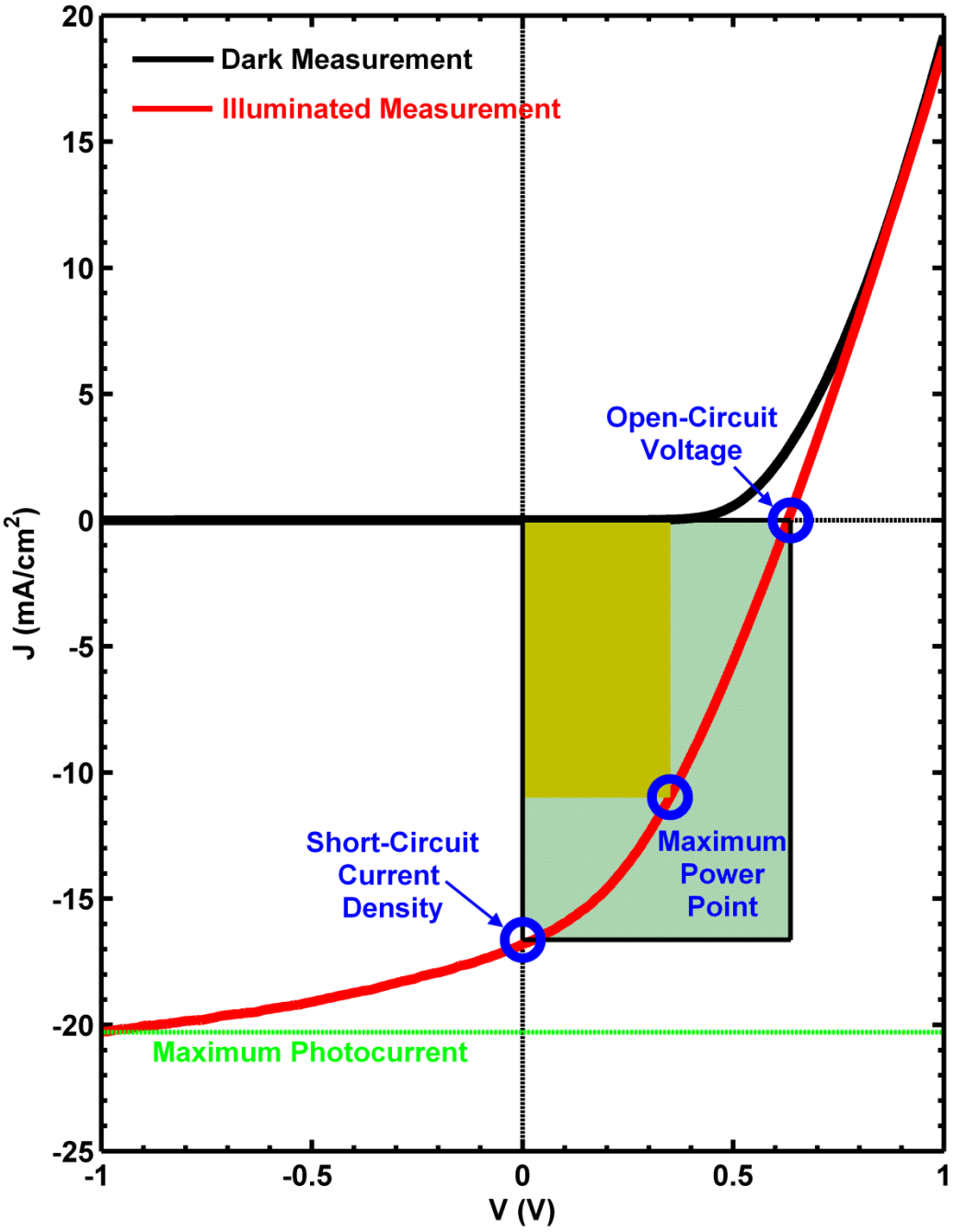


**Figure 2-13** J-V characteristics of an organic bulk heterojunction photovoltaic devices measured in dark and under 1 sun (AM 1.5 – 1mWmm$^{-2}$) illumination.

In organic bulk heterojunction photovoltaic devices, the $V_{OC}$ is found to be linearly dependent on the HOMO level of the donor (D) and LUMO level of the acceptor (A).[109-111] However, this relation is only valid when the electrodes form ohmic contacts with the HOMO of the donor and the LUMO of the acceptor. This relationship can be described by the following equation;

$$V_{OC} = \mathrm{HOMO(D)} - \mathrm{LUMO(A)} - \frac{K_B T}{q} \ln\left[\frac{(1-p)\gamma N_C^2}{pG_M}\right] \tag{2.7}$$

in which q is the elementary charge, p is the dissociation probability of a bound electron–hole pair into free charge carriers, $G_M$ is the generation rate of the bound electron-hole pairs, $\gamma$ is the Langevin recombination constant, $N_C$ is the effective density of states, $K_B$ is the Boltzmann constant, and T is the temperature.

In the organic bulk heterojunction organic photovoltaic device architecture, $V_{OC}$ is dependent on various structural parameters. If the charge carrier losses increase, $V_{OC}$ decreases. Moreover, open circuit voltage depends on the nanomorphology of the organic polymers in the bulk heterojunction active layer. It is also important to have a better match between the work function of the metal electrode and the HOMO level of the organic polymer semiconductor to avoid formation of Schottky barriers which reduce the charge carrier diffusion to metal electrode by generating an electric field on the interface. This match is modified by depositing a thin layer of LiF between the electrode and the organic polymer. This deposition decreases the interfacial effects on the interface.

In the ideal case, photogenerated current of the organic polymer layer in an organic bulk heterojunction photovoltaic device can be described by;

$$I_L = nq\mu E \tag{2.8}$$

where n is the charge carrier density, q is the elementary charge, μ is the charge carrier mobility, and E is the electric field. When the overall photovoltaic device structure is considered, this current is reduced by several factors. As an outcome, overall short circuit current of an organic bulk heterojunction photovoltaic device is described by;

$$I_{SC} = I_L - I_{SH} - I_D \tag{2.9}$$

where $I_{SH}$ is the shunt resistor current and  current and $I_D$ is the diode current as given in figure 2-12. $I_{SC}$ is the current I when the voltage source V is short-circuited.

The point where the electrical power generated by the photovoltaic device reaches the maximum value represents the condition where the device can deliver its maximum power to an external load. It is called the $P_{max}$ as given in figure 2-13. The ratio of this $P_{max}$ to the product of the $J_{SC}$ and the $V_{OC}$, i.e. theoretical maximum power can be generated by the device if the device is ideal, is called the fill factor (FF).[112]

$$FF = \frac{P_{max}}{V_{OC} J_{SC}} \tag{2.10}$$

Ideally, the fill factor should be unity, but losses due to transport and recombination result in values between 0.2–0.7 for organic bulk heterojunction photovoltaic devices. Fill factor of a photovoltaic device is mainly determined by charge

dissociation, the charge carrier transport, and the recombination processes. These processes effects the hole transport capability. When hole and electron transport are unbalanced, a build up space charge region results in the active layer, resulting in low fill factors.

The photovoltaic power conversion efficiency (η) [113] is then calculated for an incident light power of light by;

$$\eta = \frac{P_{out}}{P_{in}} = \frac{V_{OC} J_{SC}}{P_{in}} FF \tag{2.11}$$

where $P_{in}$ is the incident light power per unit area. This light intensity is standardized at 1000 W/m$^2$ with a spectral intensity distribution matching that of the sun on the earth's surface at an incident angle of 48.2°, which is called the AM 1.5 spectrum [114]. The spectra of solar irradiation for AM 0 and A.M 1.5 which are also known as the extraterrestrial and terrestrial irradiations are given in figure 2-14 in comparison with the black body radiation. A black body is an idealized physical body that absorbs all incident electromagnetic radiation. Because of this perfect absorptivity at all wavelengths, a black body is also the best possible emitter of thermal radiation, which it radiates incandescently in a characteristic, continuous spectrum that depends on the body's temperature. At Earth-ambient temperatures this emission is in the infrared region of the electromagnetic spectrum and is not visible. The object appears black, since it does not reflect or emit any visible light. Blackbody radiation becomes a visible glow of light if the temperature of the object is high enough.

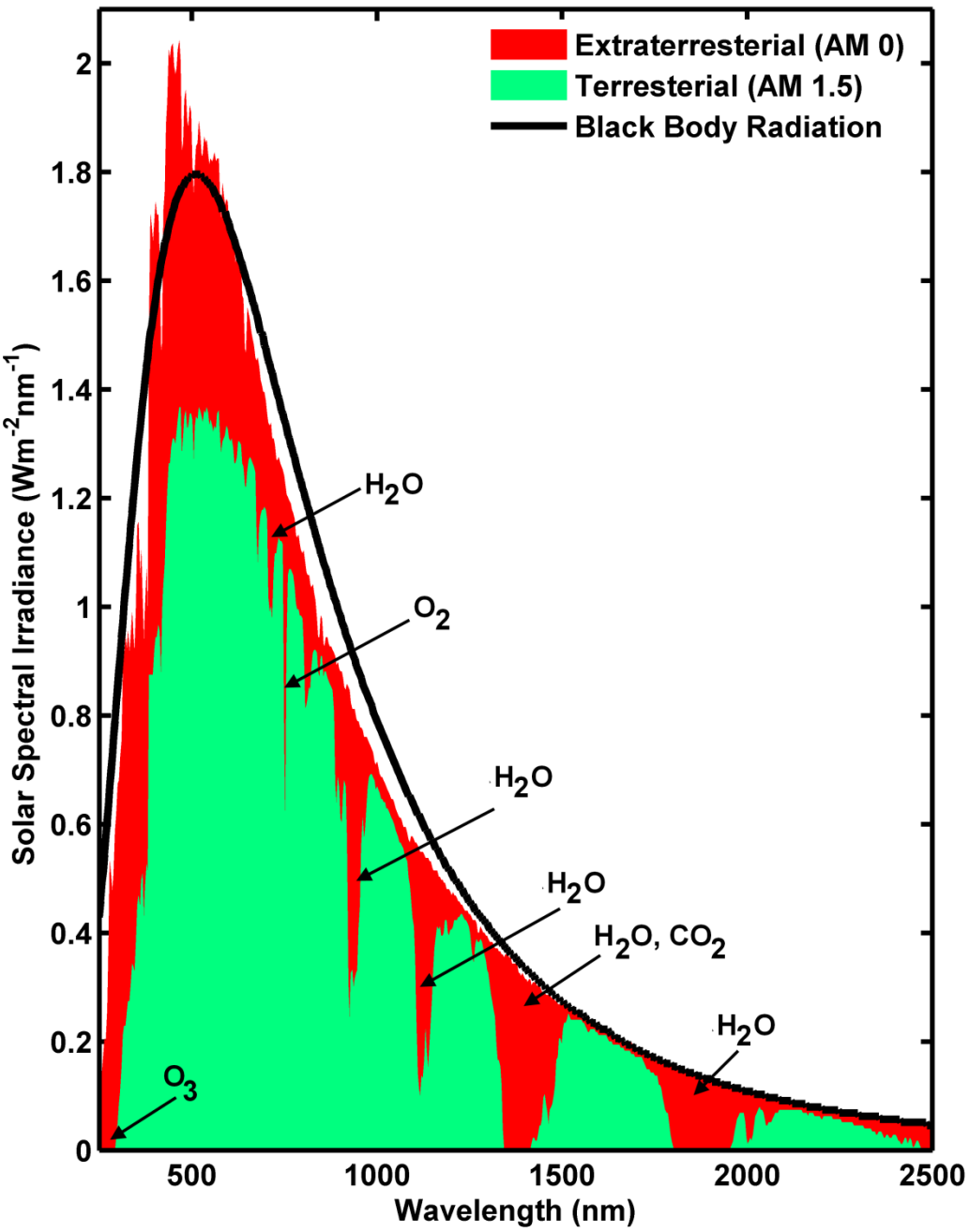


**Figure 2-14** Solar spectral irradiance at sea level, terrestrial or AM 1.5, above earth's atmosphere, extraterrestrial or AM 0, and black body radiation.

One other important performance parameter of organic bulk heterojunction photovoltaic devices that can be extracted from the J-V characteristic of the device is the series resistance, $R_S$, of the device by;[115]

$$R_S = \frac{V_{max\,P}}{I_{max\,P}} - \frac{nK_BT}{q(I_L - I_{max\,P})} \tag{2.12}$$

where $V_{maxP}$ and $I_{maxP}$ are the voltage and current at $P_{max}$ point, n is the diode ideality factor, $K_B$ is the Boltzmann constant, T is the temperature, q is the elementary charge and $I_L$ is the photogenerated current.

## Chapter 3:

## Effect of Incident Light Power on Schottky Barriers and I–V Characteristics of Organic Bulk Heterojunction Photodiodes

### 3.1 Introduction

In recent years, photodiodes fabricated from organic semiconductors have drawn great attention due to the cost effective, flexible, thin and large area device fabrication opportunities.[116, 117] In addition to these desirable properties, their high on/off ratios and high external quantum efficiencies have taken organic photodiodes (OPDs) to a competing level with their inorganic counterparts.[118, 119] These unique electro-optical characteristics make them candidates for various optical/electrical applications, such as; optochemical sensors,[120] image sensor arrays[121] or optocouplers.[122] Despite of this high application potential, there are few works reported in literature about analyzing and explaining the device principles of the OPDs.[123] In most of these reports, photodiodes are characterized by using the non-ideal diode model.[124, 125] The drawback of this model is assuming some parameters, such as; photo-generated current and recombination to be constant or to have a linear effect on the device performance.[126]

The most commonly used structure for the bulk heterojunction (BH) OPDs is the indium tin oxide (ITO)/poly(ethylene-dioxythiophene):poly(styrenesulphonate) (PEDOT:PSS)/poly(3-hexylthiophene):phenyl-$C_{61}$-butyric acid methyl ester (P3HT:PCBM)/ Aluminum(Al)[105] given in figure 3-1. During the fabrication process,

P3HT:PCBM layer exposes to oxygen and moisture because of remaining water molecules at the interfaces. As previous studies show that P3HT can easily be p-type doped under these circumstances[127] and doping concentration is directly related to the oxygen concentration in P3HT.[128, 129] The doping makes it possible to form Schottky barriers (SBs) at the metal contacts of the devices (Figure 3-1). These barriers can be detected by Mott-Schottky characteristics.[130] The space charge regions (SCRs) on SBs forming only in the semiconductor side so these barriers behave as single junction Schottky diodes.[130]

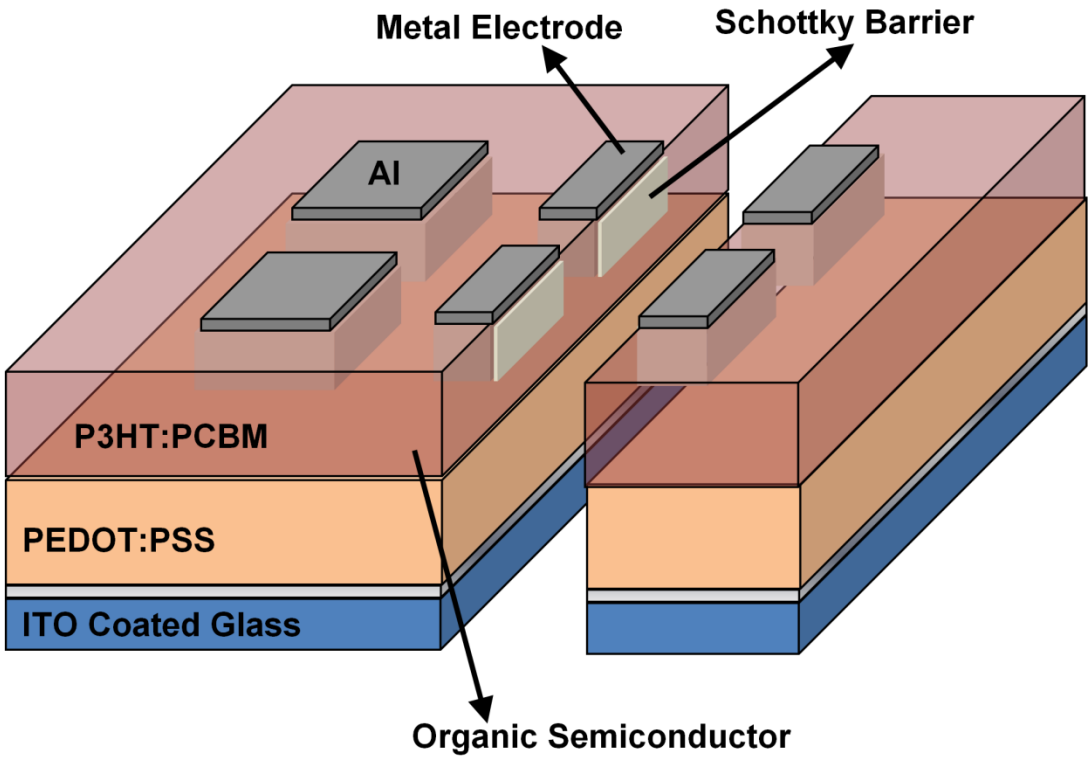


**Figure 3-1** Structure of BH OPDs: Glass Substrate / ITO / PEDOT:PSS / P3HT:PCBM / Al electrodes. SBs form under Al electrodes on metal-organic semiconductor interface.

Here we studied the effect of incident light power (ILP) on the SCRs of the SBs, the current-voltage (I-V) characteristics and performance of the devices and built an I-V model for the devices that involves these effects.

### 3.2 Experimental

For the fabrication of OPDs, ITO coated glass substrates from Delta Technologies (15 Ω/sq) were used as the transparent anode contact. The glass substrates were cleaned by ultrasonification in subsequent solutions such as; detergent, de-ionized (di) water for rinsing, acetone and isopropanol alcohol (IPA). After the cleaning process, the cleaned ITO coated glass substrates were left for annealing for 12 hours in nitrogen ($N_2$) at 70 °C. This process was followed by oxygen ($O_2$) plasma etching for 5 minutes to change the surface properties of the substrates from hydrophobic to hydrophilic.[105] Following the plasma etching, a thin layer of PEDOT:PSS was spin-coated from aqueous solution at 4000 rpm for 40 seconds, after passing through 0.45 μm syringe filter. The substrate was then annealed at 150 °C for 15 minutes in $N_2$. The benefits of this annealing on the surface properties have been previously shown.[106] After the deposition of the PEDOT:PSS layer, the substrates were transferred into a $N_2$ filled glove-box system. A mixture of 1:1 P3HT and PCBM blend which had been dissolved in 1 ml 1,2-dichlorobenzene (ODCB) to make a 60 mg/ml solution, and stirred for 12 hours at 80 °C was filtered through a 0.22 μm filter and then deposited on top of the PEDOT:PSS layer at 400 rpm, 500 rpm and 600 rpm separately on different samples for 50 seconds by spin coating. High temperature annealing treatment was carried in $N_2$ environment for 1 hour

at 120 °C. For the cathode contact, 100 nm thick Al layer was deposited on top of P3HT:PCBM layer via vacuum thermal evaporation (Temescal BJD 1800).

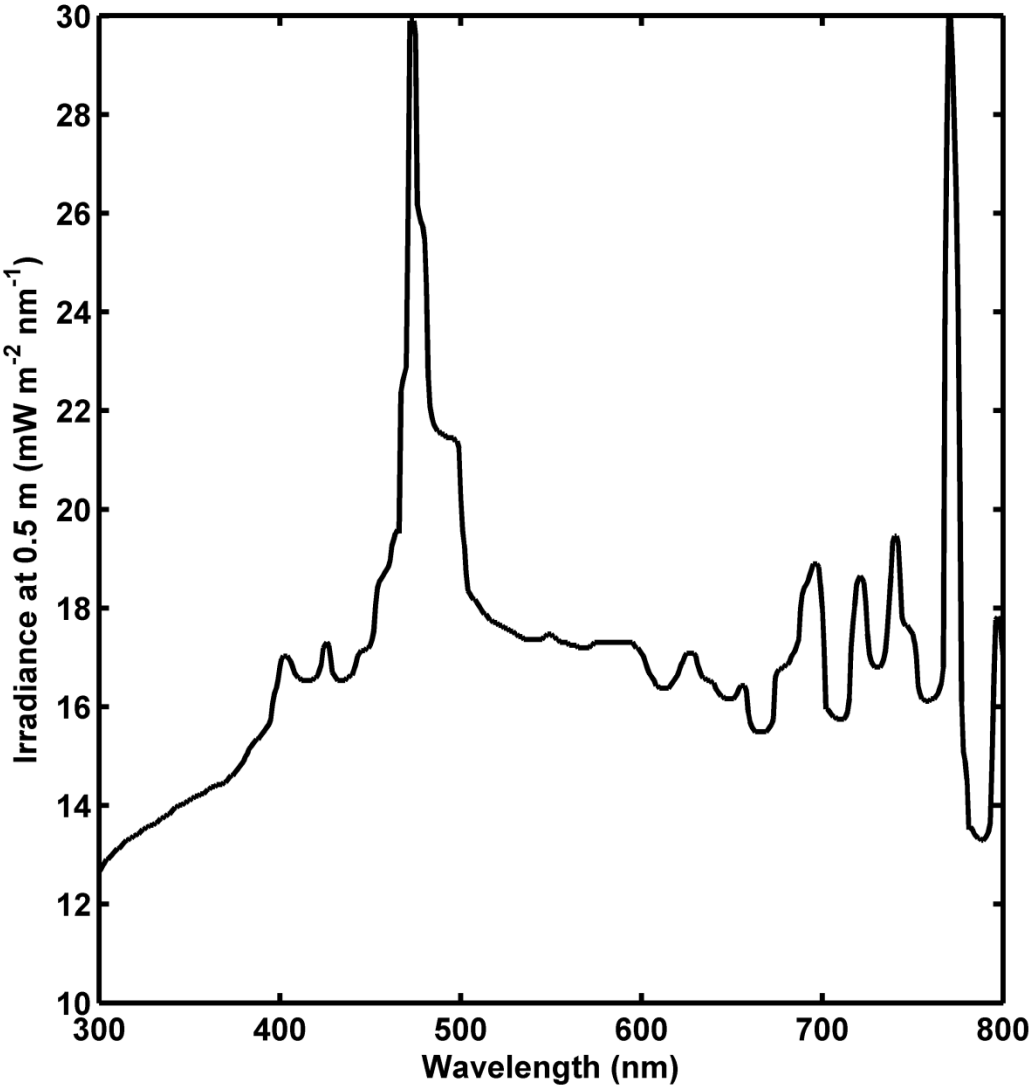


**Figure 3-2** Power irradiance spectra of the Newport 96000 Solar Simulator at 0.5 m distance.

I-V characterization measurements were performed on each device by using Newport 96000, UV-Enhanced 150 W Xenon Solar Simulator at a distance of 50 cm from the light source by changing the ILP from 0 $mW/mm^2$ to 1.34 $mW/mm^2$. The I-V characteristics were acquired via measurement under different ILPs by using a probe station and Agilent 4155C Semiconductor Parameter Analyzer.

For OPD responsivity characterization, the photocurrent values under 0 bias voltage, short-circuit currents under illumination, were measured by using the solar simulator which set to a power of AM 1.5 G, 1 sun (1 $mW/mm^2$), for 10 different wavelength values changing from 350 nm to 850 nm. Different wavelengths of light were acquired by using a rotatable filter cage system which has 10 different optical band-pass filters (Thorlabs) installed in. The power irradiance of the light source for the sample distance was measured by using a reference photodiode (Thorlabs) (Figure 3-2).

For Mott-Schottky characterization, the capacitance-voltage (C-V) measurements were performed for each device by using Agilent 4284A LCR meter at 98 Hz.

### 3.3 Results and Discussion

In order to investigate the effect of change in SCR width on the I-V characteristics of the OPDs, first, the ILP was fixed to 1 $mW/mm^2$. The approximate I-V characteristic of SBs[131] with slight modifications for reverse bias and generated photocurrent, given in equation 3.1, is usually used to model reverse biased BH OPDs. This model assumes that there is no change in the SCR width of the SBs at metal-semiconductor interfaces.

$$I = -I_S\left\{exp\left[\frac{-qV_R}{nK_BT}\right]-1\right\}+I_{ph} \tag{3.1}$$

In equation 3.1, $I_S$ = 1.2 mA, the reverse saturation current, is extracted from dark measurement (Figure 3-3), $V_R$ is the applied reverse bias, $n$ = 40, the ideality factor, and $I_{ph}$ = 1.25 mA, the photocurrent, are extracted from the measurement data in figure 3-4, $K_B$ is the Boltzmann constant, $T$ = 300 K is the temperature and $q$ is the electronic charge. In figure 3-4, there is a significant difference between the measurement data and the results from equation 3.1 model. The reason for this is; the effect of change in SCR thickness was not included in the calculations.

This effect can be included to the I-V model in equation 3.1 by adding the reverse generation current, on Schottky SCR which is given by[132]

$$I_g = A\frac{qn_i}{\tau_e}W \tag{3.2}$$

where, $A$ = 16 mm$^2$ is the area of the aluminum contact, $n_i$ = 1.9 $\times 10^{11}$ cm$^{-3}$, intrinsic doping concentration of P3HT:PCBM, is extracted from the slope of the dark current, $W$ is the width of the SCR and $\tau_e$, the relaxation time of electrons, is assumed as $10^{-10}$ s.[133] Accordingly, the new I-V model is then given by equation 3.3.

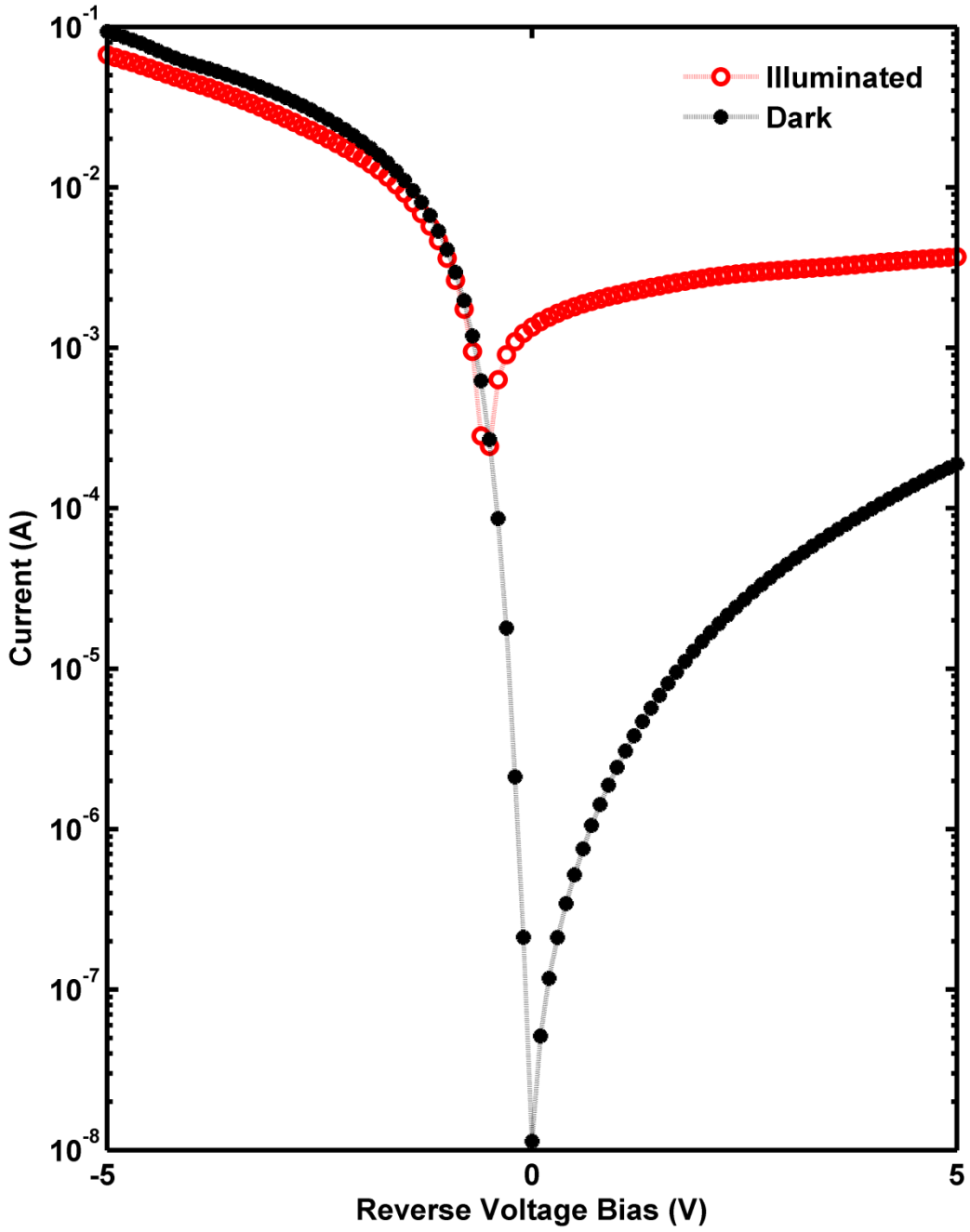


**Figure 3-3** Dark and 1 sun illuminated $\log_{10}$(I)-V characteristics of OPD

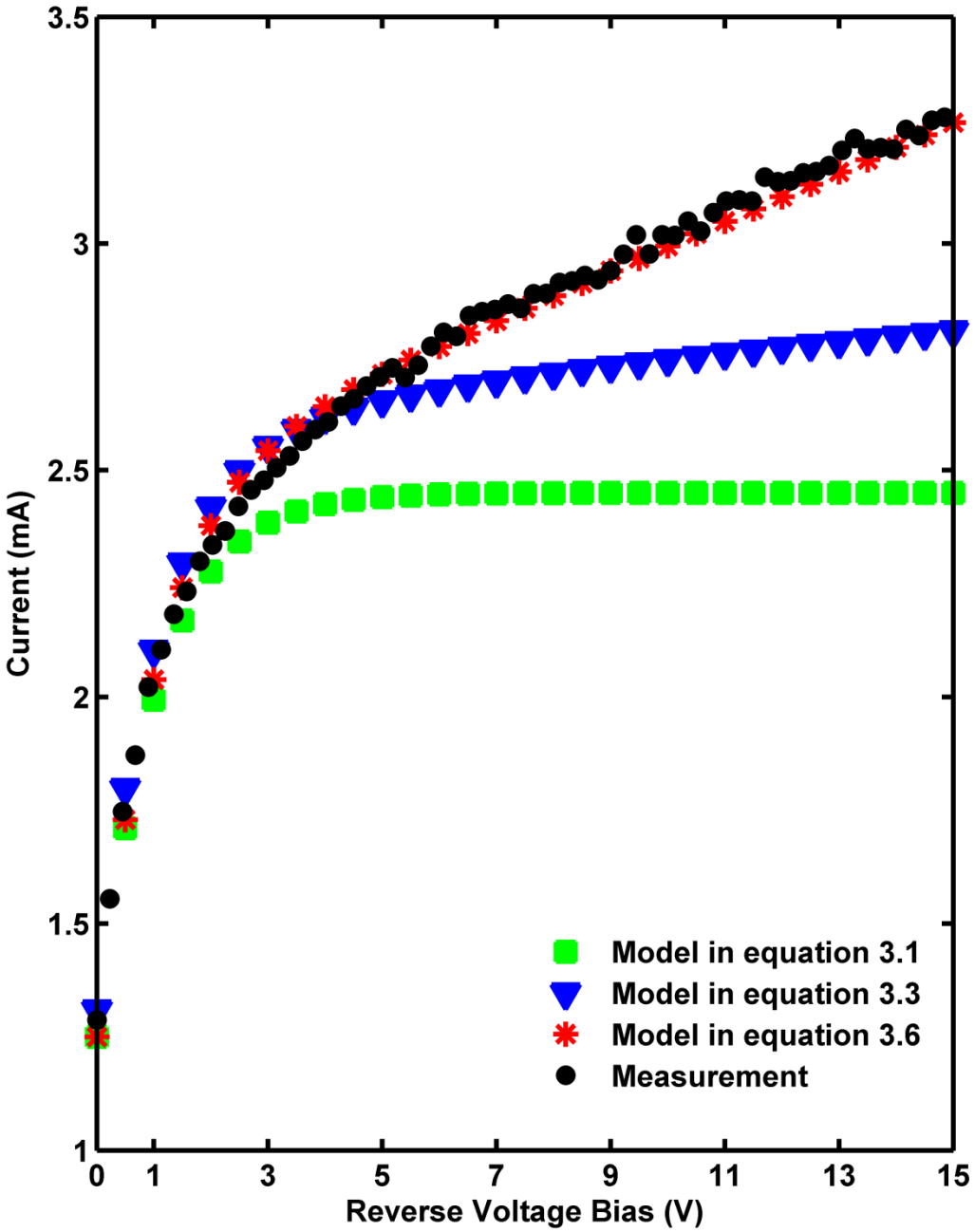


**Figure 3-4** Comparison of the models for I–V characteristics given in equation 3.1, equation 3.3 and equation 3.6 with the measurement data.

$$I = I_S\left\{\exp\left[\frac{-qV_R}{nK_BT}\right]-1\right\}+I_{ph}+I_g \tag{3.3}$$

As it can be seen from equation 3.2, $I_g$, is directly proportional with the SCR width. Since the Schottky junctions can be treated as single-sided p-n junctions,[134] the SCR width of the junction is then given by[135]

$$W=\sqrt{\frac{2\varepsilon_0\varepsilon_r}{q}\left(V_{bi}+V_R\right)\frac{1}{N_A}} \tag{3.4}$$

where, $\varepsilon_0$ is the permittivity of vacuum, $\varepsilon_r$, the relative permittivity of P3HT:PCBM, is assumed as 3,[136] $N_A$ is the concentration of p-type dopants in P3HT and $V_{bi}$ is the built-in voltage of the SB. The change in the SCR region width can be investigated with the small signal capacitance vs. reverse voltage bias measurement.[137] Because the SBs formed on BH devices, the small signal capacitance depends on frequency of the measurement.[137] In order to decrease the level of this dependency, the C-V measurements (Figure 3-5) were done below 100 Hz.[137] Reciprocal of the capacitance squared versus applied reverse voltage relation[136] which is given in equation 3.5, gives the Mott-Schottky curve in figure 3-6. The curve shows a linear behavior along the RVB and by extrapolating this straight line to the voltage-axis $V_{bi}$, can be extracted as 0.43 eV.[136]

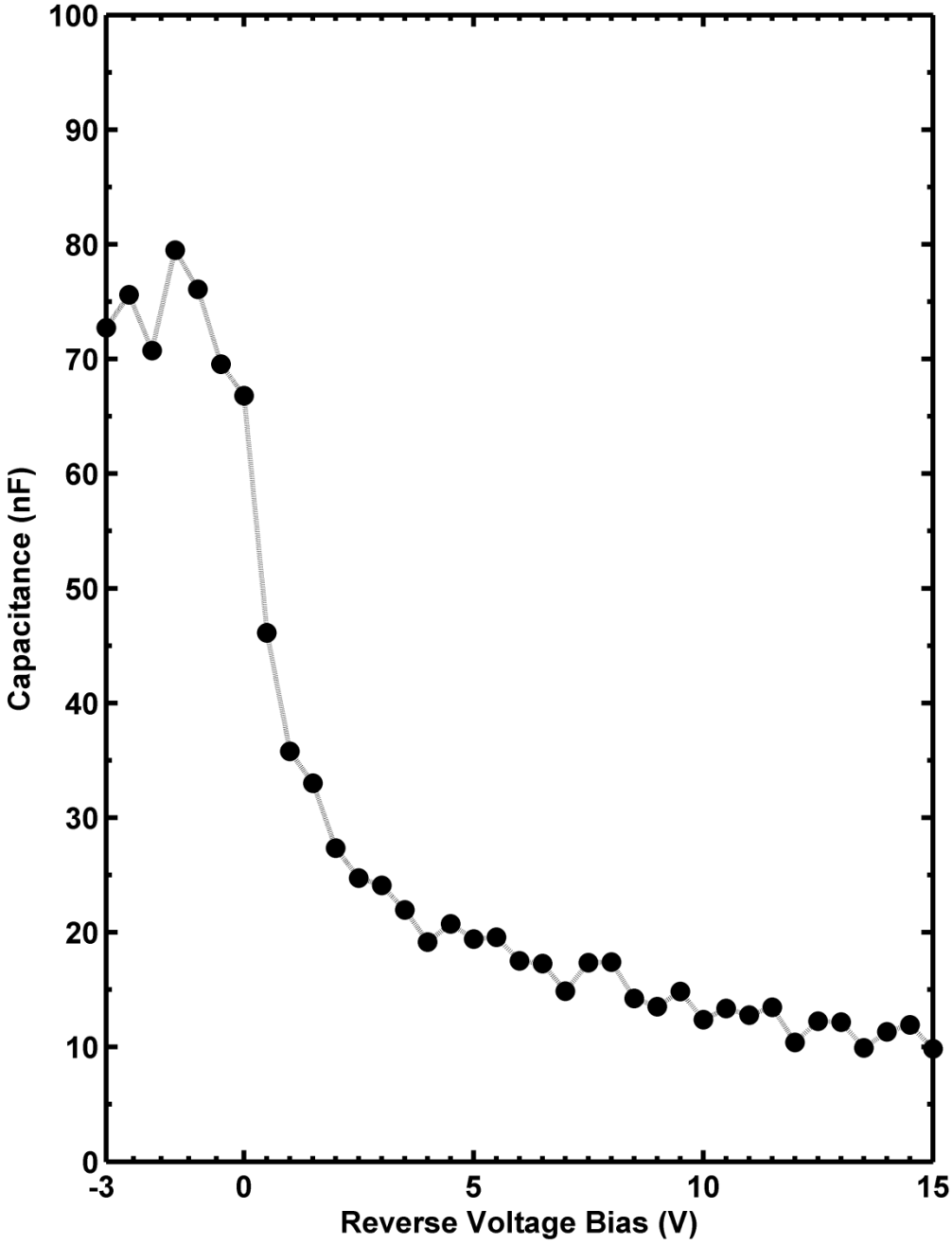


**Figure 3-5** SB C–V measurement (98 Hz) data for OPD having a 200 nm P3HT:PCBM active layer thickness.

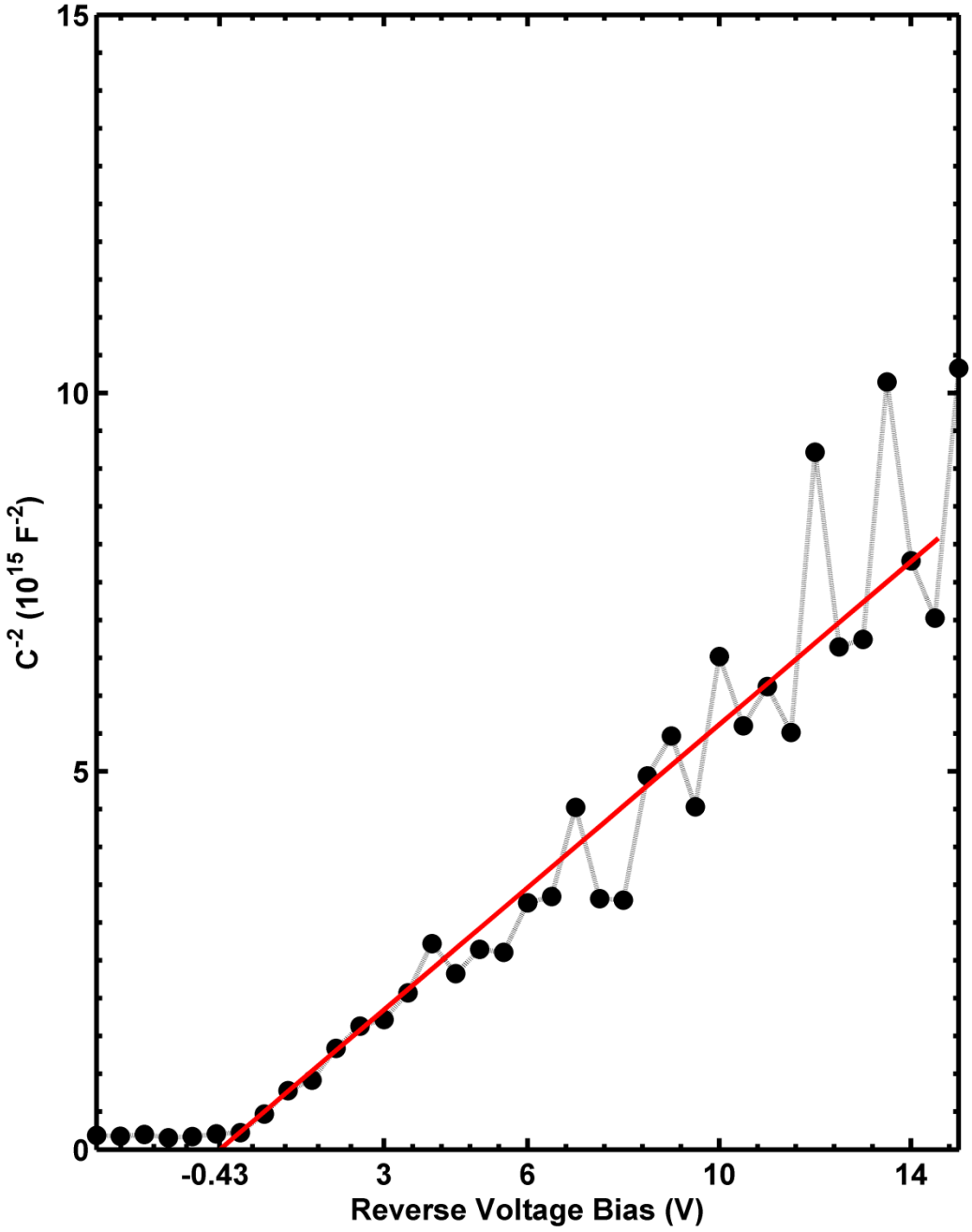


**Figure 3-6** Mott-Schottky Characteristic of 200 nm OPD calculated from C-V measurement.

$$C^{-2} = \frac{2(V_{bi} + V_R)}{A^2 q \varepsilon_0 \varepsilon_r N_A} \tag{3.5}$$

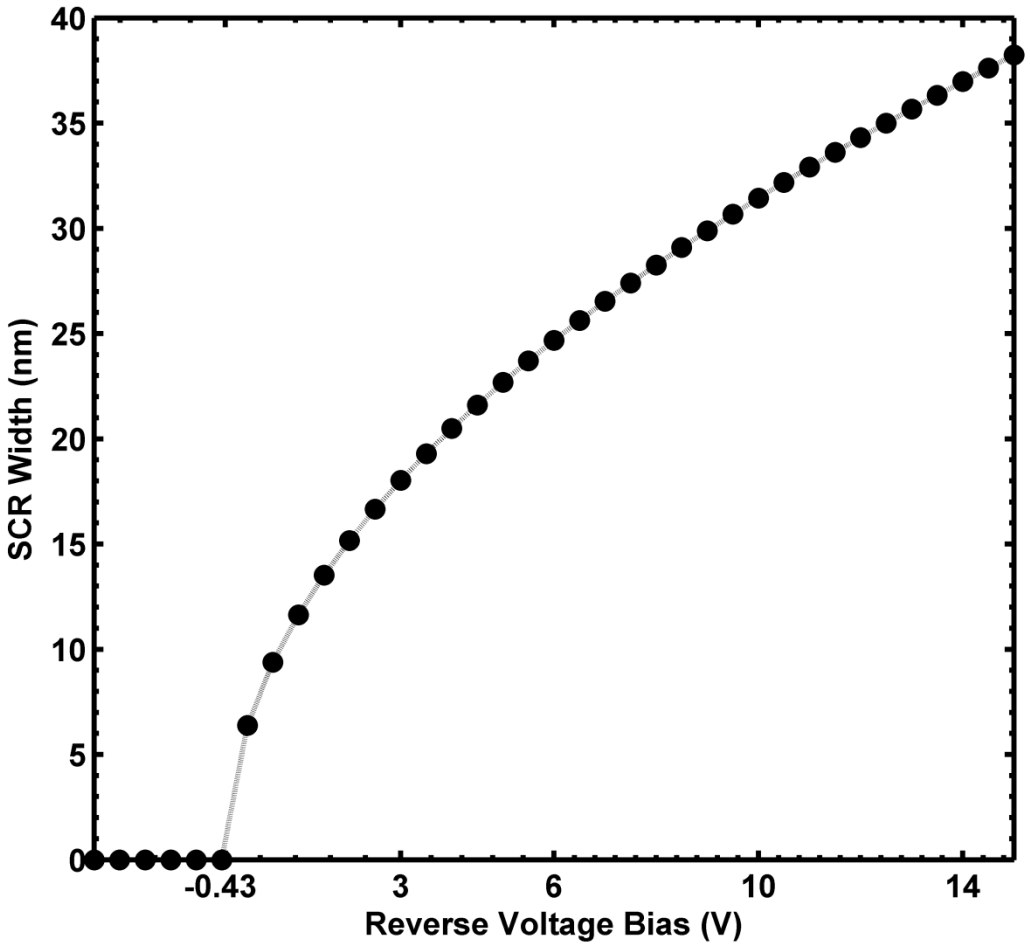


**Figure 3-7** Calculation results of SCR width of SBs on metal-organic semiconductor interface of OPDs according to RVB.

Accordingly, $N_A$ is then calculated as $3.5 \times 10^{18}$ cm$^{-3}$ from equation 3.5. The SCR width versus the RVB was then calculated as in figure 3-7. The results show that the SCR with in SBs increase with the increasing RVB from 10nm to 40nm. This increases $I_g$, so the total reverse bias current given in equation 3.3 with a constant slope as it can be seen in figure 3-4. Although, the I-V curve of this model is more accurate than the model in

equation 3.1 and involves the effect of change in SRC width, there is still difference between the measurement data and the results of equation 3.3 model. The slope of the measurement data is still larger than that of the model results. The reason for this may be explained as; the width of the SCR in SB does not only depend on the RVB.

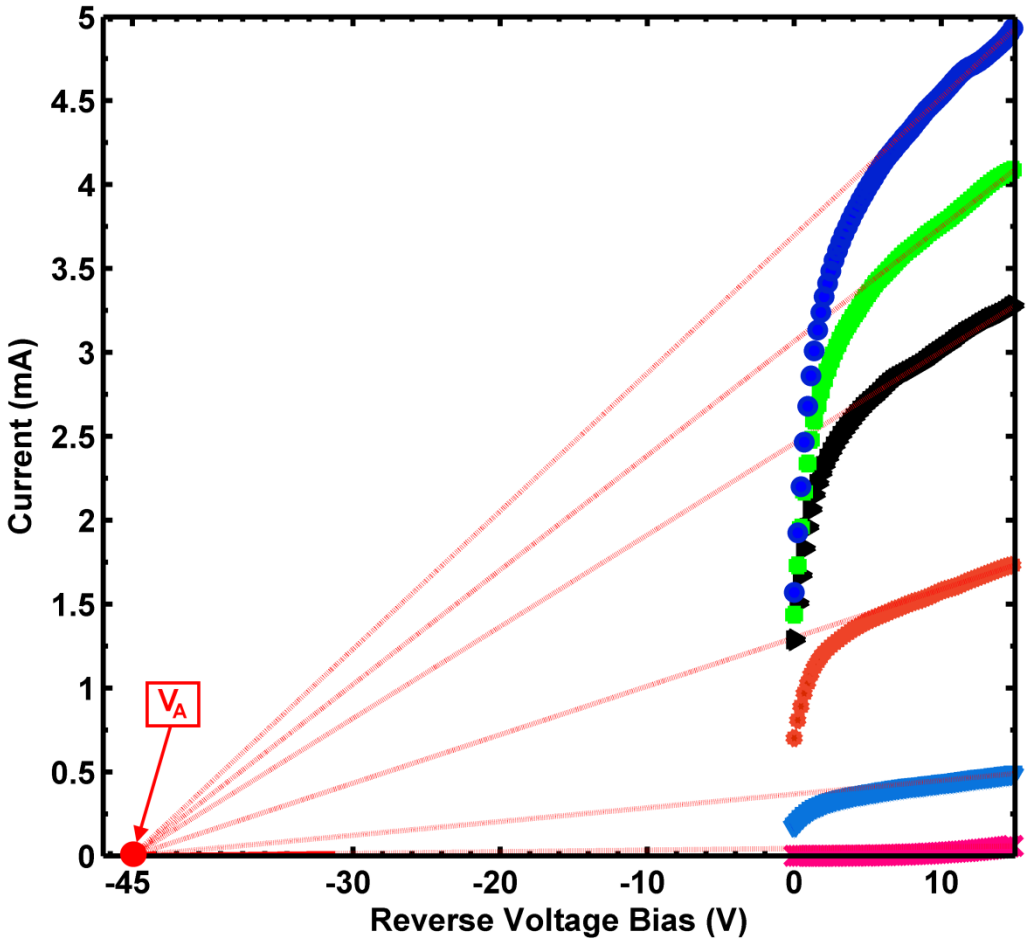


**Figure 3-8** Reverse bias I – V measurements under different ILPs.

In order to investigate the effect of ILP, power of light was increased from 0 $mW/mm^2$ to 1.34 $mW/mm^2$. In figure 3-8, the reverse bias I-V curves according to increasing ILP can be seen. It is clear that, as ILP increases, the slopes of the I-V curves

increase. When the tangents to the saturation region of these curves are extrapolated, all the tangent lines intersect the voltage-axis at the same voltage value, $V_A$. This shows that, the increase in the slopes of the curves has a certain order. This behavior looks similar to the $I_C$-$V_{CE}$ (collector current vs. collector-emitter bias) characteristic of n-p-n bipolar junction transistors (BJT).[131] In BJTs, the base current causes the shift in curves by injecting electrons, similarly, in OPDs, the ILP works like the base current by exciting electrons/holes. The increase in the slope of the curves in BJTs is because of the increasing SCR width in base due to the increasing RVB on base-collector junction, i.e. Early Effect.[131] Similarly, as mentioned in equation 3.3 model, SCR width has the same effect on the I-V characteristics of OPDs but that model was not enough for handling all the effects on SCR width.

Assuming that the change in slopes of the I-V curves does only depend on the change in SCR width, according to figure 3-8, the increasing ILP, then, increases the SCR width. Because the Early model theoretically involves all the effect of increasing SCR width on the I-V characteristic, using a model similar to the Early model will involve all the effects, the effect of RVB bias and the effect of ILP, on the SCR width. Accordingly, $I_g$ was removed from the model in equation 3.3 and the new coefficient similar to the Early model was introduced to the model as given in equation 3.6.

$$I = \left( -I_S \left\{ exp\left[ \frac{-qV_R}{nK_BT} \right] - 1 \right\} + I_{ph} \right) \left( 1 - \frac{V_R}{V_A} \right) \tag{3.6}$$

In figure 3-4, it is obvious that equation 3.6 model is much more accurate than the other models given above, so it can be said that this model involves both the effect of RVB and ILP on the SCR width of the SB. With the assumption above, the increase in the SRC width due to increasing ILP was extracted from the difference between the equation 3.3 model and the equation 3.6 model as it can be seen in figure 3-9. It can easily be seen that the ILP has an effect on the width of the depletion region of the SBs in OPDs. Also in figure 3-10, the dependency of slopes to the ILP can be seen.

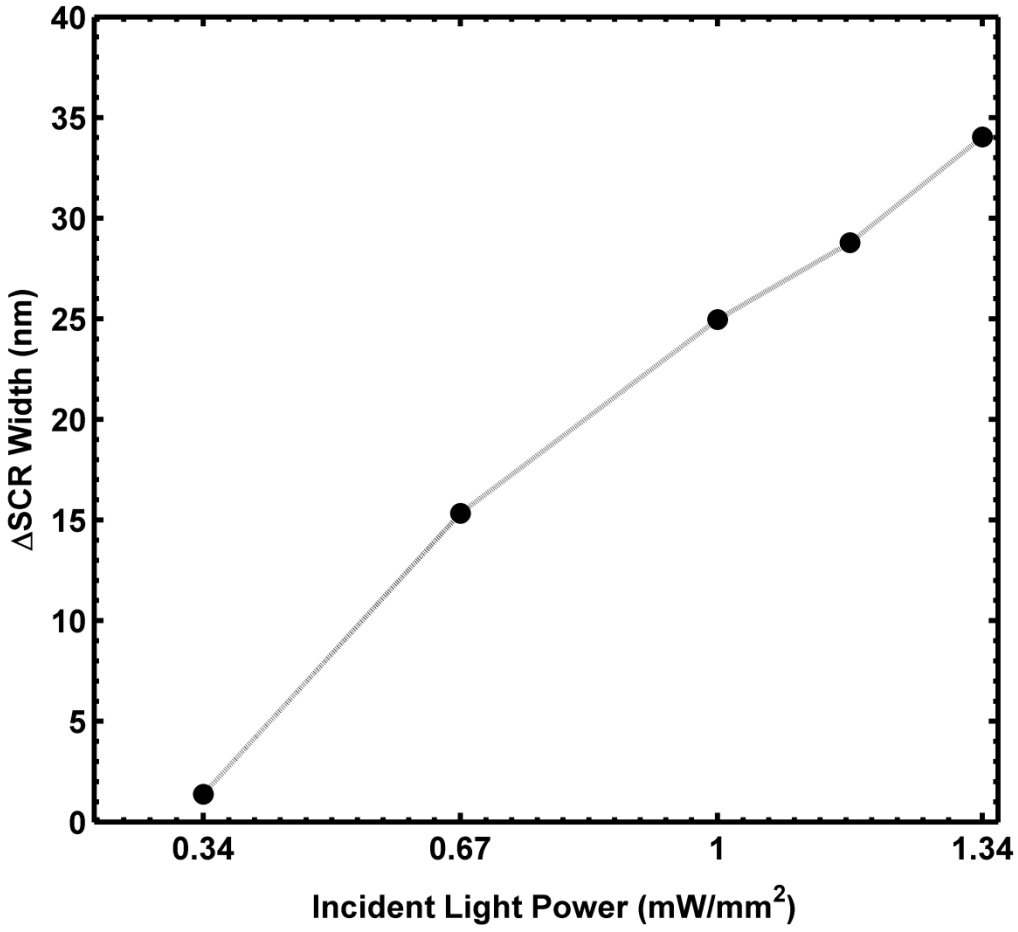


**Figure 3-9** Calculation results of the increase in the SCR width of the OPDs due to the ILP.

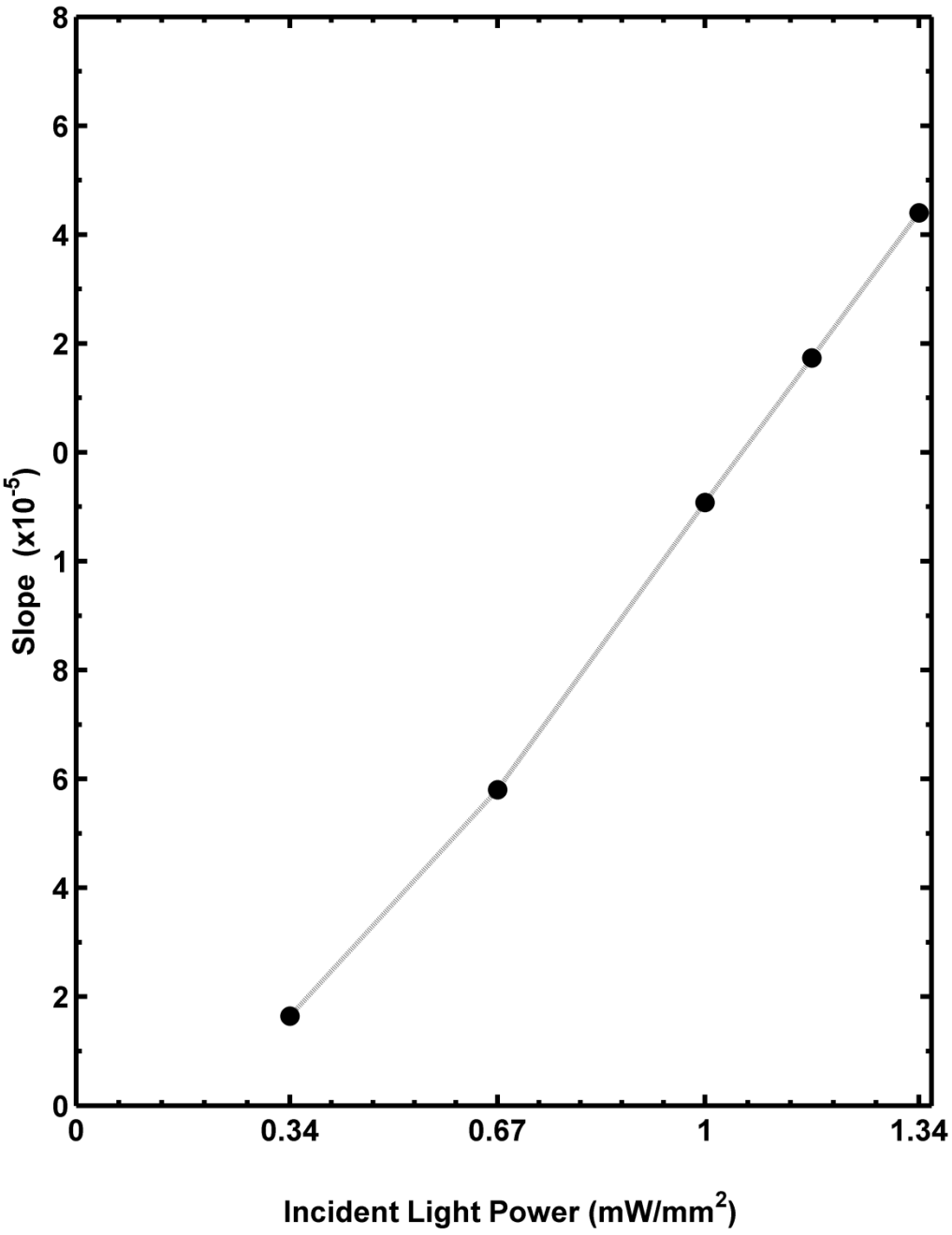


**Figure 3-10** Slope of saturation region I-V characteristics of OPDs according to ILP.

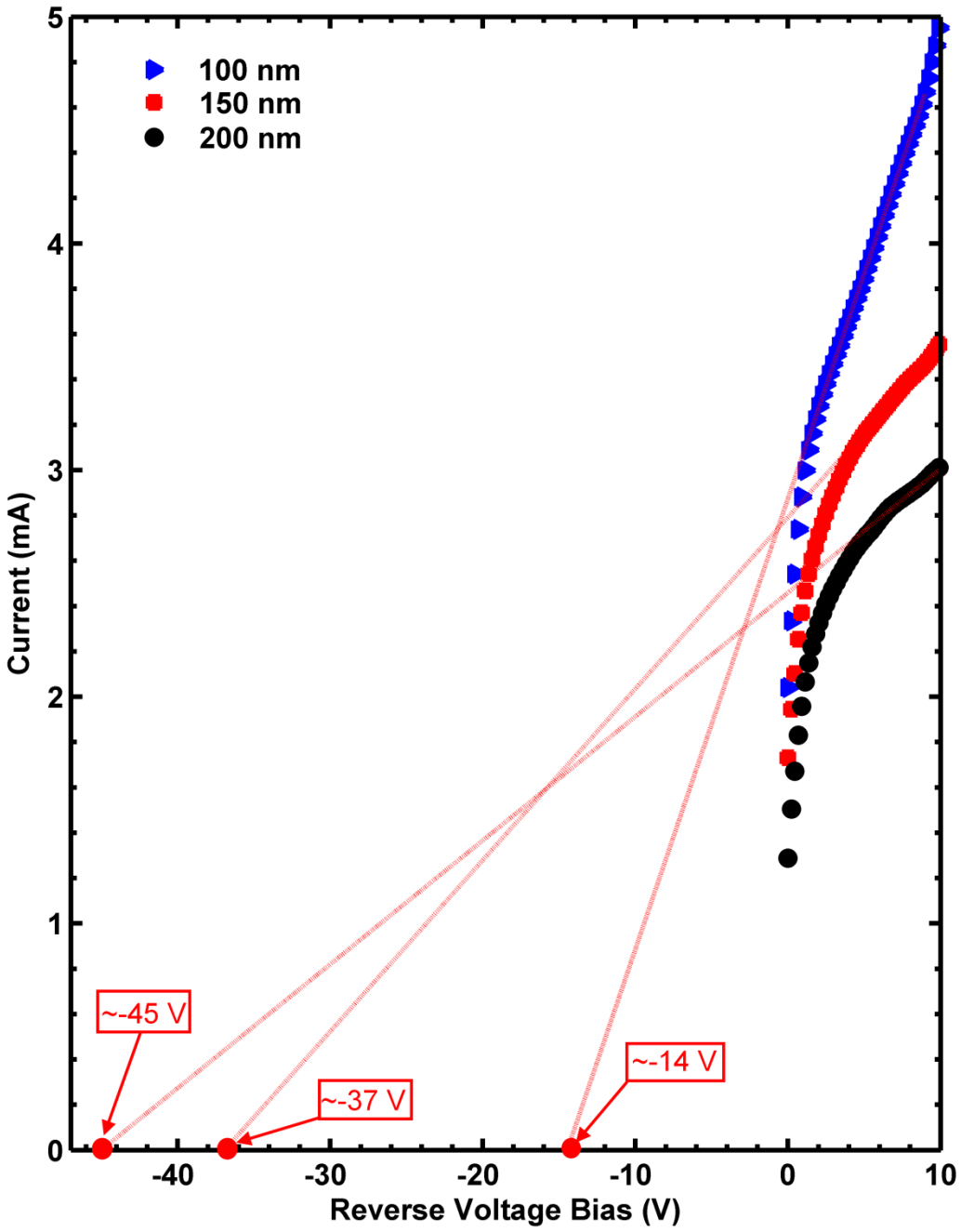


**Figure 3-11** Reverse bias I–V measurements of OPDs having different P3HT:PCBM thicknesses; slopes of the saturation region in the I-V characteristics is inversely proportional with the OPD active layer thickness.

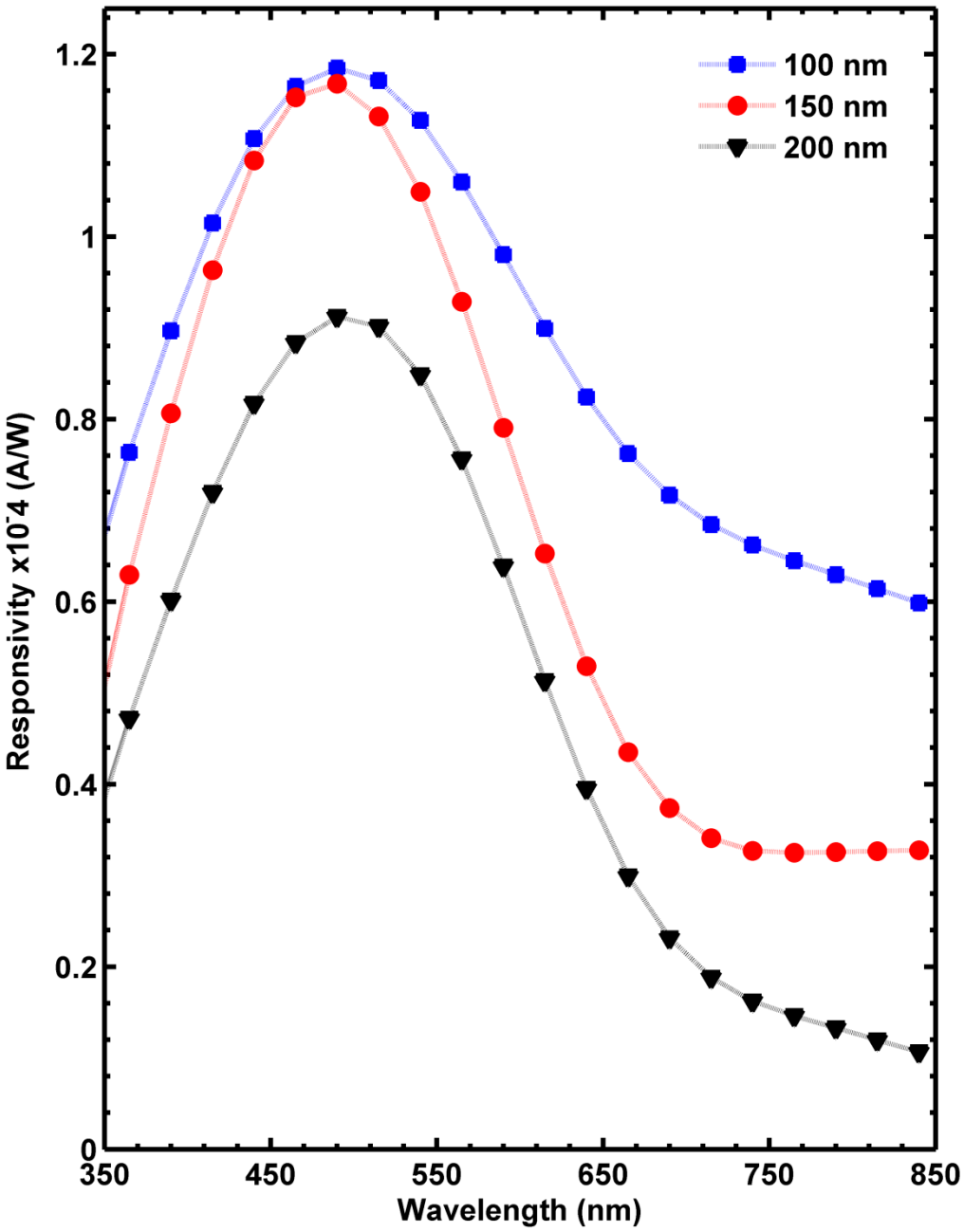


**Figure 3-12** Responsivity spectra of the OPDs having different P3HT:PCBM active layer thicknesses.

In order to investigate the effect of SCRs width of SBs on the performance of the devices, three different devices with different active layer thicknesses were fabricated. The reason for this is to understand the effect of total device thickness to SCR width ratio on the performance with the assumption that $N_A$ and $V_{bi}$ do not depend on the device thickness. In figure 3-11, under the same ILP, devices having different thicknesses show different $V_A$ values. The thinner devices have smaller $V_A$ values, larger slopes on I-V curves and higher current values. This indicates a better photodetection performance of the devices with the decreasing total device thickness to SCR width ratio or the thicker the SCR on SB, the higher the performance. In figure 3-12, the thinnest device having the smallest $V_A$, shows the highest responsivity so the highest performance. But, on the other hand, under excessive ILP, the SCR width becomes comparable with the total device thickness, or the ratio gets closer to 1. This makes the gap between the SCR region and ITO contact small enough that charges can tunnel through and the device will break down. As $V_A$ decreases, the photodetection performance of the devices increase but when $V_A$ becomes too close zero, the devices will instantly break down and behave as ohmic devices.

## 3.4 Conclusion

In summary, the ILP has an effect on the SBs of the OPDs by changing the width of the SCRs. This change directly affects the reverse bias I-V curves by increasing the current values and the slope of the curves. The photodetection performance of the devices tends to increase with the increasing light power due to the increasing SCR width. But under excessive ILP; the SCRs will merge, the devices will break down and work as ohmic devices.

## Chapter 4:

## Increased Absorption in Band Energy Structure Arranged λ-DNA/Organic Bulk Heterojunction Photovoltaic Devices with Colloidal Platinum Nanoparticle Surface Plasmons

### 4.1 Introduction

In recent years, organic bulk heterojunction (BHJ) photovoltaic devices have attracted great attention due to the advantages of light weight, flexibility, tunable optical properties and low cost large area fabrication.[138-140] The active layer of these devices is fabricated by cascading solutions of conjugated polymers and fullerene derivatives or nanoparticles. Despite of their promising benefits, the power conversion of BHJ photovoltaics are limited due to their short exciton diffusion lengths of the polymers in the active layer[141], short drift length of the charge carriers[142], non-ordered phase separation[143], low dissociation probability of excitons and inefficient hopping carrier transport.

The BHJ photovoltaic device performance improving can be achieved by using several approaches. One approach is to introduce organic/inorganic nanostructures including carbon nanotubes (CNT)[144], nanorods[145], nanoparticles[146], deoxyribonucleic acid (DNA) complexes[147], nanowires[148] and etc. to increase the exciton dissociation, charge carrier transport in and inter material by enhancing the efficiency of the hooping carrier transport. This can be achieved by arranging the band energy diagram of the BHJ photovoltaic devices by introducing hole collecting and

electron blocking layers into the device structure. The hole collection and electron blocking effect of DNA complexes has already been shown.[104, 147] One other approach is to improving device photon absorption percentage by using plasmonic effect of nanoparticles.[149, 150]

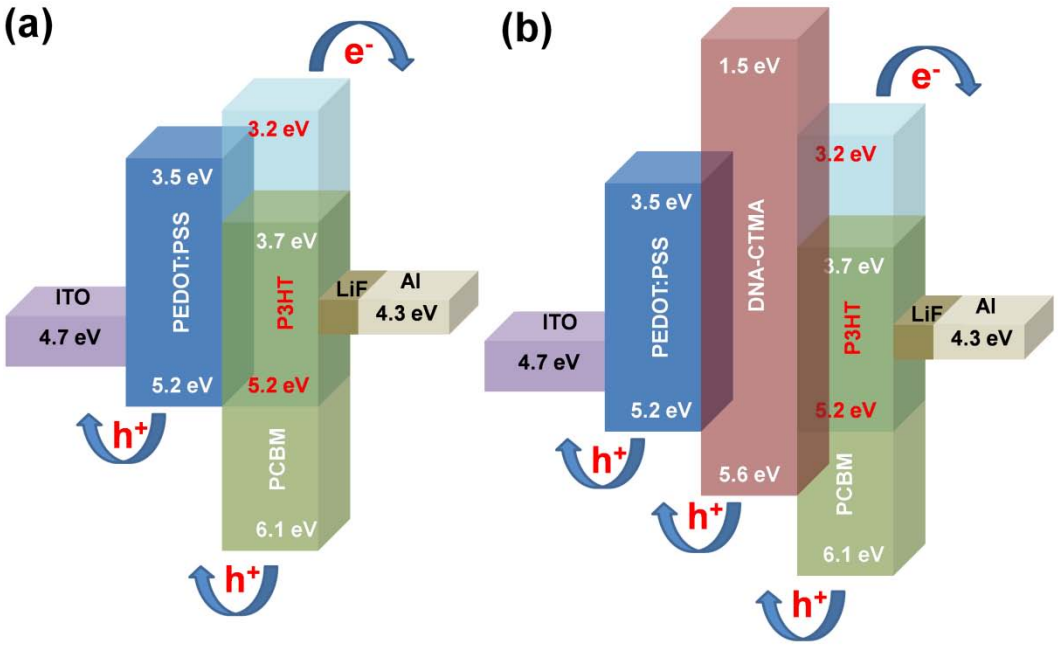


**Figure 4-1** Band energy diagrams of organic BHJ photovoltaic devices. (a) Control sample with the well known band energy diagram, (b) DNA complex layer introduced between PEDOT:PSS and P3HT:PCBM layers as hole collecting and electron blocking layer.

A plasmon is a quantum of plasma oscillation. The plasmon is a quasiparticle resulting from the quantization of plasma oscillations just as photons and phonons are quantizations of light and mechanical vibrations, respectively. Thus, plasmons are collective oscillations of the free electron gas density, for example, at optical frequencies. Plasmons can couple with a photon to create another quasiparticle called a plasma polariton.

Photovoltaic devices exploiting this effect of nanoparticles are called plasmonic photovoltaic devices. A major limitation in all thin film photovoltaics technologies is that their absorbance of near-bandgap light is ineffective. Therefore, structuring the photovoltaic devices so that light is trapped inside, in order to increase the absorbance, is very important. It is possible to achieve light-trapping by forming a wavelength-scale texture on the substrate and then depositing the thin-film photovoltaic device on top, and large increases in photocurrent have been achieved in this way.[151, 152] However, rough semiconductor surface results in increased surface recombination, and semiconductors deposited on rough surfaces typically have low material quality. A new method for increasing the light absorption that has emerged recently is the use of scattering from noble metal nanoparticles such as gold, silver, platinum and etc., excited at their surface plasmon resonance.

In this study, we combined the two improvement methods, improving the charge carrier transport and improving absorption of the BHJ photovoltaic devices. For charge carrier transport improvement, we presented DNA complexes as hole collecting and electron blocking layer on the anode side of the devices by using them as hole collecting and band energy diagram arranging layer. The band energy diagrams for the devices are given in figure 4-1. In figure 4-1a the band energy diagram for the control sample is given and the band energy diagram for DNA complex layer introduced device is given in figure 4-1b. The DNA complexes have the highest occupied molecular orbital (HOMO) level of 5.6 eV[104] which creates a mid step between the photoactive polymer poly(3-hexylthiophene):phenyl-$C_{61}$-butyric acid methyl ester (P3HT:PCBM) and the anode

electrode polymer poly(ethylene-dioxythiophene):poly(styrenesulphonate) (PEDOT:PSS) and lowest unoccupied molecular orbital (LUMO) level of 1.5 eV[147] which creates a high potential difference between the LUMO of the P3HT:PCBM layer and blocks the electrons to be transferred to anode electrode. For absorption improvement with plasmonic effect of the particles, we present colloidal platinum nanoparticles as the surface plasmons.

### 4.2 Experimental

Four separate device structure have been fabricated for testing and comparing the performance of organic BHJ photovoltaic devices (Figure 4-2).

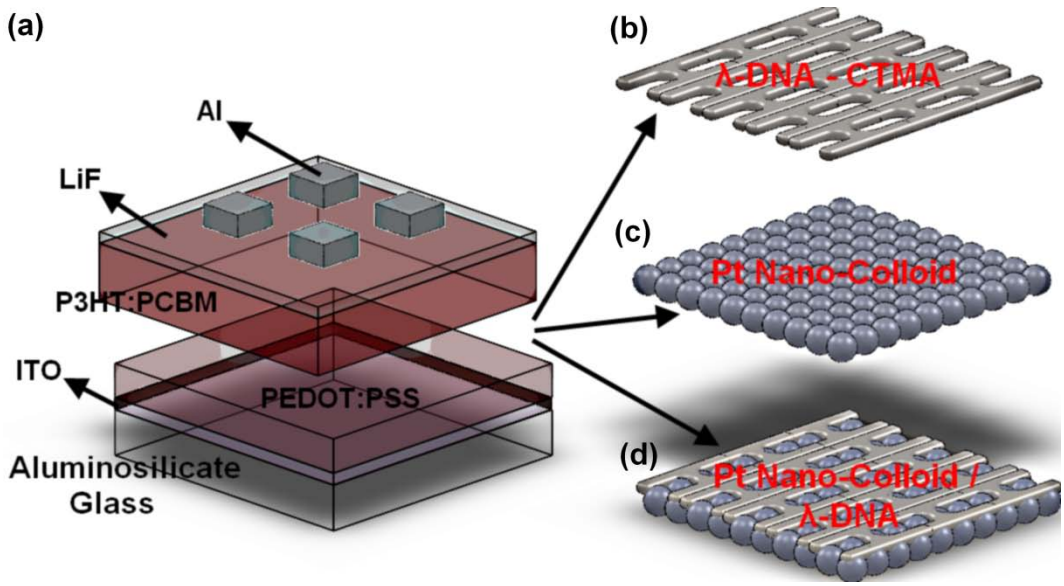


**Figure 4-2** Structure of organic BHJ photovoltaic devices used in this study. (a) Most commonly used structure for organic BHJ photovoltaic devices, control sample, (b) λ-DNA-CTMA layer introduced device structure, (c) PtNC surface plasmon layer introduced device structure, (d) PtNC/DNA-CTMA mixture layer introduced device structure

First device, figure 4-2a, is the control sample which has the most commonly used device structure. For the fabrication of control sample for organic BHJs, first, ITO coated glass substrates from Delta Technologies (15 Ω/sq) were used as the transparent anode contact. The glass substrates were cleaned by ultrasonification in subsequent solutions such as; detergent, de-ionized (di) water for rinsing, acetone and isopropanol alcohol (IPA). After the cleaning process, the cleaned ITO coated glass substrates were left for annealing for 12 hours in nitrogen ($N_2$) at 70 °C. This process was followed by oxygen ($O_2$) plasma etching for 5 minutes to change the surface properties of the substrates from hydrophobic to hydrophilic.[105] Following the plasma etching, a thin layer of PEDOT:PSS was spin-coated from aqueous solution at 4000 rpm for 40 seconds, after passing through 0.45 μm syringe filter. The substrate was then annealed at 150 °C for 15 minutes in $N_2$. The benefits of this annealing on the surface properties have been previously shown.[106] After the deposition of the PEDOT:PSS layer, the substrates were transferred into a $N_2$ filled glove-box system. A mixture of 1:1 P3HT and PCBM blend which had been dissolved in 1 ml 1,2-dichlorobenzene (ODCB) to make a 60 mg/ml solution, and stirred for 12 hours at 80 °C was filtered through a 0.22 μm filter and then deposited on top of the PEDOT:PSS layer at 700 rpm for 50 seconds by spin coating. High temperature annealing treatment was carried in $N_2$ environment for 1 hour at 120 °C. For the cathode contact, first 1 nm of protective layer which is usually lithium fluoride (LiF) is deposited on top of active polymer blend via vacuum thermal evaporation (Temescal BJD 1800). Then, 100 nm thick Al layer was deposited on top of P3HT:PCBM layer via vacuum thermal evaporation (Temescal BJD 1800).

Second device, figure 4-2b, is the organic BHJ photovoltaic device which has DNA complex layer as the band energy structure arrangement and hole collecting/electron blocking layer. The fabrication of the device starts with the preparation of the DNA complex. First, DNA-CTMA electron blocking-hole collecting layer in the device structure was synthesized by mixing Lambda Phage DNA (λ-DNA), (Sigma-Aldrich, Product No:D3654, Non-methylated from Escherichia coli host strain GM119 ($r_m^-, dam^-, dcm^-$), strains in the form of buffered aqueous solution and Cetyltrimethylammonium (CTMA) chloride solution, (Sigma-Aldrich, Product No: 292737, 25 wt. % in $H_2O$). 5 µg/ml DNA and 1 ml of CTMA chloride were diluted in 15 ml of di-water separately by ultrasonicating the solutions for 1 hour. DNA solution was added into the CTMA solution while stirring the mixture as it was added. For the precipitation process the DNA-CTMA mixture was centrifuged for 1 minute at 500 rpm. The liquid in the vessel was taken with a syringe and the DNA-CTMA precipitates left in the vessel were dispensed on a filter paper. The precipitates were dried in a nitrogen ($N_2$) filled oven at 40°C for 12 hours. For the preparation process of the DNA-CTMA solution used in the fabrication of the organic BHJ photovoltaic devices; 100 mg of DNA-CTMA with 2 ml of methanol mixed in an aluminum (Al) foil-wrapped bottle to prevent light degradation. Then, the air left inside the bottle was vacuumed and Ar pumped in to reduce oxidation. The solution was stirred on a hot plate placed in a $N_2$ filled glove-box for 24 hours at 60°C. Following the preparetion of the DNA-CTMA solution the fabrication of the photovoltaic devices starts. DNA-CTMA layer is deposited via spin coating of the solution at 1500 rpm between PEDOT:PSS and P3HT:PCBM layers in the

structure of the control sample.[147] After the deposition of the DNA-CTMA layer the samples are annealed for 5 minutes at 40$^{o}$C in a $N_2$ filled glove-box. The rest of the fabrications steps, deposition of P3HT:PCBM, LiF and Al are same with the control samples.

Third device, figure 4-2c, is the organic BHJ photovoltaic device which has colloidal Pt nanoparticles (PtNC) for the improvement of device photon absorption rate. PtNC used as the surface plasmons in the device were synthesized by Rampino and Nord[153, 154] method. The Pt was incorporated in the form of potassium tetrachloroplatinate(II) ($K_2PtCl_4$) (Sigma-Aldrich, Product No:520853, ≥99.9% trace metals basis) solution. A solution of $1 \times 10^{-5}$ M $K_2PtCl_4$ was prepared in 5 ml de-ionized water (di-water) to which 0.2 ml of 0.1 M sodium polyacrylic acid (Sigma-Aldrich, Product No: 420344, average Mw ~2,100) was added. The solution was then ultrasonicated for 10 minutes and left for aging for 24 hours. Later, Argon (Ar) gas was bubbled through the aged solution for 20 min. For reduction of the Pt ions, hydrogen ($H_2$) gas was bubbled vigorously through the solution for 10 minutes. Then the reaction mixture was incubated at room temperature for 12 hours and centrifuged for 10 seconds at 500 rpm. After centrifuge, the upper 2 ml of the solution was taken with a syringe and dispensed in a clean vessel for later use. The PtNC layer is deposited via spin coating of the solution at 1500 rpm between the PEDOT:PSS and P3HT:PCBM layers in the the structure of the control sample. After the deposition of the PtNC layer the samples are annealed for 5 minutes at 40$^{o}$C. The rest of the fabrications steps are same with the control samples.

The Fourth device, figure 4-2d, is the organic BHJ photovoltaic device which has DNA-CTMA for the improvement of interlayer charge carrier hopping and colloidal Pt nanoparticles for the improvement of device photon absorption rate. The previously synthesized 2 ml of colloidal PtNC solution is first mixed with 2 ml of DNA-CTMA solution by stirred for 1 hour and ultrasonificating the solution for 10 minutes. The PtNC/DNA-CTMA mixture is deposited via spin coating of the solution at 1500 rpm between PEDOT:PSS and P3HT:PCBM layers in the structure of the control sample. After the deposition of the PtNC/DNA-CTMA layer, the samples are annealed for 5 minutes at $40^{o}$C. The rest of the fabrications steps are same with the control samples.

In order to define the order of the deposition steps to arrange a proper band energy diagram for the charge carriers, first the work function of the PtNCs is measured. Since the work function values for metallic materials, zero-bandgap, can be measured by using thermionic emission method [155-157], a device has been designed and fabricated for this measurement (Figure 4-3). Fabrication of the device starts with the deposition of the ptNC solution on top of a 5.08 cm in length, 2.54 cm in depth and 5 mm in thickness ceramic substrate. Aluminum Nitride (AlN) ceramic is used as the substrate because of its high thermal conductivity and electrical insulation properties.[158] After the deposition of the PtNC, 100 nm thick gold (Au) electrode is deposited on top of PtNC particles only on one side of the sample for thermionic emission current measurements via thermal evaporation.

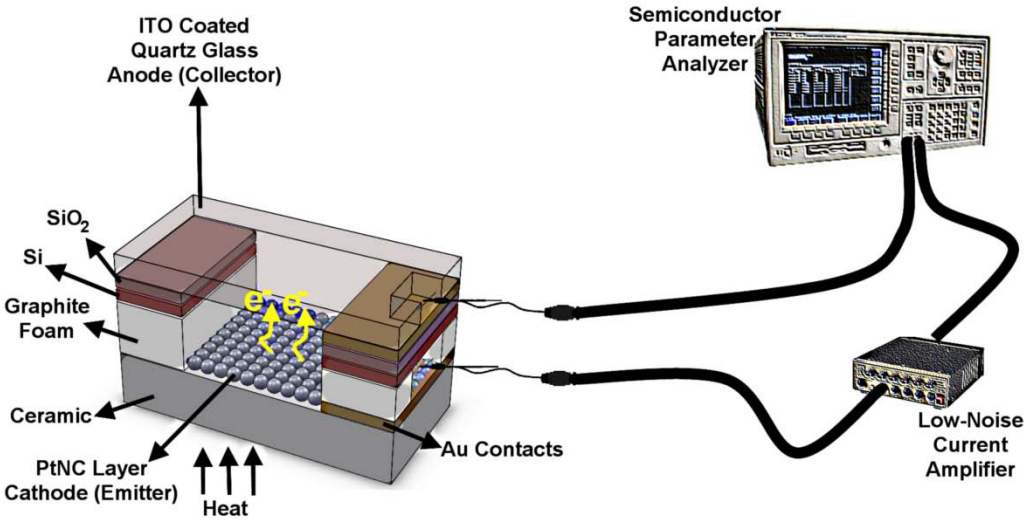


**Figure 4-3** Device which has been designed and fabricated for thermionic emission measurements of PtNCs and the measurement setup.

In order to protect the anode side of the device from heat dissipation graphite foam is used as the heat insulator between cathode (emitter) and anode (collector) electrodes.[159, 160] For this, graphite foam blocks given in figure 4-3 are cut from a bulk grapite foam by using doctors blade and adhered to the substrate by using thermal glue. The cut graphite foam blocks are ~1.27 cm in length, 2.54 cm in depth and ~1 mm in thickness. A gap has been prepared by cutting the block given on right hand side of the sample which Au electrode was deposited. For insulating the unintended electrical current flow between the anode and the cathode side Si/$SiO_2$ wafer pieces are used. Wafer pieces are cut according to the dimensions of the graphite foam blocks and adhered on them by using thermal glue. Then, 100 nm thick gold (Au) electrode is deposited on top of $SiO_2$ only on one side of the sample for thermionic emission current measurements via thermal evaporation as given in figure 4-3, on right hand side of the sample. For anode side of the device, 5.08 cm by 2.54 cm ITO coated glass from Delta

Technologies (15 Ω/sq) that has a cut part on one side is used. The ITO coated glass is adhered to the sample by using electrically conductive glue mixed with gold nanoparticles for increasing the electrical conductivity of the glue.

The measurement is done in MMR vacuum probe station with K-20 Programmable Temperature Controller. Two probes which are in contact with the emitter electrode and collector electrodes are used for the measurement. Probes are connected to Agilent 4155 Semiconductor parameter analyzer for sweeping applied voltage over the anode-cathode from 0-to-100V which creates an increasing electromagnetic field between the emitter and collector electrodes and increases the collection rate of the emitted electrons from the surface and LMC6001 Ultra Ultra-Low Input Current Amplifier for pre-amplification of the very low thermionic emission current before measured by the semiconductor parameter analyzer. First, the pressure in the vacuum probe station is set to ~$10^{-6}$ mmHg. Then, the temperature applied to the sample is swept from 600-to-650 K by 5 K steps and the thermionic emission current is measured for each temperature step accordingly.

Electrical and spectral characterization of photovoltaic devices is performed in both dark and illuminated conditions. Newport 9600 150 W Solar Simulator which is calibrated to generate illumination power equals to 1 sun (AM 1.5 G) is used as the light source. Current-Voltage (I-V) characteristics of the devices are measured by using Agilent 4155C Semiconductor Parameter Analyzer. For spectral performance analysis such as external quantum efficiency (EQE) and internal quantum efficiency (IQE) 30

band-pass optical filters in the spectral range of 350-to-800 nm wavelengths used to filter white light into monochromatic light for making the calculation of number of photons which is the denominator in efficiency calculations (Chapter 2.4.5.1 Optical (Spectral) Characterization) possible.

Other devices used in the measurements are Perkins Elmer Lambda 35, UV/VIS Spectrometer for absorbance/transmittance/extinction measurements, Perkins Elmer LS 55 Luminescence Spectrometer for PtNC solution photoluminescence measurements and Veeco Multimode V for atomic force microscopy (AFM) imaging.

### 4.3 Results and Discussion

In this study, we used solution-processable PtNC to trigger the localized surface plasmon resonance. After the synthesis of the PtNC, the solution is used for the extinction measurement for determination of the plasmon resonance frequency values of the PtNCs. The extinction spectrum of the PtNCs, determined using UV/VIS spectroscopy, is displayed in figure 4-4. As it can be seen from the figure, the plasmon resonance frequency of the solution processable PtNCs in solution was located at around 550 nm. The plasmonic resonance regime of the PtNCs is close to the absorption peak of the P3HT/PCBM blends of the organic BHJ photovoltaic devices given in figure 4-5. Thereby this enhancement is suggesting enhanced light-harvesting efficiency in the active layer of the devices. As it can be seen from the figure 4-5 introduction of PtNCs into the device structure enhanced the absorption of the devices without making a significant increase in the thickness of the active layers of the devices.

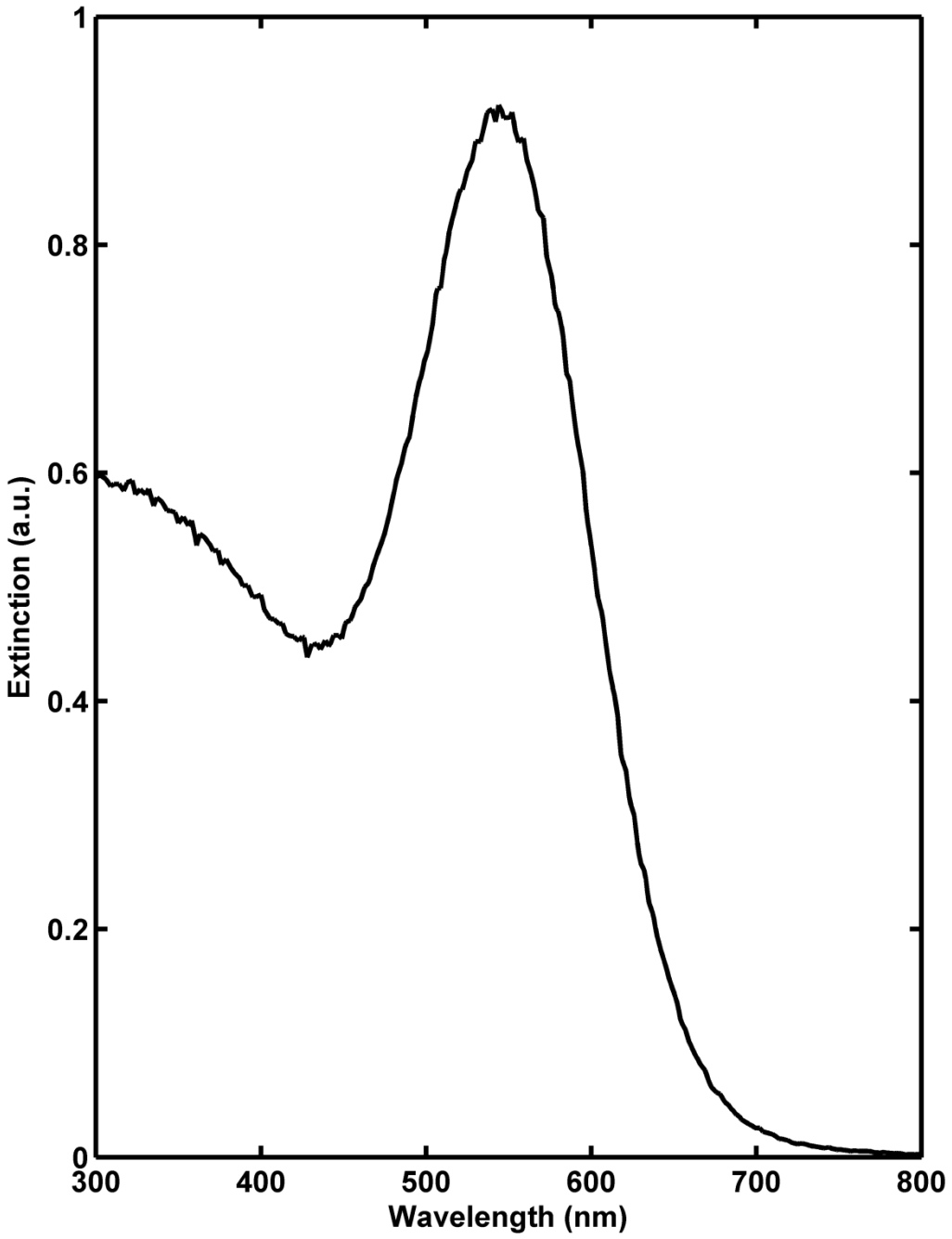


**Figure 4-4** UV/VIS extinction spectrum of the solution processable PtNCs measured in the spectral range of 300-to-800 nm wavelengths.

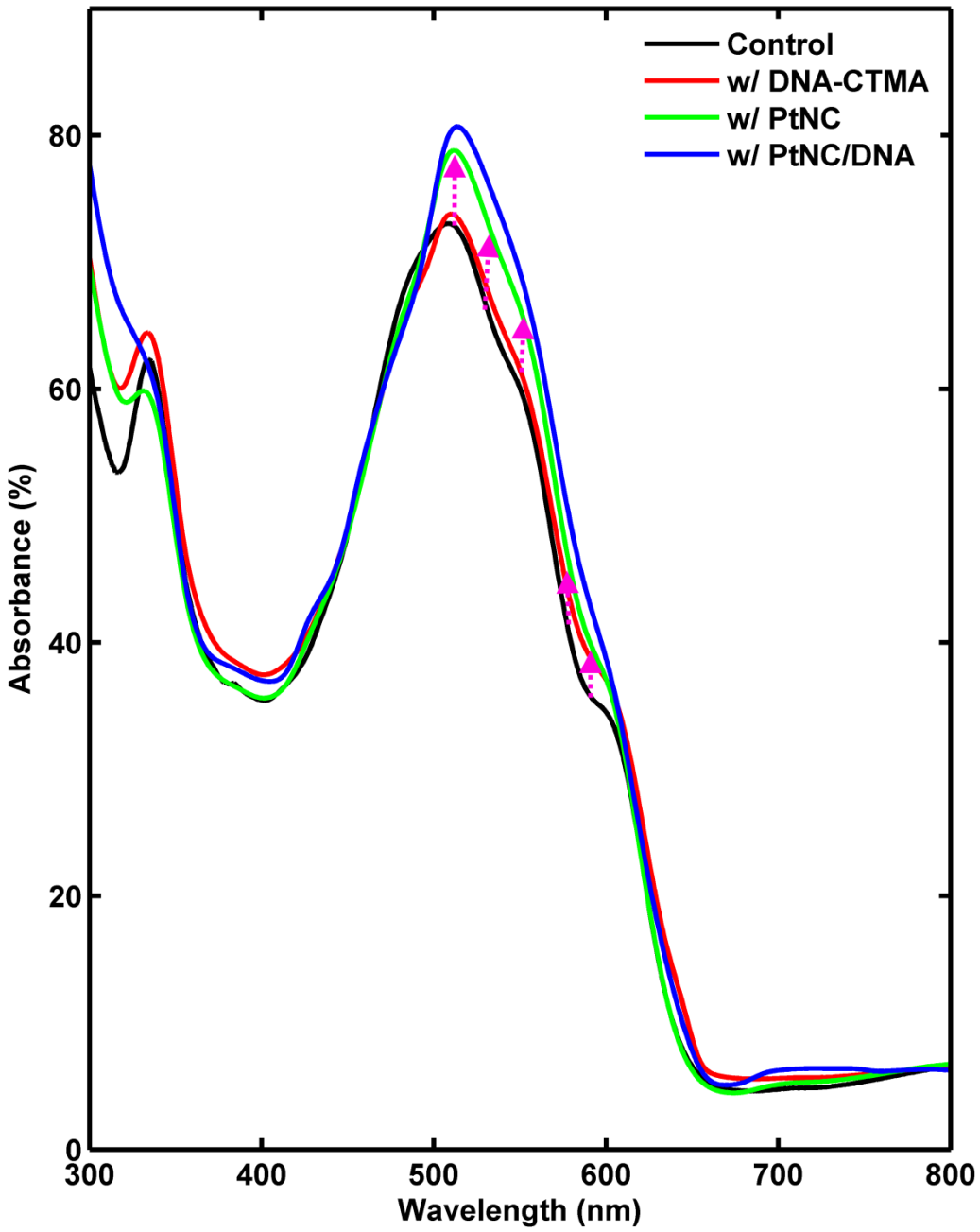


**Figure 4-5** UV/VIS absorbance spectrum of the photovoltaic devices fabricated with four different device structures. Purple arrows indicate the light-harvesting enhancement due to surface plasmon resonance.

In order to measure the average particle size and particle distribution throughout the surface, AFM images of PtNCs deposited on $Si/SiO_2$ substrates are taken. In figure 4-6, AFM image of the PtNCs is given. It can easily be seen from the figure that PtNCs which have been deposited on the surface via spin coating are distributed evenly throughout the surface. This shows that the particle suspension and distribution in the solution-processable PtNC solution was achieved and homogeneous. Additionally, in figure 4-7, a close-up view of the AFM image of PtNCs deposited on $Si/SiO_2$ substrate is given for illustrating the particle sizes in both vertical and horizontal scales. There are particles having sizes in the range of 5-to-80 nm in diameter. From the calculations throughout the surface, the average particle size of the synthesized PtNCs is determined as ~25 nm in diameter.

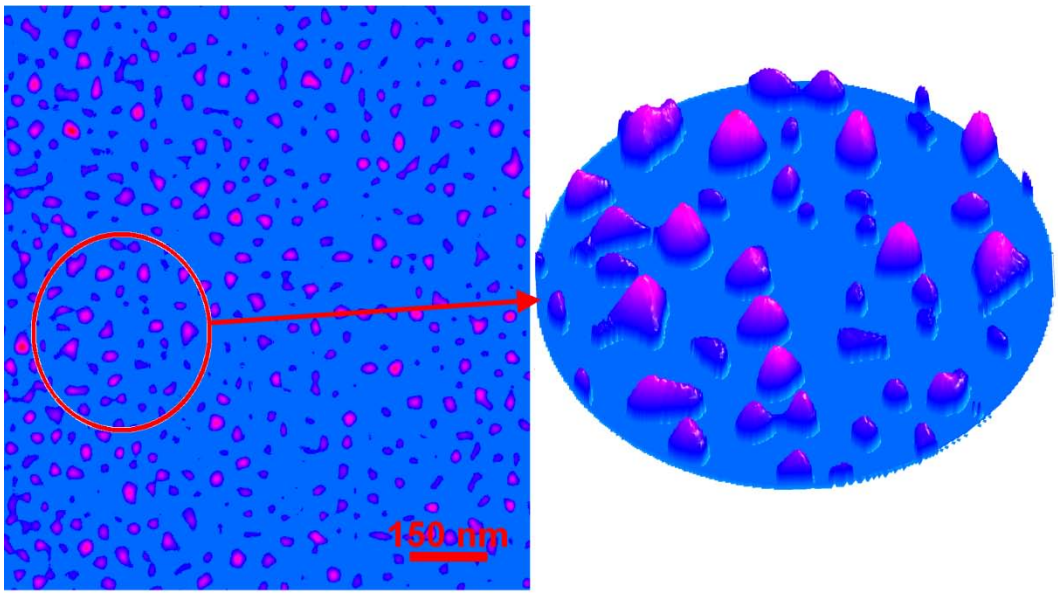


**Figure 4-6** AFM height image of PtNCs deposited via spin coating on $Si/SiO_2$ substrate.

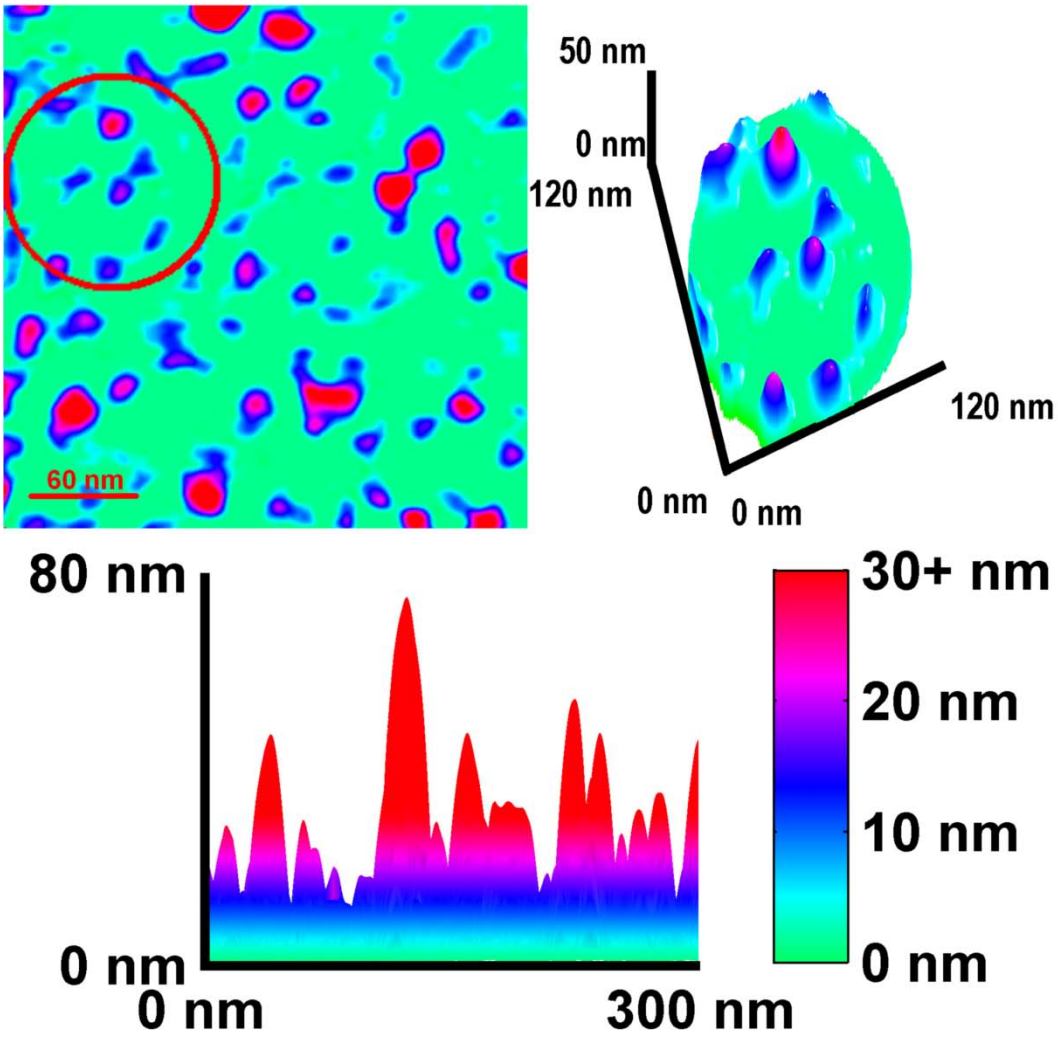


**Figure 4-7** Close-up view of AFM height image of PtNCs deposited via spin coating on Si/$SiO_2$ substrate.

Work function is an important parameter for materials used in the structure of the photovoltaic devices, because the order of the layers is defined according to work function to enable charge carriers hop between layers. Order of the layers is important for designing the fabrication process. In order to define the order of the deposition steps to arrange a proper band energy diagram for the charge carriers, the work function of the PtNCs is measured. The work function values for metallic materials, zero-bandgap, can

be measured by using thermionic emission method.[155-157] Thermionic electron emission is used as electron sources in a wide variety of applications, such as fluorescent lamps, cathode ray tubes, X-ray tubes, mass spectrometers, vacuum gauges, scanning electron microscopes and many scientific instruments. Currently, thermionic emission measurements require high operation temperature (>1000 °C) for practical measurements due to the low emission efficiency. Low-temperature and highly efficient thermionic emission not only improves, but also make it more easy to measure the work function.

Thermionic electron emission current can be described by the Richardson–Dushman[161, 162] equation with the Richardson's emission constant A ($A \cdot cm^{-2} \cdot K^{-2}$). The work function was calculated according to Richardson-Dushman equation,[161]

$$I_0 = AT^2 \exp\left(-\frac{\Phi}{K_B T}\right) \tag{4.1}$$

where $I_0$ is the zero field thermionic emission current, T is the absolute temperature, $\Phi$ is the work function of the cathode at absolute zero temperature, $K_B$ is the Boltzmann constant.

The "zero field thermionic emission current" $I_0$ can be calculated from the I-V curves according to the Schottky effect,[162]

$$I_a = I_0 \exp\left(-\frac{q\sqrt{qE/4\pi\varepsilon_0}}{K_B T}\right) \tag{4.2}$$

where $I_a$ is the thermionic emission current, q is the electron charge, E is the electric field on the thermionic cathode surface, and $\varepsilon_0$ is the vacuum dielectric constant. E can be substituted by $\alpha\sqrt{U_a + U_c}$. Here α is a constant determined by the geometry of electrode structures, $U_a$ is the anode voltage in volts, $U_c$ is the contact potential between the cathode and anode, which is usually below 1 V and can be neglected in the calculation.

Figure 4-8 shows representative results of emission current, i.e. anode current, as a function of anode voltage at several temperatures for forward bias. The measurement was done at different temperatures in the range of 600-to-650 K for anode voltage sweeping from 0-to-100 V. No emission current was observed for reverse bias. The emission current increased rapidly and saturated with increasing the anode voltage for the temperatures from 625 K to 650 K.

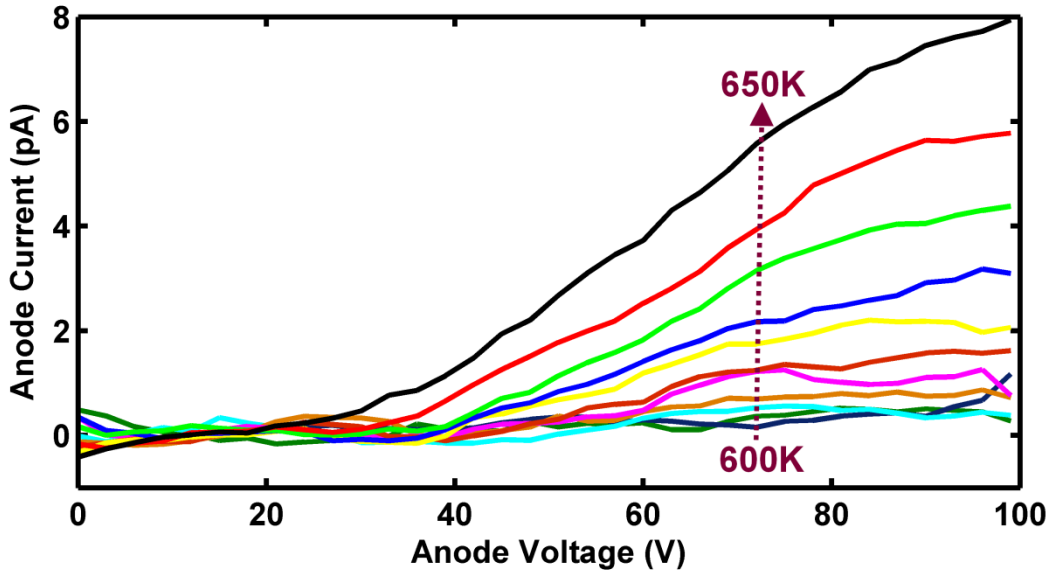


**Figure 4-8** Thermionic emission current as a function of forward bias at several temperatures.

The saturation emission current increased with increasing the temperature. Temperature dependence of saturation current at anode voltage = 99 V is shown in figure 4-9. As it can be seen from the figure, saturation current rapidly increased with increasing the temperature as expected.

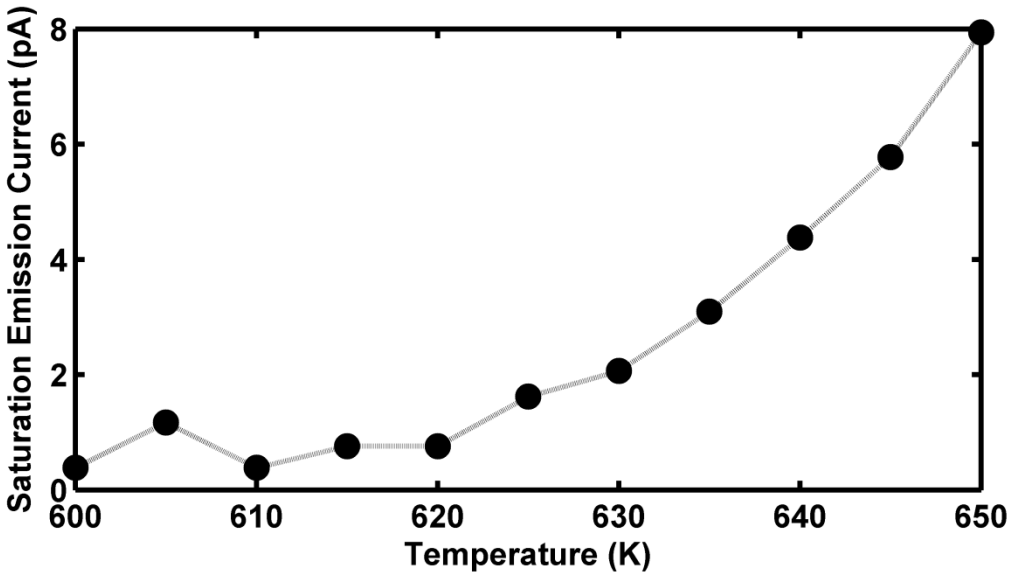


**Figure 4-9** Saturation emission current at anode voltage = 99 V as a function of the temperature.

The work function (Φ) for the PtNCs can be estimated from the relation between the saturation emission current density (J) and the temperature. The J divided $T^2$ ($J/T^2$) showed a straight line against the reciprocal temperature as shown in figure 4-10. Natural logarithm, $\ln(J/T^2)$, of this relation is calculated an given in figure 4-11 as the experimental $\ln(J/T^2)$ versus l000/T curves. The slope of the plot given in equation 4.3,[163] gives the work function which corresponds to Φ = 5.8 eV.

$$\Phi = -\frac{K_B}{q}\frac{d}{d(1000/T)}\left[\ln\left(J/T^2\right)\right] \qquad (4.3)$$

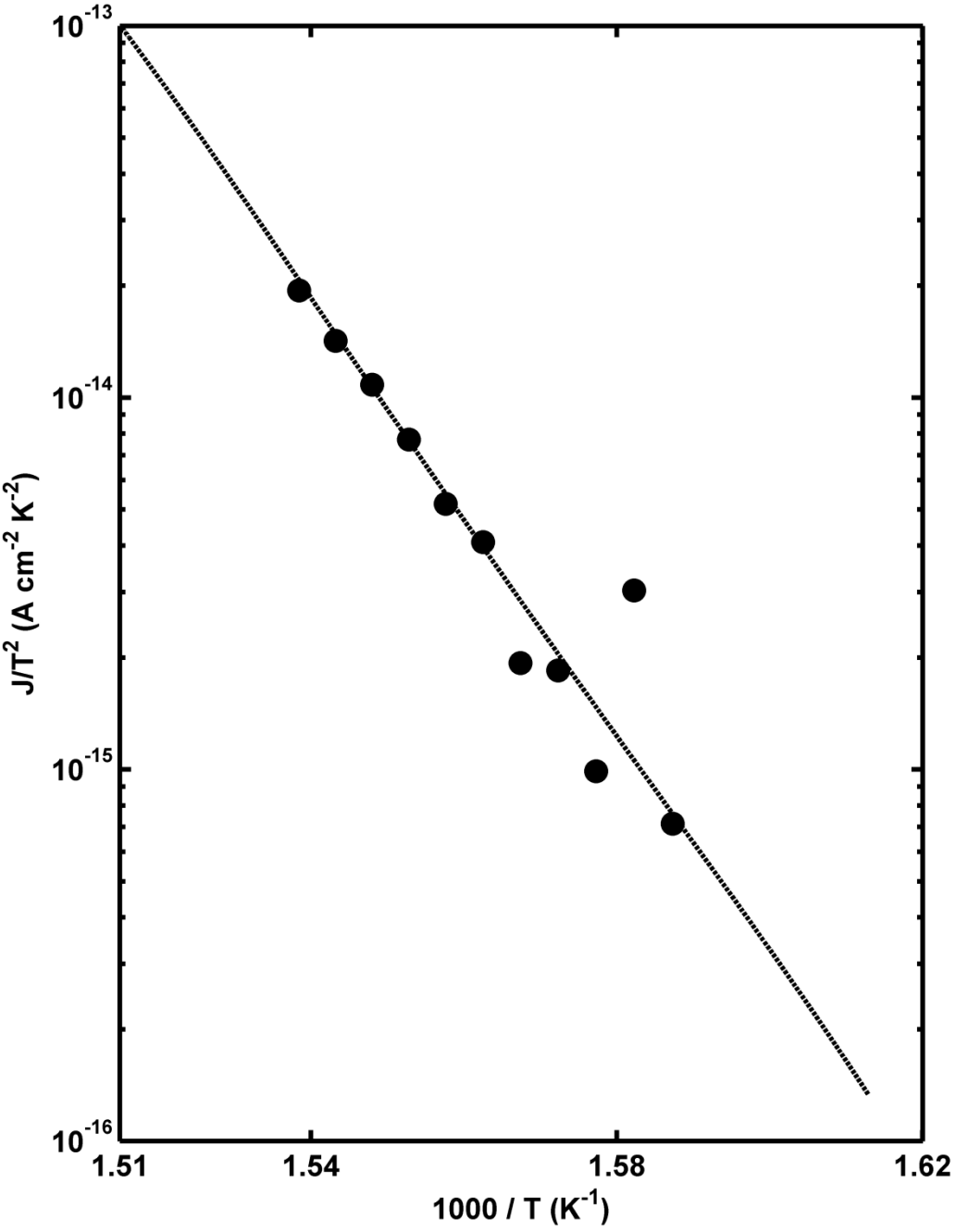


**Figure 4-10** Saturation emission current density divided $T^2$ ($J/T^2$) as a function of the reciprocal temperature.

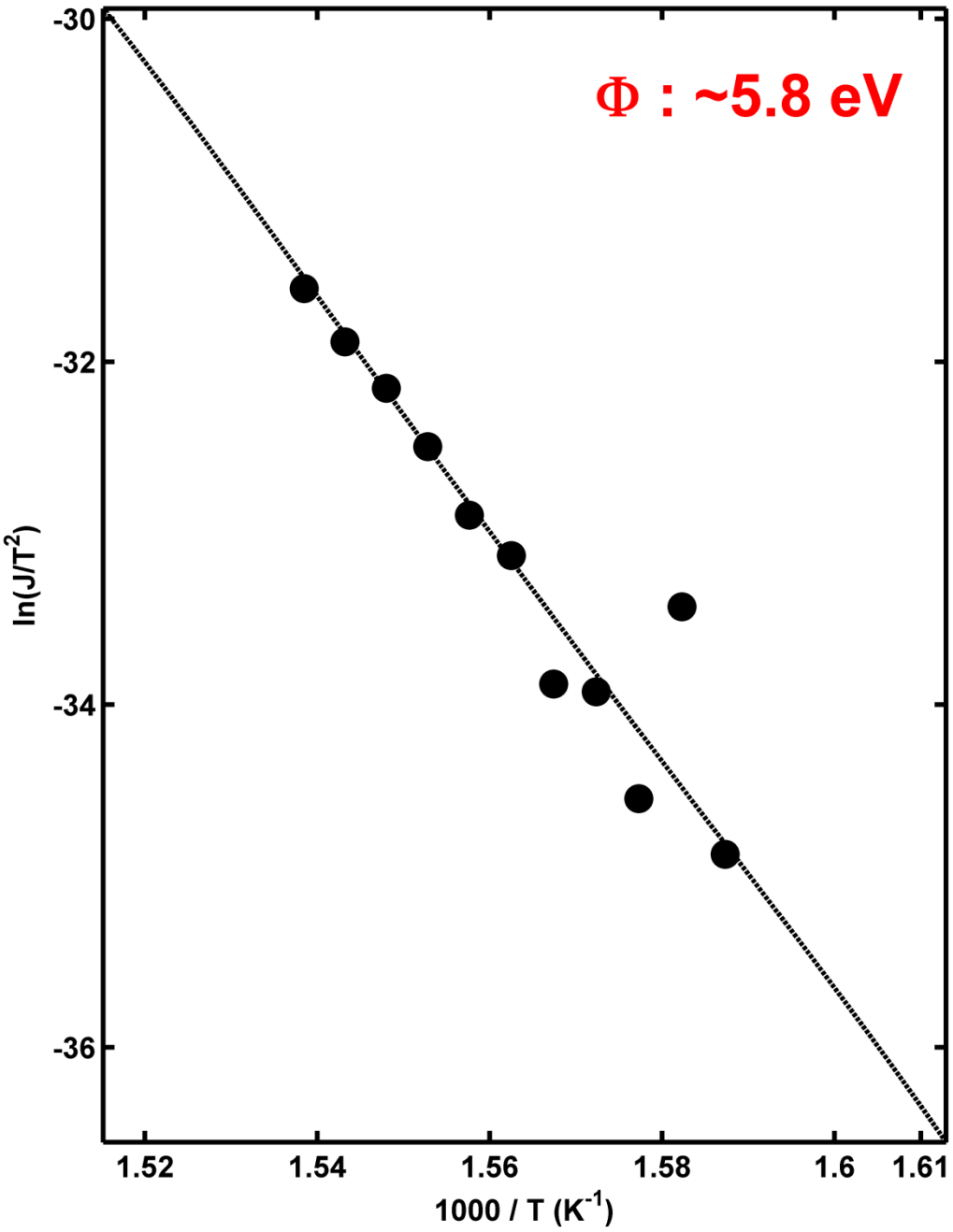


**Figure 4-11** The experimental natural logarithm of saturation current density divided by $T^2$, $\ln(J/T^2)$, as a function of the reciprocal temperature (1000/T).

The orders of the layers in the organic BHJ photovoltaic devices are then arranged according to this work function value. Since the work function of the PtNCs are 5.8 eV, the layers having PtNC in their composition should be placed between PEDOT:PSS and P3HT:PCBM due to allow the holes hop smoothly between layers. The corresponding band energy diagrams for the devices in which PtNCs are used as the surface plasmons are given in figure 4-12.

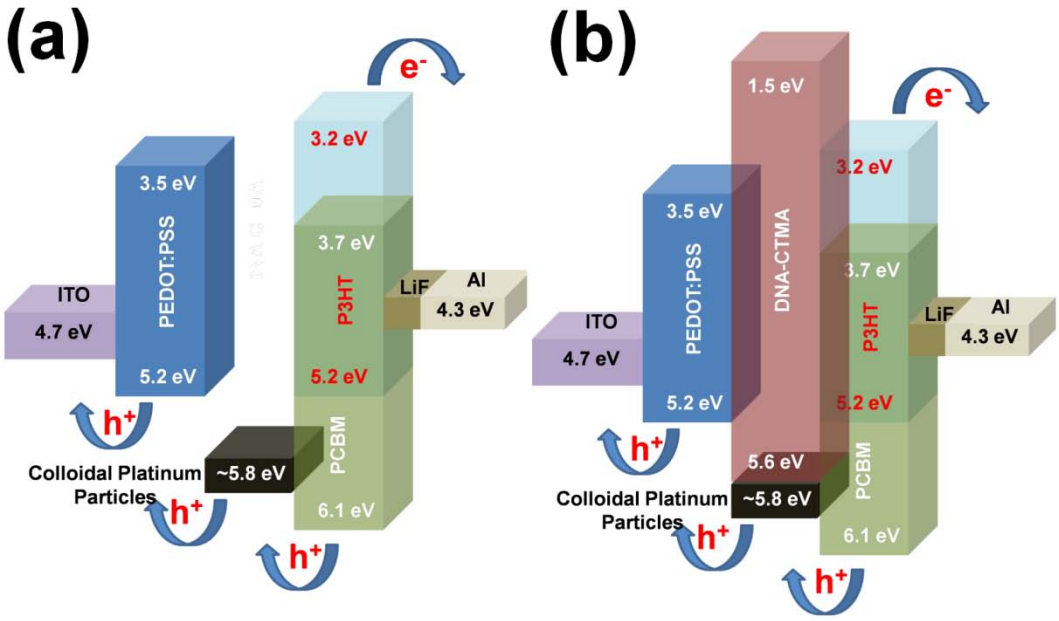


**Figure 4-22** Band energy diagrams of organic BHJ photovoltaic devices. (a) Sample with the PtNCs as the surface plasmons , (b) Sample with PtNC/DNA complex layer introduced between PEDOT:PSS and P3HT:PCBM layers as hole collecting and electron blocking layer.

After completing the structural designs, several devices having four different device structures which have been discussed above as control samples, samples with DNA complex introduced only, samples with PtNC layer introduced only and samples with PtNC/DNA complex introduced are fabricated for electrical and spectral

characterization and performance analysis of the devices. For the electrical characterization the devices have been tested under 1 sun illumination. The results for the current-voltage measurements are given in figure 4-13 as the current density as a function of applied voltage.

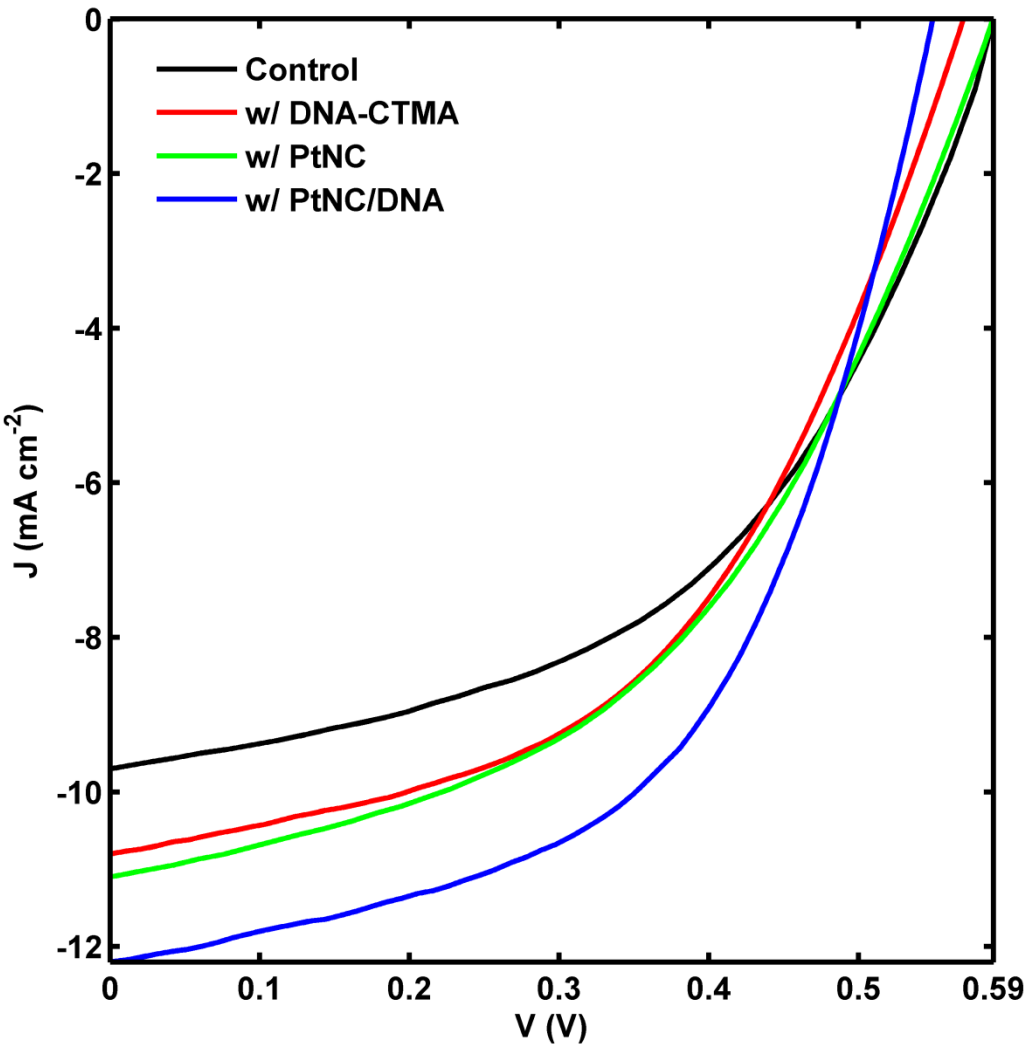


**Figure 4-33** Current density (J) – Applied voltage (V) characteristics of the organic BHJ photovoltaic devices, control sample and devices with DNA-CTMA layer, PtNC layer and PtNC/DNA layer introduced between PEDOT:PSS and P3HT:PCBM layers, tested under illumination having power of 1mW/mm2, i.e. 1sun or AM 1.5 G

As it can easily be seen form figure 4-13, a significant increase in the short-circuit current density, which stands for the photocurrent under zero bias voltage, for the devices having improvement layers introduced in the device structure. The electrical characterization parameters for the devices have been calculated as in chapter 2.4.5.2 and given in table 4-1.

**Table 4-1** Electrical characterization parameters for the organic BHJ photovoltaic devices having four different device structures.

| Device | $V_{oc}$ (V) | $J_{sc}$ (A/cm$^2$) | Power Conversion Efficiency [%] | Fill Factor [%] | $R_s$ ($\Omega$cm$^2$) |
|---|---|---|---|---|---|
| **Control** | 0.59 | -9.7 | 2.84 | 49.7 | 3.35 |
| **DNA-CTMA** | 0.57 | -10.8 | 3.03 | 49.2 | 2.85 |
| **PtNC** | 0.59 | -11.1 | 3.06 | 46.7 | 2.96 |
| **PtNC/DNA** | 0.55 | -12.2 | 3.59 | 53.5 | 2.53 |

In table 4-1, averages of the characterization parameters for the devices are given. Power conversion efficiency (PCE) of all of the fabricated devices having improvement layers show increase. DNA-CTMA layer with its band energy structure arrangement for electron blocking and hole collecting properties, increased the charge hopping efficiency because there is almost no increase in the photon absorption or light-harvesting efficiency of the devices due to this layer as it can be seen from figure 4-5. This unchanged absorbance spectra prove the improvement is only in charge hopping efficiency between layers. Additionally, from table 4-1, series resistance ($R_s$) of the device has also reduced due to increasing charge hopping efficiency. This device structure has 7% higher PCE compared to the control device structure.

The devices having PtNC surface plasmons shows great improvement in the photon absorption (Figure 4-5) matching with the range of plasmon extinction spectra (Figure 4-4). This improvement in the light-harvesting efficiency brings more charge carriers which results an 8% increase in the PCE of the device. Additionally, $R_s$ of this device is also reduced.

Combination of PtNCs and DNA-CTMA in the same device structure improves the device in both light-harvesting efficiency and charge hopping efficiency. For the light-harvesting efficiency, absorbance spectra of the devices having PtNC/DNA layer show great increase in the photon absorption. Figure 4-5 indicates that, comparison of PtNC only device absorbance and PtNC/DNA device absorbance are almost same, thereby, it can be said that the improvement of light-harvesting comes only from the PtNC surface plasmons. This improvement in the absorbance spectra also matches with the extinction spectra of the PtNCs given in figure 4-4. DNA-CTMA mixed with PtNCs causes additional improvement by improving the charge carrier hopping for the holes on the anode side and blocking the electrons diffusing to the anode electrode. As a result of this combination, $R_s$ of devices having this structure reduces 30% and PCE increases 26%.

For the spectral characterization of the devices, first, the photocurrent density spectra of the devices given in figure 4-14 are calculated by using the $J_{sc}$ values from which the short circuit dark current density was subtracted measured under illumination of 30 different wavelengths of light filtered by monochromatic band-pass filters.

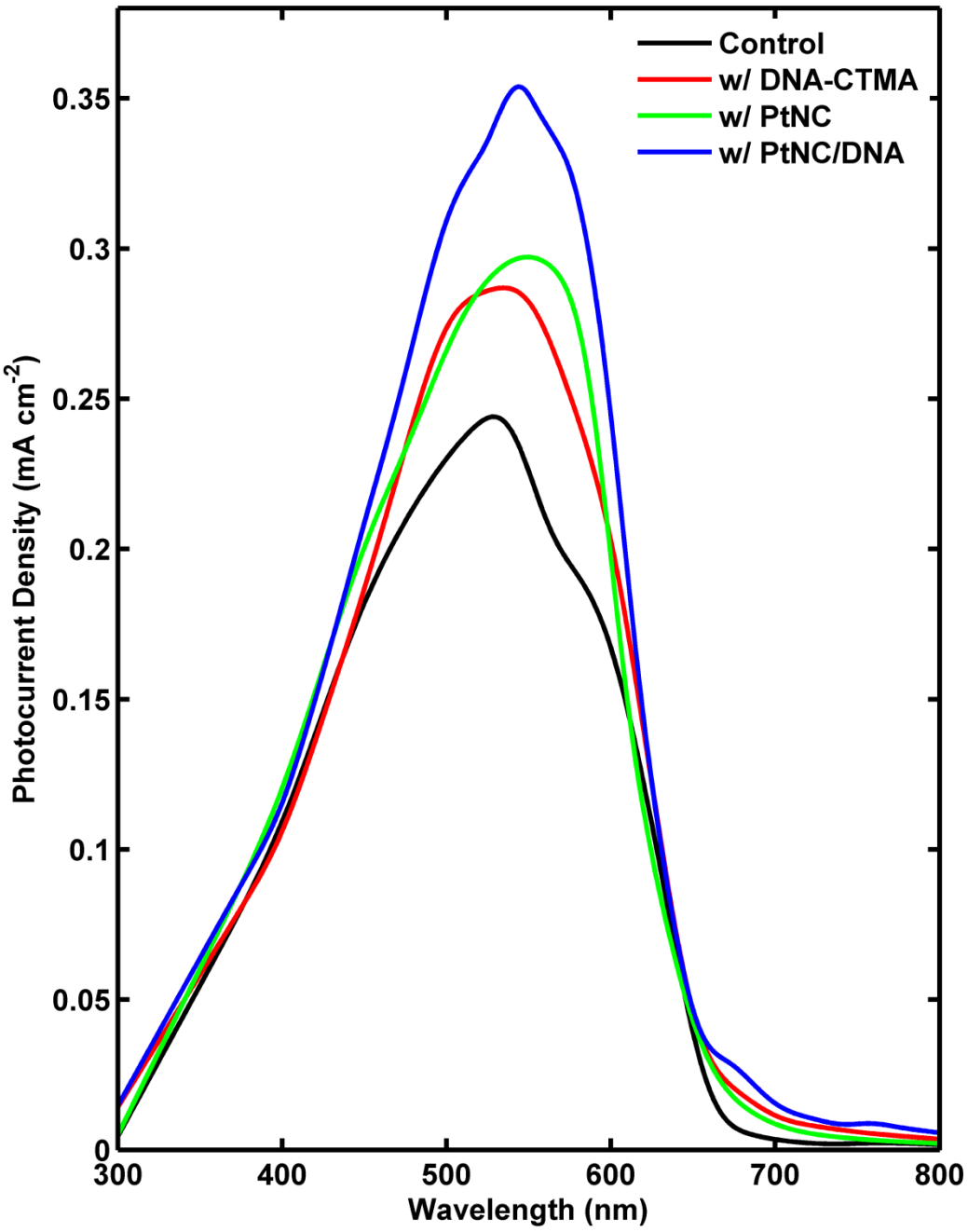


**Figure 4-44** Photocurrent density spectra of the devices as a function of wavelength measured under illumination of 30 different wavelengths of light filtered by monochromatic band-pass filters.

Although position of the peaks of the photocurrent density spectra of the devices match perfectly with the position of the peaks of the absorbance spectra of the devices, they show different behavior in magnitudes of the peaks. This difference comes from different methods of device improvement such as DNA-CTMA shows less absorption but higher charge carrier hopping efficiency improvement when it is compared to PtNC device. As a result, they have almost the same photocurrent density spectra. Besides these anecdotes on the devices, without any questions PtNC/DNA combination shows the highest performance.

Using the photocurrent density spectra and the solar simulator power irradiance spectra given in figure 3-2 other spectral characterizations such as EQE and IQE were calculated and given in figure 4-15 and 4-16 respectively.

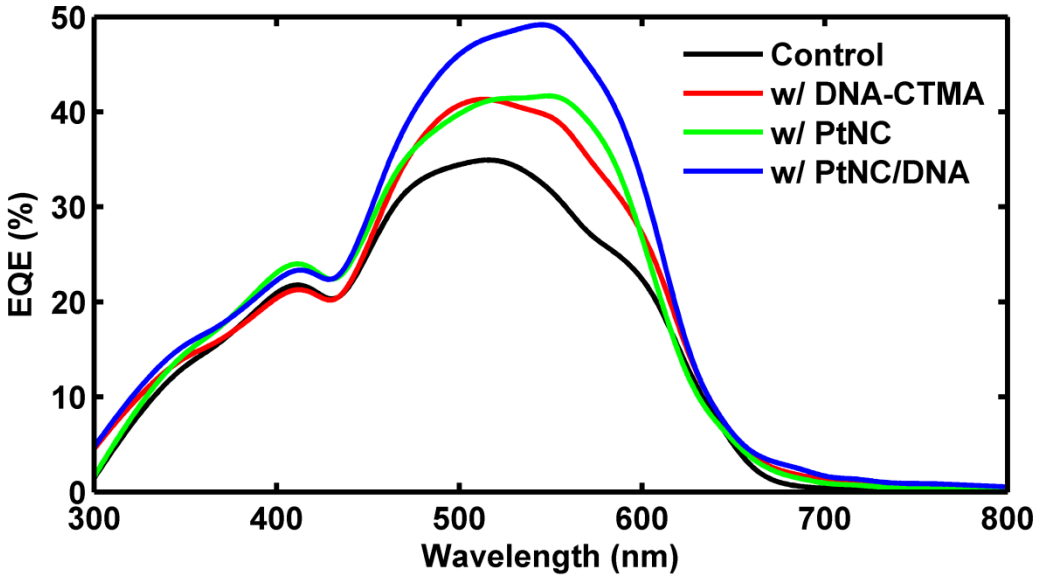


**Figure 4-55** EQE spectra of the devices as a function of wavelength measured under illumination of 30 different wavelengths of light filtered by monochromatic band-pass filters.

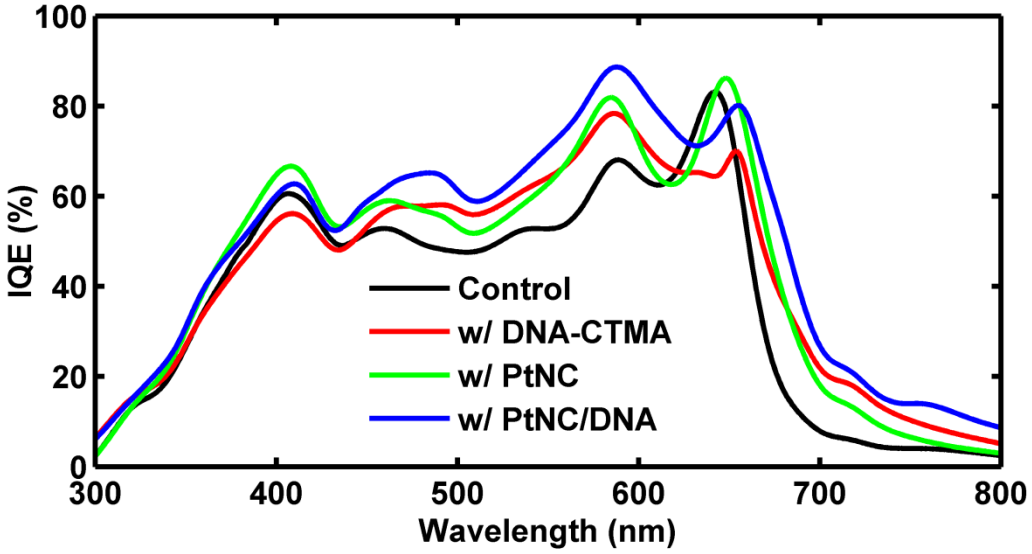


**Figure 4-66** IQE spectra of the devices as a function of wavelength measured under illumination of 30 different wavelengths of light filtered by monochromatic band-pass filters.

As it can be seen in figure 4-15 and 4-16, in PtNC/DNA devices, more excitons can dissociate and charges can reach to the anode and cathode electrodes without recombining. This results a higher increase in the rate of EQE spectra than that of absorbance spectra which is a proof of improvement in charge carrier hopping

### 4.4 Conclusion

As a summary, four different device structures with three different improvement layers for organic BHJ photovoltaic devices have been tested and characterized. All three of the new layers introduced into to device structure improves the performance of the devices as they compared with the very-well known P3HT:PCBM device structure. DNA-CTMA layer improved the device performance by improving the charge carrier hopping efficiency of the devices by arranging the band energy diagram in order to collect holes easily and block electrons diffusing to anode electrodes. PtNC layer

improved the device performance by increasing the light-harvesting efficiency of the devices by increasing the rate of photon absorption. This proves that the PtNCs can be used as surface plasmons in organic BHJ photovoltaic devices. Because peak their extinction spectra matches with the peak of absorbance of P3HT:PCBM. Combination of these two novel materials in the same device showed a significant improvement as a 26% increase in the PCE of the devices as they compared with the control samples.

## Chapter 5:

## Conclusion

In conclusion, the space charge region width of the Schottky barrier forms on the interface between aluminum and organic semiconductor polymer of organic bulkheterojunction photovoltaic devices based on poly(3-hexylthiophene) (P3HT): [6,6]-phenyl-$C_{61}$-butyric acid methyl ester (PCBM) blend, have been investigated according to reverse voltage bias over the device. Comparison of the developed mathematical models and experimental data measured under different incident light powers indicates a dependency of space charge region to the incident light power. The incident light power has an effect on the Schottky barriers of the organic bulk heterojunction photovoltaic devices by changing the width of the space charge regions. This change directly affects the reverse bias I-V curves by increasing the current values and the slope of the curves. The photodetection performance of the devices tends to increase with the increasing light power due to the increasing space charge region width. But under excessive incident light power; the space charge regions will merge, the devices will break down and work as ohmic devices.

Four different device structures with three different improvement layers for organic BHJ photovoltaic devices have been tested and characterized. All three of the new layers introduced into to device structure improves the performance of the devices as they compared with the very-well known P3HT:PCBM device structure. deoxyribonucleic acid complex layer improved the device performance by improving the

charge carrier hopping efficiency of the devices by arranging the band energy diagram in order to collect holes easily and block electrons diffusing to anode electrodes. Colloidal platinum nanoparticles layer improved the device performance by increasing the light-harvesting efficiency of the devices by increasing the rate of photon absorption. This proves that the Colloidal platinum nanoparticles can be used as surface plasmons in organic bulk heterojunction photovoltaic devices. Because peak their extinction spectra matches with the peak of absorbance of P3HT:PCBM. Combination of these two novel materials in the same device showed a significant improvement as a 26% increase in the power conversion efficiency of the devices as they compared with the control samples.

**Chapter 6:**

**References**


[1] E. Lorenzo, G. L. Araujo, A. Cuevas, M. A. Egido, J. C. Minano and R. Ziles, Solar Electricity: Engineering of Photovoltaic Systems. (Progensa, Madrid, Spain, 1994).

[2] United Nations, Human Development Report, 2011.

[3] U.S. Energy Information Administration, International Energy Outlook, DOE/EIA-0484(2010), Washington DC 2010.

[4] U.S. Energy Information Administration, International Energy Outlook, DOE/EIA-0484(2011), Washington DC 2011.

[5] H. J. Longwell, The Future of the Oil and Gas Industry, World Energy 5 (3), (2002)

[6] T. Conway and P. Tan, NOAA/ESRL www.esrl.noaa.gov/gmd/ccgg/trends/

[7] NASA, GISS Surface Temperature Analysis (GISTEMP), http://data.giss.nasa.gov/gistemp/

[8] European Wind Energy Association, Wind Energy The Facts: An Analysis of Wind Energy in the EU-25, 2007.

[9] V. Smil, General Energetics Energy in the Biosphere and Civilization, VIII ed. (John Wiley & Sons, New York, 1991).

[10] United Nations, World Energy Assesment Report: Energy and Challenge of Sustainability, New York 2003.

[11] 3TIER, Renewable Energy Resource Maps, http://www.3tier.com/en/support/resource-maps/

[12] M. B. Prince and M. Wolf, New developments in silicon photovoltaic devices, Journal of the British Institution of Radio Engineers 18 (10), 583-595595 (1958).

[13] N. S. Kang, B. K. Ju, T. W. Lee, D. H. Choi, J. M. Hong and J. W. Yu, Organic photovoltaic devices with a crosslinkable polymer interlayer, Solar Energy Materials and Solar Cells 95 (10), 2831-2836 (2011).

[14] H. M. Khlyap and V. I. Laptev, Recent Achievements in Nanostructured Photovoltaic Devices, Recent Patents on Nanotechnology 5 (2), 100-105 (2011).

[15] K. Fostiropoulos and M. Rusu, Engineering of hybrid interfaces in organic photovoltaic devices, Solar Energy Materials and Solar Cells 95 (6), 1489-1494 (2011).

[16] Y. Shang, Q. K. Li, L. Y. Meng, D. Wang and Z. G. Shuai, Computational characterization of organic photovoltaic devices, Theoretical Chemistry Accounts 129 (3-5), 291-301 (2011).

[17] R. S. Ohl and R. S. Ohl, Light-Sensitive Electric Device, United States, U. S. P. a. T. Office, Patent No. 2402662 (1946).

[18] K. A. Tsokos, Physics for the IB Diploma, V ed. (Cambridge University Press, Cambridge, 2008).

[19] H. I. Ringermacher, NDE: surfing the electromagnetic spectrum, AIP Conference Proceedings 1211, 29-4646 (2010).

[20] M. Bacci, Exploitation of the whole electromagnetic spectrum in art conservation studies, 2010 35th International Conference on Infrared, Millimeter, and Terahertz Waves (IRMMW-THz 2010), 4 pp.-4 pp.4 pp. (2010).

[21] P. J. Mohr, B. N. Taylor and D. B. Newell, CODATA recommended values of the fundamental physical constants: 2006, Reviews of Modern Physics 80 (2), 633 (2008).

[22] P. W. Hawkes, Advances in electronics and electron physics. (Academic Press, San Diego, 1989).

[23] P. Scherz, Practical electronics for inventors, 2nd ed. (McGraw-Hill, New York, 2007).

[24] A. B. Guvenc, E. Yengel, G. P. Wang, C. S. Ozkan and M. Ozkan, Effect of incident light power on Schottky barriers and I-V characteristics of organic bulk heterojunction photodiodes, Applied Physics Letters 96 (14) (2010).

[25] A. Smee, Elements of electro-biology,: or the voltaic mechanism of man; of electro-pathology, especially of the nervous system; and of electro-therapeutics. (Longman, Brown, Green & Longmans, London, 1849).

[26] C. W. Tucker, A study of photovoltaic cells, Journal of Physical Chemistry 31, 1357-1380 (1927).

[27] C. G. Fink and D. K. Alpern, Development of photovoltaic cells with discussion, Transactions of the American Electrochemical Society 58, 275-298298 (1930).

[28] R. T. Dufford, Photovoltaic effect with discussion, Transactions of the American Electrochemical Society 62, 359-368368 (1932).

[29] C. G. Fink and E. Adler, The photovoltaic effect with discussion, Transactions of the Electrochemical Society 79, 367-375375 (1940).

[30] R. K. Katiyar, A. Kumar, G. Morell, J. F. Scott and R. S. Katiyar, Photovoltaic effect in a wide-area semiconductor-ferroelectric device, Applied Physics Letters 99 (9) (2011).

[31] Nobelprize.org, The Nobel Prize in Physics 1921, http://www.nobelprize.org/nobel_prizes/physics/laureates/1921/

[32] J. Perlin, National Renewable Energy Laboratory (NREL), The Silicon Solar Cell Turns 50, BR-520-33947, 2004.

[33] L. Kazmerski, National Renewable Energy Laboratory (NREL), Research Cell Efficiency Plot for Various Photovoltaic Technologies 1976-2011, 2011.

[34] M. A. Green, Third generation photovoltaics: solar cells for 2020 and beyond, Physica E-Low-Dimensional Systems & Nanostructures 14 (1-2), 65-70 (2002).

[35] C. J. Keavney and M. B. Spitzer, INDIUM-PHOSPHIDE SOLAR-CELLS MADE BY ION-IMPLANTATION, Applied Physics Letters 52 (17), 1439-1440 (1988).

[36] D. E. Carlson and C. R. Wronski, AMORPHOUS SILICON SOLAR-CELL, Applied Physics Letters 28 (11), 671-673 (1976).

[37] Y. Ohtake, K. Kushiya, M. Ichikawa, A. Yamada and M. Konagai, Polycrystalline Cu(InGa)Se-2 thin-film solar cells with ZnSe buffer layers, Japanese Journal of Applied Physics Part 1-Regular Papers Short Notes & Review Papers 34 (11), 5949-5955 (1995).

[38] K. D. Dobson, I. Visoly-Fisher, G. Hodes and D. Cahen, Stability of CdTe/CdS thin-film solar cells, Solar Energy Materials and Solar Cells 62 (3), 295-325 (2000).

[39] A. Luque and S. Hegedus, Handbook of photovoltaic science and engineering. (Wiley, Hoboken, NJ, 2003).

[40] A. Luque and S. Hegedus, Handbook of photovoltaic science and engineering, 2nd ed. (Wiley, Chichester, West Sussex, U.K. ; Hoboken, N.J., 2010).

[41] National Renewable Energy Laboratory (NREL), NREL Solar Cell Sets World Efficiency Record at 40.8 Percent, NR-2708, 2008.

[42] G. Li, V. Shrotriya, J. S. Huang, Y. Yao, T. Moriarty, K. Emery and Y. Yang, High-efficiency solution processable polymer photovoltaic cells by self-organization of polymer blends, Nature Materials 4 (11), 864-868 (2005).

[43] M. A. Green, K. Emery, D. L. King, Y. Hisikawa and W. Warta, Solar cell efficiency tables (Version 27), Progress in Photovoltaics 14 (1), 45-51 (2006).

[44] I. S. Yahia, F. Yakuphanoglu and O. A. Azim, Unusual photocapacitance properties of a mono-crystalline silicon solar cell for optoelectronic applications, Solar Energy Materials and Solar Cells 95 (9), 2598-2605 (2011).

[45] W. T. Hsiao, S. F. Tseng, K. C. Huang, Y. H. Wang and M. F. Chen, Pulsed Nd:YAG laser treatment of monocrystalline silicon substrate, International Journal of Advanced Manufacturing Technology 56 (1-4), 223-231 (2011).

[46] R. Guerrero-Lemus, A. Montesdeoca-Santana, B. Gonzalez-Diaz, B. Diaz-Herrera, J. J. Velazquez, C. Hernandez-Rodriguez and E. Jimenez-Rodriguez, Photoluminescence of monocrystalline and stain-etched porous silicon doped with high temperature annealed europium, Journal of Physics D-Applied Physics 44 (33) (2011).

[47] F. Schindler, J. Geilker, W. Kwapil, W. Warta and M. C. Schubert, Hall mobility in multicrystalline silicon, Journal of Applied Physics 110 (4) (2011).

[48] C. C. Kuo, A novel optical diagnostic technique for analyzing the recrystallization characteristics of polycrystalline silicon thin films following frontside and backside excimer laser irradiation, Optics and Lasers in Engineering 49 (11), 1281-1288 (2011).

[49] I. S. Kang, Y. S. Kim, H. S. Seo, C. W. Ahn, J. M. Yang and W. J. Hwang, Hysteresis suppression improvement of polycrystalline silicon thin-film transistors by two-step hydrogenation, Current Applied Physics 11 (6), 1319-1321 (2011).

[50] I. Laboriante, M. Fisch, A. Payamipour, F. Liu, C. Carraro and R. Maboudian, Morphological, Electrical, and Chemical Changes in Cyclically Contacting Polycrystalline Silicon Surfaces Coated with Perfluoroalkylsilane Self-Assembled Monolayer, Tribology Letters 44 (1), 13-17 (2011).

[51] D. Kim, Deposition of polycrystalline Si thin films on glass substrates by direct negative Si ion beam deposition, Nuclear Instruments & Methods in Physics Research Section B-Beam Interactions with Materials and Atoms 269 (18), 2017-2019 (2011).

[52] L. Dong Nyung, Solid-phase crystallization of amorphous Si films on glass and Si wafer, Journal of the Physics and Chemistry of Solids 72 (11), 1330-13331333 (2011).

[53] D. P. Zhou, M. X. Wang and S. D. Zhang, Degradation of Amorphous Silicon Thin Film Transistors Under Negative Gate Bias Stress, Ieee Transactions on Electron Devices 58 (10), 3422-3427 (2011).

[54] Z. Dapeng, W. Mingxiang and Z. Shengdong, Degradation of Amorphous Silicon Thin Film Transistors Under Negative Gate Bias Stress, IEEE Transactions on Electron Devices 58 (10), 3422-34273427 (2011).

[55] T. Sumitomo, H. Huang, L. B. Zhou and J. Shimizu, Nanogrinding of multi-layered thin film amorphous Si solar panels, International Journal of Machine Tools & Manufacture 51 (10-11), 797-805 (2011).

[56] C. Kraft, A. Bromel, S. Schonherr, M. Hadrich, U. Reislohner, P. Schley, G. Gobsch, R. Goldhahn, W. Wesch and H. Metzner, Phosphorus implanted cadmium telluride solar cells, Thin Solid Films 519 (21), 7153-7155 (2011).

[57] M. Hadrich, C. Heisler, U. Reislohner, C. Kraft and H. Metzner, Back contact formation in thin cadmium telluride solar cells, Thin Solid Films 519 (21), 7156-7159 (2011).

[58] M. T. Khan, A. Kaur, S. K. Dhawan and S. Chand, In-Situ growth of cadmium telluride nanocrystals in poly(3-hexylthiophene) matrix for photovoltaic application, Journal of Applied Physics 110 (4) (2011).

[59] N. H. Kim, J. S. Park and W. S. Lee, Effective Ag Doping by He-Ne Laser Exposure to Improve the Electrical and the Optical Properties of CdTe Thin Films for Heterostructured Thin Film Solar Cells, Journal of the Korean Physical Society 59 (3), 2286-2290 (2011).

[60] L. Dingyuan, S. Baosheng, D. Yuepeng, B. J. Stanbery and L. Eldada, Copper Indium Gallium Selenide photovoltaic modules manufactured by reactive transfer, 2010 35th IEEE Photovoltaic Specialists Conference (PVSC), 000175-000178000178 (2010).

[61] K. Zweibel, Baseline evaluation of thin-film amorphous silicon, copper indium diselenide, and cadmium telluride for the 21st Century, Photovoltaics for the 21st Century. Proceedings of the International Symposium. (Electrochem. Soc. Proceedings Vol.99-11), 3-1515 (1999).

[62] R. K. Ahrenkiel, D. H. Levi, S. Johnston, W. Song, D. Mao and A. Fischer, Photoconductive lifetime of CdS used in thin-film solar cells, Conference Record of the Twenty Sixth IEEE Photovoltaic Specialists Conference - 1997 (Cat. No.97CB36026), 535-538538 (1997).

[63] W. Palz and R. Van Overstraeten, Progress of photovoltaic solar energy development in Europe, Clean and Safe Energy Forever. Proceedings of the 1989 Congress of the International Solar Energy Society, 78-87 vol.187 vol.181 (1990).

[64] G. A. Landis, S. G. Bailey and D. J. Flood, Advances In Thin-Film Solar-Cells for Light Weight Space Photovoltaic Power, Space Power 8 (1-2), 31-50 (1989).

[65] M. Z. Jacobson, Review of solutions to global warming, air pollution, and energy security, Energy & Environmental Science 2 (2), 148-173 (2009).

[66] J. S. Liu, C. H. Kuan, S. C. Cha, W. L. Chuang, G. J. Gau and J. Y. Jeng, Photovoltaic technology development: A perspective from patent growth analysis, Solar Energy Materials and Solar Cells 95 (11), 3130-3136 (2011).

[67] Q. Cao, O. Gunawan, M. Copel, K. B. Reuter, S. J. Chey, V. R. Deline and D. B. Mitzi, Defects in Cu(In,Ga)Se(2) Chalcopyrite Semiconductors: A Comparative Study of Material Properties, Defect States, and Photovoltaic Performance, Advanced Energy Materials 1 (5), 845-853 (2011).

[68] F. Alharbi, J. D. Bass, A. Salhi, A. Alyamani, H. C. Kim and R. D. Miller, Abundant non-toxic materials for thin film solar cells: Alternative to conventional materials, Renewable Energy 36 (10), 2753-2758 (2011).

[69] A. Bosio, A. Romeo, D. Menossi, S. Mazzamuto and N. Romeo, Review: The second-generation of CdTe and CuInGaSe(2) thin film PV modules, Crystal Research and Technology 46 (8), 857-864 (2011).

[70] T. Zhuo, Z. Bin, S. Ping, J. Shenghui, J. Peng, W. Xianyou and T. Songting, Low-cost quasi-solid-state dye-sensitized solar cells based on a metal-free organic dye and a carbon aerogel counter electrode, Journal of Materials Science 46 (23), 7482-74887488 (2011).

[71] R. Mi Sun and J. Jin, Enhanced efficiency of organic photovoltaic cells using solution-processed metal oxide as an anode buffer layer, Solar Energy Materials and Solar Cells 95 (11), 3015-30203020 (2011).

[72] Z. L. Yuan, J. S. Yu, N. N. Wang and Y. D. Jiang, Well-aligned ZnO nanorod arrays from diameter-controlled growth and their application in inverted polymer solar cell, Journal of Materials Science-Materials in Electronics 22 (11), 1730-1735 (2011).

[73] J. A. Mikroyannidis, D. V. Tsagkournos, P. Balraju and G. D. Sharma, Efficient bulk heterojunction solar cells using an alternating phenylenevinylene copolymer with dithenyl(thienothiadiazole) segments as donor and PCBM or modified PCBM as acceptor, Solar Energy Materials and Solar Cells 95 (11), 3025-3035 (2011).

[74] S. D. Yambem, K. S. Liao and S. A. Curran, Flexible Ag electrode for use in organic photovoltaics, Solar Energy Materials and Solar Cells 95 (11), 3060-3064 (2011).

[75] H. C. Li, K. K. Rao, J. Y. Jeng, Y. J. Hsiao, T. F. Guo, Y. R. Jeng and T. C. Wen, Nano-scale mechanical properties of polymer/fullerene bulk hetero-junction films and their influence on photovoltaic cells, Solar Energy Materials and Solar Cells 95 (11), 2976-2980 (2011).

[76] S. H. Hong, Y. S. Kim, W. Lee, Y. H. Kim, J. Y. Song, J. S. Jang, J. H. Park, S. H. Choi and K. J. Kim, Active doping of B in silicon nanostructures and development of a Si quantum dot solar cell, Nanotechnology 22 (42) (2011).

[77] A. Sugunan, Y. C. Zhao, S. Mitra, L. Dong, S. H. Li, S. Popov, S. Marcinkevicius, M. S. Toprak and M. Muhammed, Synthesis of tetrahedral quasi-type-II CdSe-CdS core-shell quantum dots, Nanotechnology 22 (42) (2011).

[78] H. Seung Hui, K. Yong Sung, L. Woo, K. Young Heon, S. Jae Yong, J. Jong Shik, P. Jae Hee, C. Suk-Ho and K. Kyung Joong, Active Doping of b in Silicon Nanostructures and Development of a si Quantum dot Solar cell, Nanotechnology 22 (42), 425203 (425206 pp.)-425203 (425206 pp.)425203 (425206 pp.) (2011).

[79] J. Tang, K. W. Kemp, S. Hoogland, K. S. Jeong, H. Liu, L. Levina, M. Furukawa, X. H. Wang, R. Debnath, D. K. Cha, K. W. Chou, A. Fischer, A. Amassian, J. B. Asbury and E. H. Sargent, Colloidal-quantum-dot photovoltaics using atomic-ligand passivation, Nature Materials 10 (10), 765-771 (2011).

[80] D. S. Kim, A. M. Gabor and A. Rohatgi, String ribbon silicon solar cells with 17.8 % efficiency, Journal of the Korean Physical Society 47 (1), 157-162 (2005).

[81] A. Rohatgi, V. Yelundur, J. W. Jeong, D. S. Kim and A. M. Gabor, Implementation of rapid thermal processing to achieve greater than 15% efficient screen-printed ribbon silicon solar cells, Proceedings of 3rd World Conference on Photovoltaic Energy Conversion (IEEE Cat. No.03CH37497), 1352-1355 Vol.1325 Vol.1352 (2003).

[82] V. Yelundur, A. Rohatgi, J. W. Jeong and J. I. Hanoka, Improved String Ribbon silicon solar cell performance by rapid thermal firing of screen-printed contacts, Ieee Transactions on Electron Devices 49 (8), 1405-1410 (2002).

[83] M. Y. Feteha and G. M. Eldallal, The effects of temperature and light concentration on the GaInP/GaAs multijunction solar cell's performance, Renewable Energy 28 (7), 1097-1104 (2003).

[84] J. M. Olson, A. Kibbler and T. Gessert, GaInP/GaAs Multijunction Solar-Cells, Solar Cells 21, 450-451 (1987).

[85] B. J. Yan, G. Z. Yue, L. Sivec, J. Yang, S. Guha and C. S. Jiang, Innovative dual function nc-SiO(x):H layer leading to a > 16% efficient multi-junction thin-film silicon solar cell, Applied Physics Letters 99 (11) (2011).

[86] Y. A. Akimov and W. S. Koh, Tolerance study of nanoparticle enhancement for thin-film silicon solar cells, Applied Physics Letters 99 (6) (2011).

[87] S. Fernandez, O. de Abril, F. B. Naranjo and J. J. Gandia, High quality textured ZnO:Al surfaces obtained by a two-step wet-chemical etching method for applications in thin film silicon solar cells, Solar Energy Materials and Solar Cells 95 (8), 2281-2286 (2011).

[88] M. Despeisse, C. Battaglia, M. Boccard, G. Bugnon, M. Charriere, P. Cuony, S. Hanni, L. Lofgren, F. Meillaud, G. Parascandolo, T. Soderstrom and C. Ballif, Optimization of thin film silicon solar cells on highly textured substrates, Physica Status Solidi a-Applications and Materials Science 208 (8), 1863-1868 (2011).

[89] W. J. Yang, H. C. Yu, J. P. Tang, Y. B. Su, Q. Wan and Y. G. Wang, Omnidirectional light absorption in thin film silicon solar cell with dual anti-reflection coatings, Solar Energy 85 (10), 2551-2559 (2011).

[90] Y. Wenji, Y. Hongchun, T. Jianping, S. Yingbing, W. Qing and W. Yanguo, Omnidirectional light absorption in thin film silicon solar cell with dual anti-reflection coatings, Solar Energy 85 (10), 2551-25592559 (2011).

[91] J. M. Pearce, N. Podraza, R. W. Collins, M. M. Al-Jassim, K. M. Jones, J. Deng and C. R. Wronski, Optimization of open circuit voltage in amorphous silicon solar cells with mixed-phase (amorphous+nanocrystalline) p-journal article contacts of low nanocrystalline content. (AIP, 2007).

[92] P. Sanchez, O. Lorenzo, A. Menendez, J. L. Menendez, D. Gomez, R. Pereiro and B. Fernandez, Characterization of Doped Amorphous Silicon Thin Films through the Investigation of Dopant Elements by Glow Discharge Spectrometry. A Correlation of Conductivity and Bandgap Energy Measurements, International Journal of Molecular Sciences 12 (4), 2200-2215 (2011).

[93] C. K. Chiang, C. R. Fincher, Y. W. Park, A. J. Heeger, H. Shirakawa, E. J. Louis, S. C. Gau and A. G. Macdiarmid, Electrical-Conductivity in Doped Polyacetylene, Physical Review Letters 39 (17), 1098-1101 (1977).

[94] J. H. Burroughes, D. D. C. Bradley, A. R. Brown, R. N. Marks, K. Mackay, R. H. Friend, P. L. Burns and A. B. Holmes, Light-Emitting-Diodes Based on Conjugated Polymers, Nature 347 (6293), 539-541 (1990).

[95] R. H. Friend, R. W. Gymer, A. B. Holmes, J. H. Burroughes, R. N. Marks, C. Taliani, D. D. C. Bradley, D. A. Dos Santos, J. L. Bredas, M. Logdlund and W. R. Salaneck, Electroluminescence in conjugated polymers, Nature 397 (6715), 121-128 (1999).

[96] N. S. Sariciftci, D. Braun, C. Zhang, V. I. Srdanov, A. J. Heeger, G. Stucky and F. Wudl, Semiconducting Polymer-Buckminsterfullerene Heterojunctions - Diodes, Photodiodes, and Photovoltaic Cells, Applied Physics Letters 62 (6), 585-587 (1993).

[97] G. Yu, J. Gao, J. C. Hummelen, F. Wudl and A. J. Heeger, Polymer Photovoltaic Cells - Enhanced Efficiencies Via a Network of Internal Donor-Acceptor Heterojunctions, Science 270 (5243), 1789-1791 (1995).

[98] R. Hoffmann, C. Janiak and C. Kollmar, A Chemical Approach to the Orbitals of Organic Polymers, Macromolecules 24 (13), 3725-3746 (1991).

[99] M. Granstrom, K. Petritsch, A. C. Arias, A. Lux, M. R. Andersson and R. H. Friend, Laminated fabrication of polymeric photovoltaic diodes, Nature 395 (6699), 257-260 (1998).

[100] S. E. Shaheen, C. J. Brabec, N. S. Sariciftci, F. Padinger, T. Fromherz and J. C. Hummelen, 2.5% efficient organic plastic solar cells, Applied Physics Letters 78 (6), 841-843 (2001).

[101] P. Schilinsky, C. Waldauf and C. J. Brabec, Recombination and loss analysis in polythiophene based bulk heterojunction photodetectors, Applied Physics Letters 81 (20), 3885-3887 (2002).

[102] F. Padinger, R. S. Rittberger and N. S. Sariciftci, Effects of postproduction treatment on plastic solar cells, Advanced Functional Materials 13 (1), 85-88 (2003).

[103] Y. Y. Liang, Z. Xu, J. B. Xia, S. T. Tsai, Y. Wu, G. Li, C. Ray and L. P. Yu, For the Bright Future-Bulk Heterojunction Polymer Solar Cells with Power Conversion Efficiency of 7.4%, Advanced Materials 22 (20), E135-+ (2010).

[104] A. J. Steckl, DNA - a new material for photonics?, Nature Photonics 1 (1), 3-5 (2007).

[105] S. Chaudhary, H. W. Lu, A. M. Muller, C. J. Bardeen and M. Ozkan, Hierarchical placement and associated optoelectronic impact of carbon nanotubes in polymer-fullerene solar cells, Nano Letters 7 (7), 1973-1979 (2007).

[106] H. W. Lu, S. Chaudhary, A. M. Muller, C. J. Bardeen and M. Ozkan, Effects of mild plasma exposure on the active-layer in polythiophene: Fullerene bulk-heterojunction solar cells, Journal of Nanoelectronics and Optoelectronics 2 (3), 282-286 (2007).

[107] C. J. Brabec, S. E. Shaheen, C. Winder, N. S. Sariciftci and P. Denk, Effect of LiF/metal electrodes on the performance of plastic solar cells, Applied Physics Letters 80 (7), 1288-1290 (2002).

[108] V. Shrotriya, G. Li, Y. Yao, T. Moriarty, K. Emery and Y. Yang, Accurate measurement and characterization of organic solar cells, Advanced Functional Materials 16 (15), 2016-2023 (2006).

[109] C. J. Brabec, A. Cravino, D. Meissner, N. S. Sariciftci, T. Fromherz, M. T. Rispens, L. Sanchez and J. C. Hummelen, Origin of the open circuit voltage of plastic solar cells, Advanced Functional Materials 11 (5), 374-380 (2001).

[110] C. J. Brabec, A. Cravino, D. Meissner, N. S. Sariciftci, M. T. Rispens, L. Sanchez, J. C. Hummelen and T. Fromherz, The influence of materials work function on the open circuit voltage of plastic solar cells, Thin Solid Films 403, 368-372 (2002).

[111] M. C. Scharber, D. Wuhlbacher, M. Koppe, P. Denk, C. Waldauf, A. J. Heeger and C. L. Brabec, Design rules for donors in bulk-heterojunction solar cells - Towards 10 % energy-conversion efficiency, Advanced Materials 18 (6), 789-+ (2006).

[112] G. Dennler, C. Lungenschmied, H. Neugebauer, N. S. Sariciftci and A. Labouret, Flexible, conjugated polymer-fullerene-based bulk-heterojunction solar cells: Basics, encapsulation, and integration, Journal of Materials Research 20 (12), 3224-3233 (2005).

[113] G. Dennler and N. S. Sariciftci, Flexible conjugated polymer-based plastic solar cells: From basics to applications, Proceedings of the Ieee 93 (8), 1429-1439 (2005).

[114] J. Rostalski and D. Meissner, Photocurrent spectroscopy for the investigation of charge carrier generation and transport mechanisms in organic p/n-junction solar cells, Solar Energy Materials and Solar Cells 63 (1), 37-47 (2000).

[115] V. N. Singh and R. P. Singh, A METHOD FOR THE MEASUREMENT OF SOLAR-CELL SERIES RESISTANCE, Journal of Physics D-Applied Physics 16 (10), 1823-1825 (1983).

[116] S. F. Tedde, J. Kern, T. Sterzl, J. Furst, P. Lugli and O. Hayden, Fully Spray Coated Organic Photodiodes, Nano Letters 9 (3), 980-983 (2009).

[117] E. S. Zaus, S. Tedde, T. Rauch, J. Fuerst and G. H. Doehler, Design of highly transparent organic photodiodes, Ieee Transactions on Electron Devices 55 (2), 681-684 (2008).

[118] Y. Yao, H. Y. Chen, J. S. Huang and Y. Yang, Low voltage and fast speed all-polymeric optocouplers, Applied Physics Letters 90 (5) (2007).

[119] L. S. Roman, M. R. Andersson, T. Yohannes and O. Inganas, Photodiode performance and nanostructure of polythiophene/C-60 blends, Advanced Materials 9 (15), 1164-& (1997).

[120] E. Kraker, A. Haase, B. Lamprecht, G. Jakopic, C. Konrad and S. Kostler, Integrated organic electronic based optochemical sensors using polarization filters, Applied Physics Letters 92 (3), 3 (2008).

[121] T. N. Ng, W. S. Wong, M. L. Chabinyc, S. Sambandan and R. A. Street, Flexible image sensor array with bulk heterojunction organic photodiode, Applied Physics Letters 92 (21), - (2008).

[122] N. A. Stathopoulos, L. C. Palilis, M. Vasilopoulou, A. Botsialas, P. Falaras and P. Argitis, All-organic optocouplers based on polymer light-emitting diodes and photodetectors, Physica Status Solidi a-Applications and Materials Science 205 (11), 2522-2525 (2008).

[123] J. Petrovic, P. Matavulj, D. F. Qi, D. K. Chambers and S. Selmic, A model for the current-voltage characteristics of ITO/PEDOT : PSS/MEH-PPV/Al photodetectors, Ieee Photonics Technology Letters 20 (5-8), 348-350 (2008).

[124] B. Pradhan, A. K. Sharma and A. K. Ray, A simple hybrid inorganic-polymer photodiode, Journal of Physics D-Applied Physics 42 (16) (2009).

[125] C. J. Novotny, E. T. Yu and P. K. L. Yu, InP nanowire/polymer hybrid photodiode, Nano Letters 8 (3), 775-779 (2008).

[126] P. Peumans, A. Yakimov and S. R. Forrest, Small molecular weight organic thin-film photodetectors and solar cells, Journal of Applied Physics 93 (7), 3693-3723 (2003).

[127] M. S. A. Abdou, F. P. Orfino, Y. Son and S. Holdcroft, Interaction of oxygen with conjugated polymers: Charge transfer complex formation with poly(3-alkylthiophenes), Journal of the American Chemical Society 119 (19), 4518-4524 (1997).

[128] M. Glatthaar, M. Riede, N. Keegan, K. Sylvester-Hvid, B. Zimmermann, M. Niggemann, A. Hinsch and A. Gombert, Efficiency limiting factors of organic bulk heterojunction solar cells identified by electrical impedance spectroscopy, Solar Energy Materials and Solar Cells 91 (5), 390-393 (2007).

[129] D. B. A. Rep, A. F. Morpurgo, W. G. Sloof and T. M. Klapwijk, Mobile ionic impurities in organic semiconductors, Journal of Applied Physics 93 (4), 2082-2090 (2003).

[130] J. Bisquert, G. Garcia-Belmonte, A. Munar, M. Sessolo, A. Soriano and H. J. Bolink, Band unpinning and photovoltaic model for P3HT:PCBM organic bulk heterojunctions under illumination, Chemical Physics Letters 465 (1-3), 57-62 (2008).

[131] R. S. Muller, T. I. Kamins and M. Chan, Device Electronics for Integrated Circuits. (Wiley, New York, 2003).

[132] S. M. Sze and K. K. Ng, Physics of Semiconductors. (Wiley, New Jersey, 2007).

[133] E. Lioudakis, A. Othonos, I. Alexandrou and Y. Hayashi, Ultrafast carrier dynamics on conjugated poly(3-hexylthiophene)/[6,6]-phenylC(61)-butyric acid methyl ester composites, Applied Physics Letters 91 (11), - (2007).

[134] P. Kumar, S. C. Jain, V. Kumar, S. Chand and R. P. Tandon, A model for the current-voltage characteristics of organic bulk heterojunction solar cells, Journal of Physics D-Applied Physics 42 (5), - (2009).

[135] B. L. Anderson and R. L. Anderson, Fundamentals of Semiconductor Devices. (Mc Graw Hill, New York, 2005).

[136] G. Garcia-Belmonte, A. Munar, E. M. Barea, J. Bisquert, I. Ugarte and R. Pacios, Charge carrier mobility and lifetime of organic bulk heterojunctions analyzed by impedance spectroscopy, Organic Electronics 9 (5), 847-851 (2008).

[137] G. Jarosz, On doubts about Mott-Schottky plot of organic planar heterojunction in photovoltaic cell, Journal of Non-Crystalline Solids 354 (35-39), 4338-4340 (2008).

[138] D. Wohrle and D. Meissner, Organic Solar-Cells, Advanced Materials 3 (3), 129-138 (1991).

[139] J. Y. Kim, S. H. Kim, H. H. Lee, K. Lee, W. L. Ma, X. Gong and A. J. Heeger, New architecture for high-efficiency polymer photovoltaic cells using solution-based titanium oxide as an optical spacer, Advanced Materials 18 (5), 572-+ (2006).

[140] C. J. Brabec, J. A. Hauch, P. Schilinsky and C. Waldauf, Production aspects of organic photovoltaics and their impact on the commercialization of devices, Mrs Bulletin 30 (1), 50-52 (2005).

[141] A. Haugeneder, M. Neges, C. Kallinger, W. Spirkl, U. Lemmer, J. Feldmann, U. Scherf, E. Harth, A. Gugel and K. Mullen, Exciton diffusion and dissociation in conjugated polymer fullerene blends and heterostructures, Physical Review B 59 (23), 15346-15351 (1999).

[142] M. Morana, M. Wegscheider, A. Bonanni, N. Kopidakis, S. Shaheen, M. Scharber, Z. Zhu, D. Waller, R. Gaudiana and C. Brabec, Bipolar charge transport in PCPDTBT-PCBM bulk-heterojunctions for photovoltaic applications, Advanced Functional Materials 18 (12), 1757-1766 (2008).

[143] B. Kannan, K. Castelino and A. Majumdar, Design of nanostructured heterojunction polymer photovoltaic devices, Nano Letters 3 (12), 1729-1733 (2003).

[144] E. Kymakis, N. Kornilios and E. Koudoumas, Carbon nanotube doping of P3HT: PCBM photovoltaic devices, Journal of Physics D-Applied Physics 41 (16), - (2008).

[145] W. U. Huynh, J. J. Dittmer and A. P. Alivisatos, Hybrid nanorod-polymer solar cells, Science 295 (5564), 2425-2427 (2002).

[146] E. Arici, N. S. Sariciftci and D. Meissner, Hybrid solar cells based on nanoparticles of CuInS2 in organic matrices, Advanced Functional Materials 13 (2), 165-171 (2003).

[147] V. Kolachure and M. H. C. Jin, presented at the Photovoltaic Specialists Conference, 2008. PVSC '08. 33rd IEEE, 2008.

[148] H. Xin, F. S. Kim and S. A. Jenekhe, Highly efficient solar cells based on poly(3-butylthiophene) nanowires, Journal of the American Chemical Society 130 (16), 5424-+ (2008).

[149] S. K. Ghosh and T. Pal, Interparticle coupling effect on the surface plasmon resonance of gold nanoparticles: From theory to applications, Chemical Reviews 107 (11), 4797-4862 (2007).

[150] S.-Y. Wang, D.-A. Borca-Tasciuc and D. A. Kaminski, Spectral coupling of fluorescent solar concentrators to plasmonic solar cells, Journal of Applied Physics 109 (7), 074910 (2011).

[151] J. Muller, B. Rech, J. Springer and M. Vanecek, TCO and light trapping in silicon thin film solar cells, Solar Energy 77 (6), 917-930 (2004).

[152] J. Meier, S. Dubail, S. Golay, U. Kroll, S. Fay, E. Vallat-Sauvain, L. Feitknecht, J. Dubail and A. Shah, Microcrystalline silicon and the impact on micromorph tandem solar cells, Solar Energy Materials and Solar Cells 74 (1-4), 457-467 (2002).

[153] L. D. Rampino and F. F. Nord, Preparation of palladium and platinum synthetic high polymer catalysts and the relationship between particle size and rate of hydrogenation, Journal of the American Chemical Society 63, 2745-2749 (1941).

[154] A. Henglein, B. G. Ershov and M. Malow, Absorption-Spectrum and Some Chemical-Reactions of Colloidal Platinum in Aqueous-Solution, Journal of Physical Chemistry 99 (38), 14129-14136 (1995).

[155] L. A. DuBridge, The thermionic emission from clean platinum, Physical Review 32 (6), 0961-0966 (1928).

[156] M. Suzuki, T. Ono, N. Sakuma and T. Sakai, Low-temperature thermionic emission from nitrogen-doped nanocrystalline diamond films on n-type Si grown by MPCVD, Diamond and Related Materials 18 (10), 1274-1277 (2009).

[157] P. Liu, Q. Sun, F. Zhu, K. Liu, K. Jiang, L. Liu, Q. Li and S. Fan, Measuring the work function of carbon nanotubes with thermionic method, Nano Letters 8 (2), 647-651 (2008).

[158] R. B. Dinwiddie, A. J. Whittaker and D. G. Onn, Thermal-Conductivity, Heat-Capacity, and Thermal-Diffusivity of Selected Commercial Ain Substrates, International Journal of Thermophysics 10 (5), 1075-1084 (1989).

[159] A. Yadav, R. Kumar, G. Bhatia and G. L. Verma, Development of mesophase pitch derived high thermal conductivity graphite foam using a template method, Carbon 49 (11), 3622-3630 (2011).

[160] K. C. Leong and H. Y. Li, Theoretical study of the effective thermal conductivity of graphite foam based on a unit cell model, International Journal of Heat and Mass Transfer 54 (25-26), 5491-5496 (2011).

[161] O. W. Richardson, The emission of electricity from hot bodies, 2d ed. (Longmans, Green and co., London, New York etc., 1921).

[162] A. L. Reimann, Thermionic emission. (Chapman & Hall, Ltd., London,, 1934).

[163] N. Tallaj and M. Buylebodin, WORK FUNCTION MEASUREMENTS ON GERMANIUM BY THERMIONIC EMISSION, Surface Science 69 (2), 428-436 (1977).